学位論文

An Observational Study of Rapid Gamma-ray Variability in the Brightest Blazar Flares

(最も明るいブレーザーの
フレア時における短時間変動の観測的研究)

平成 25 年 12 月博士(理学)
申請

東京大学大学院理学系研究科
物理学専攻
齊藤新也

An Observational Study of Rapid Gamma-ray Variability in the Brightest Blazar Flares (最も明るいブレーザーのフレア時における短時間変動の観測的研究)

Shinya Saito

Ph.D. Thesis

Department of Physics, Graduate School of Science
The University of Tokyo

December, 2013

Abstract

We have systematically studied rapid gamma-ray variability of blazars with *Fermi* in order to investigate the nature of blazar flares. The Large Area Telescope (LAT) onboard the *Fermi* satellite has a capability of observing gamma-rays from 20 MeV to 300 GeV, which correspond to the energy band where Flat Spectrum Radio Quasar (FSRQ) blazars emit most of their radiative energy. *Fermi*-LAT is therefore well suited for studying energy dissipation processes in blazar jets, and in particular acceleration mechanisms leading to generation of ultra-relativistic particles emitting the observed gamma-ray photons. Our goal in this thesis is to locate the emitting region in blazar jets by examining time profiles of gamma-ray flares with unprecedentedly good time resolution. We selected ten bright flares with the best photon statistics from all the LAT-detected FSRQs amounting to $\sim$400 objects for this work. In our systematic analysis of short-timescale variability, we discovered very rapid flux changes with doubling timescale as short as 1 hour, which was the shortest variability time scale in the GeV range found for all the Active Galactic Nuclei (AGN) so far. For investigating high-amplitude variability on sub-hour timescales, where photon statistics were limited, we adopted Bayesian method in modeling the light curves. In this Bayesian analysis we found an indication for marginal sub-hour variability for only one flare among the ten selected events. Our novel findings that FSRQs show hour-scale variability and little indications for sub-hour variability in GeV energy range puts strong constraints on the gamma-ray emitting region which is a long-lasting question in blazar studies. We modeled time profiles of the brightest blazar flares with numerical blazar code assuming internal shock scenario, and succesfully constructed a consistent picture of blazar emission.

Contents

Chapter 1

Introduction

One of the most energetic and spectacular phenomena associated with Active Galactic Nuclei (AGN) is the production of relativistic jets. About 10% of the total AGN population distinctly show high activity in radio band with highly collimated radio jets launched from the vicinities of super massive black holes (SMBHs) located in the centers of AGN. These jets are believed to be driven by the enormous amount of power released when gas and dust accrete onto the deep gravitational potential of SMBHs whose mass exceeds millions of solar mass. The energy of the accreting matter is converted very efficiently into the kinetic energy of relativistic, highly magnetized outflows either in the innermost parts of the accretion disks, or in the ergospheres of rotating SMBHs (Blandford & Znajek 1977).

Relativistic jets can be studied most effectively in blazars, which constitutes a subclass of radio-loud AGN. As the direction of a jet points toward the Earth in the case of blazars, the observed spectrum of a system is dominated by a jet component due to the beaming effect. The spectral energy distribution (SED) of blazars is characterized by two broad-band non-thermal components: synchrotron radiation of relativistic electrons which peaks in optical/UV/X-rays, and inverse Compton radiation which peaks in gamma-rays. Blazars which show strong optical line emission of the circumnuclear matter ('broad- and narrow line regions') are called flat spectrum radio quasars (FSRQs). FSRQs constitute most luminous population of blazars with SMBHs accreting at high rates (over 1% of the Eddington limit), and show high-amplitude multi-wavelength variability on various time scales from decades down to hours. The observed rapid and high-amplitude variability suggests that bulk of the kinetic energy in the jet is dissipated in extremely compact region relative to large jet structure reaching hundreds of kpc scale.

However, the location of the emitting region in FSRQ jets (the 'blazar emission zone'), which is crucial for understanding the energetics of AGN systems as well as the

dynamics of relativistic outflows in general, has been an open question for years, despite the extensive research in the field. Furthermore, there is no consensus on whether a single emitting region contributes to the overall multifrequency spectrum or multiple emitting regions exist. According to some researchers, the combined radio and optical polarization studies of blazar sources suggest the dominant emitting region to be located as far as $\sim$ 10 pc from SMBHs ("far-dissipation zone" scenario; e.g., Marscher et al. 2010), while the other authors, based on the overall SED modeling, advocate for much closer distances from the central engine, $\sim$ 0.01 pc ("near-dissipation zone" scenario; e.g., Ghisellini 2010).

A way of sampling in conventional multifrequency blazar monitoring programs may be one of the main reasons for this controversy. Current multifrequency study using data integrated over days inevitably mask variability shorter than the integrated intervals. In addition, multifrequency observations carried using various telescopes are rarely truly simultaneous, and involve uneven sampling of the source light curve with different binning and exposure gaps caused by various operational issues of individual instruments.

A new approach for blazar variability study, making full use of the available gamma-ray data, is presented in this thesis. Since most of the radiative power of FSRQs is released in GeV gamma-rays, rapid and high-amplitude variability in this energy range is of particular importance for investigating energy dissipation processes and energetics of relativistic jets in this type of sources. We therefore analyse systematically FSRQs with *Fermi*-LAT, which provides currently best quality GeV gamma-ray data since 2008. The accumulation of five-year all-sky survey data by *Fermi*-LAT includes a variety of blazar flares with excellent photon statistics, allowing one to study sub-daily blazar variability for the first time in the GeV energy range. Such studies were not possible in the past with the previous GeV gamma-ray instrument EGRET onboard *Compton Gamma Ray Observatory (CGRO)* launched in 1991, because of a much smaller effective area of the detector.

This thesis is organized as follows. Chapter 2 presents review of properties of AGN and relativistic jets. Chapter 3 presents detailed description of LAT onboard the *Fermi* spacecraft. Chapter 4 presents selection procedure of the blazar flares analysed in this thesis, where we identified ten flaring periods with the highest flux level from all the *Fermi* detected blazars based on the 5-year data. Chapter 5 presents systematic analysis for hour-scale time variability for the selected flaring intervals of blazars. Discussions on source energetics implicated by rapid variability is also included in this chapter. Chapter 6 presents further investigation for sub-hour variability. We introduce *Bayesian block* method to characterize variability for very limited photon statistics. Chapter 7

presents time-dependent modeling of the observed rapid variability and discussions on emitting region of blazars. Chapter 8 presents a summary of this thesis.

Chapter 2

Relativistic Jets Emerging from Super Massive Black Holes

2.1 Active Galactic Nuclei

Active Galactic Nuclei (AGN) are compact regions present at the center of galaxies. They emit enormous amount of radiation ($10^{40} - 10^{46}$ erg s^{-1}) which often exceeds total energy emitted from other components of host galaxies, such as stars, gas, and dust. Electromagnetic radiation from AGN spans over entire observable wavelength from radio to sometimes very high energy gamma-ray. It is also known that the emission from AGN is highly variable on a timescale less than days (see § 2.3.2 for details). Such a powerful emission of AGN from compact region is believed to be produced by mass accretion onto super massive black holes (SMBHs) which have millions times solar mass, because accretion is a very efficient energy release process that could extract $\sim 10\%$ of the rest energy of the infalling mass (e.g., Peterson 1997).

2.1.1 Classification

In general, AGN are divided into two classes based on their ratio of radio intensities to optical intensities (Ormes et al. 1996). It is known that about 90% of AGN show low radio activity and hence are classified as "radio quiet". The radio quiet AGN include Seyfert galaxies and radio quiet quasars. On the other hand, $\sim 10\%$ of AGN with high radio activity are classified as "radio loud" AGN, which accompany jet structures extending in opposite directions from the central SMBHs.

A schematic picture of the current paradigm for radio-loud AGN is shown in Figure 2.1 (Urry & Padovani 1995). It is believed that the structure surrounding the AGN

is axisymmetric. The central SMBH, accretion disk, and Broad Line Region (BLR) are surrounded by obscuring dusty torus. Because of the high velocity of clouds, optical emission lines from the broad line region show broad structure. Narrow line region, which emits narrow optical lines, is believed to be located outside the BLR. This unification scenario leads to the idea that the observational characteristics of any individual AGN depend only on its orientation relative to the Earth. At lines of sight near the equator of the SMBH, the radio jets are approximately in the plane of the sky and indeed Cygnus A is a good example of an AGN with such an orientation, as shown in Figure 2.2 (Perley et al. 1984). When both the broad and narrow lines are visible, such sources are classified as broad line radio galaxies. In case that the BLR is obscured by the torus and only Narrow Line Region (NLR) is visible, the object is classified as narrow line radio galaxies.

At the opposite extreme are AGN for which the line of sight is very close to the jet axis. High spatial resolution radio observation revealed that these sources are dominated at arc-second scale by compact and flat-spectrum synchrotron emission from the central region. At milli arcsecond scale, superluminal jet motion is observed for many sources, with apparent speeds of up to $> 50c$. Unique to AGN with this orientation is the presence of gamma-ray emission arising from inverse Compton scattering by high-energy electrons in the jet. These AGN are known as blazars.

2.1.2 Blazars

Blazars are classified into two major classes, Flat Spectrum Radio Quasars (FSRQs) and BL Lac objects. This classification is based only on the equivalent width (EW) of optical emission lines. Optical spectra of FSRQs exhibit strong optical emission lines, while those of BL Lacs show very weak or no emission lines. It is believed that this difference is due to the luminosity of the accretion disk around these objects. Namely, the luminous standard accretion disk (Shakura & Sunyaev, 1973) of FSRQs ionizes the BLR and strong optical lines are present, while BL Lac objects have less luminous disk and so the emission line is not present or very weak (e.g., Ghisellini et al. 2011).

Electromagnetic radiation of blazars extends over entire wavelength from radio to gamma-ray band. The broadband spectrum is characterized by two broad non-thermal bumps. The lower-energy bump peaks at optical to X-ray band and this component is thought to be due to synchrotron emission by ultra-relativistic electrons accelerated within the jet. Strong polarization in radio and optical bands support the synchrotron origin. On the other hand, the higher-energy bump peaks at gamma-ray band and this

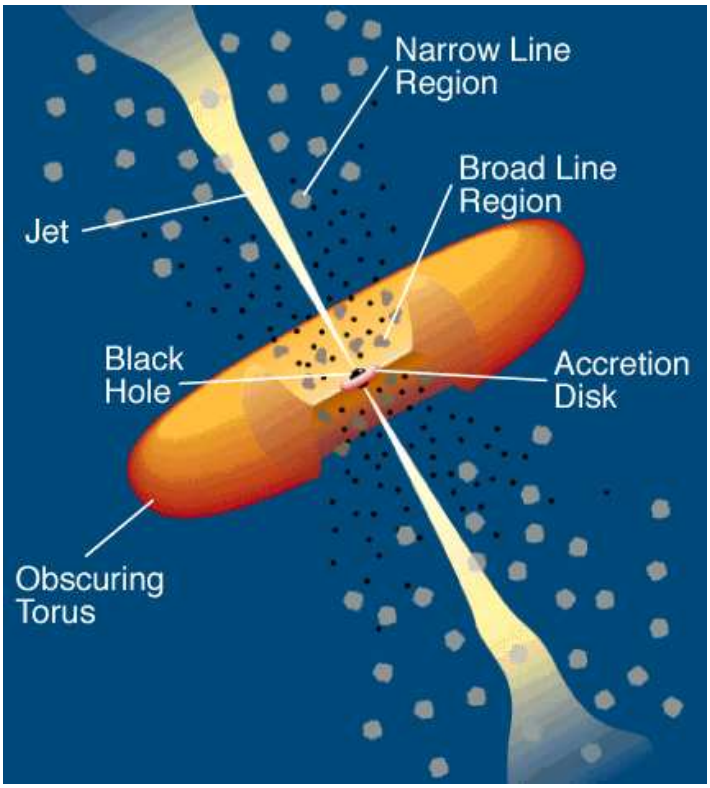

Figure 2.1: Schematic view of radio-loud AGN, which is taken from Urry & Padovani (1995).

is considered to be inverse Compton emission by the same population of electrons. It is thought that the seed photons for inverse Compton process are synchrotron ones for BL Lac objects, while photons from external radiation field such as BLR and dusty torus are believed to be the seed one for the case of FSRQs (e.g. Sikora et al. 1994).

It is known that more powerful FSRQ show (1) lower peak frequencies of the synchrotron and inverse Compton spectra and (2) increase of the ratio of the inverse Compton component relative to the synchrotron one, as compared to dim BL Lac objects (Kubo et al. 1998, Fossati et al. 1998, Donato et al. 2001). A common interpretation of this "blazar sequence" is that Compton cooling of electrons is more efficient for luminous objects due to high photon density of external radiation field such as BLR. BL Lacs are therefore believed to accelerate electrons to higher energy than FSRQs.

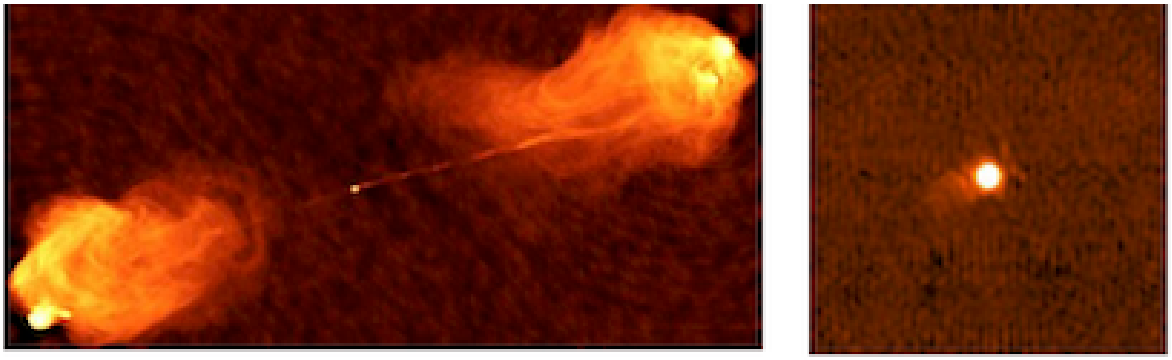

Figure 2.2: (*left*) VLA 5 GHz image of Cygnus A, which is taken from Perley et al. (1984). The east-west extent of the radio emission is 127″. (*right*) VLA 1.4 GHz image of Mrk 421, which is taken from Becker et al.(1995).

2.2 Radiative Processes

Since broadband spectrum of blazars from radio to TeV band is characterized by two broad bumps, the lower and higher of which are thought to be synchrotron and inverse Compton emissions, here we briefly provide the basic formulae of the relevant processes, together with the $\gamma\gamma$ annihilation process which is essential above sub-TeV high energy gamma-rays (e.g., Rybicki & Lightman 1979, Longair 2011).

2.2.1 Synchrotron Radiation

The synchrotron power per unit frequency emitted by relativistic single electron with Lorentz factor γ is given as,

$$P(\omega) = \frac{\sqrt{3}}{2\pi}\frac{e^3 B \sin\alpha}{m_e c^2} F\left(\frac{\omega}{\omega_c}\right), \tag{2.1}$$

where α is the angle between electron velocity and magnetic field direction ($\boldsymbol{B}$), and ω_c is critical frequency given by the following equation,

$$\omega_c = \frac{3\gamma^2 e B \sin\alpha}{2 m_e c}. \tag{2.2}$$

$F(x)$ is defined as

$$F\left(x\right) \equiv x \int_x^\infty K_{\frac{5}{3}}(\xi)\mathrm{d}\xi, \tag{2.3}$$

where $K_{5/3}\left(x\right)$ is the modified Bessel function of 5/3 order. Integration of $P(\omega)$ over ω and averaging over the angle gives the total emitted power by synchrotron emission of

$$P = \frac{4}{3}\sigma_T c \beta^2 \gamma^2 U_{\mathrm{B}}, \tag{2.4}$$

where σ_{T} is Thomson cross section and $U_{\mathrm{B}} = B^2/8\pi$ is the magnetic field energy density.

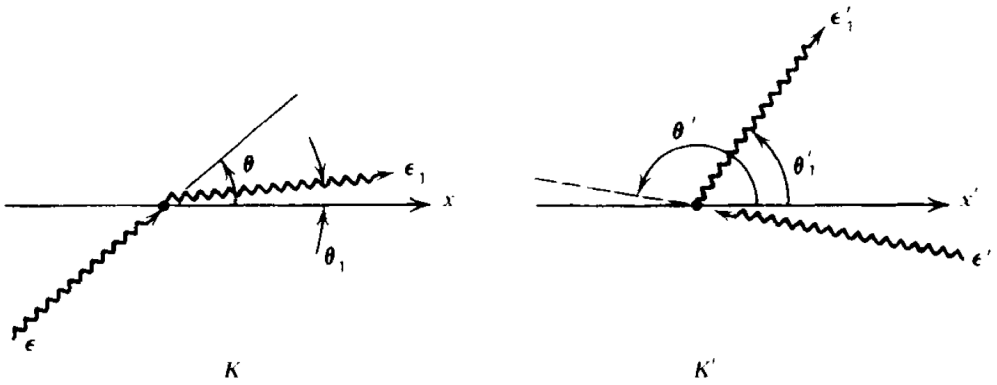

Figure 2.3: Scattering geometries in the observer's (Left) and electron rest (Right) frames, that are taken from Rybicki & Lightman 1979.

2.2.2 Inverse Compton Scattering

We first consider a scattering process by a single relativistic electron for a single photon in Thomson regime. The scattering geometry is shown in Figure 2.3. The electron energy, photon energy, and scattered photon energy are represented by $\gamma \equiv (1-\beta^2)^{-1/2}$, ϵ_0, and ϵ. We also show parameters in electron rest frame with prime, while those in laboratory frame without prime. Lorentz transformation and Compton kinematics give the following equations.

$$\epsilon_0' = \epsilon_0 \gamma \left(1 - \beta \cos\theta\right), \tag{2.5}$$

$$\epsilon = \epsilon' \gamma \left(1 + \beta \cos\theta'\right). \tag{2.6}$$

Since the scattering in the electron rest frame is elastic (Thomson regime), we can safely assume $\epsilon_0' = \epsilon'$. Hence, the ratio of photon energy before scattering, in the electron rest frame, and after scattering is expressed as

$$\epsilon_0 : \epsilon_0' : \epsilon \simeq 1 : \gamma : \gamma^2. \tag{2.7}$$

This means that a low-energy photon ϵ_0 is upscattered by relativistic electrons $\gamma m_e c^2$ and gains energy up to $\gamma^2 \epsilon_0$.

We then consider the case that isotropic distribution of relativistic electrons upscatter the isotropic distribution of photons. The total power emitted in the observer rest frame could be written as,

$$\frac{dE}{dt} = c\sigma_T \gamma^2 \int \left(1 - \beta\cos\theta\right)^2 \epsilon v d\epsilon = c\sigma_T \gamma^2 \left(1 + \frac{1}{3}\beta^2\right) U_{\rm ph} \tag{2.8}$$

where $v = v(\epsilon)$ is photon number density, σ_T is Thomson cross section. Since photon field is isotropic,

$$\left\langle (1 - \beta \cos\theta)^2 \right\rangle = 1 + \frac{1}{3}\beta^2. \tag{2.9}$$

Also, $U_{\rm ph}$ is the initial photon energy density and expressed as,

$$U_{\rm ph} \equiv m_e c^2 \int \epsilon v(\epsilon) d\epsilon. \tag{2.10}$$

Finally energy loss rate of electrons via inverse Compton process is

$$P_{\rm IC} = \frac{4}{3}\sigma_T c \beta^2 \gamma^2 U_{\rm ph}. \tag{2.11}$$

Thus, we obtain a well-known relation from equations (2.4) and (2.11),

$$\frac{P_{\rm sync}}{P_{\rm IC}} = \frac{U_{\rm B}}{U_{\rm ph}} \tag{2.12}$$

We note that Thomson regime is valid only in the case that photon energy is much smaller than the electron rest mass in the electron rest frame ($\gamma\epsilon_0 \ll m_e c^2$). If the incoming photon energy approaches the electron rest mass energy $\gamma\epsilon_0 \sim m_e c^2$, the quantum relativistic cross-section has to be introduced. The relevant total cross-section in the Klein-Nishina regime is given by the Klein-Nishina formula,

$$\sigma_{\rm KN} = \pi r_e^2 \frac{1}{x}\left\{\left[1 - \frac{2\,(x+1)}{x^2}\right]\ln 2x + 1 + \frac{1}{2} + \frac{4}{x} - \frac{1}{2\,(2x+1)^2}\right\}, \tag{2.13}$$

where $x = \epsilon_0/m_e c^2$ and r_e is the classical electron radius. In the deep Klein-Nishina case of $x \gg 1$, the Klein-Nishina cross-section is expressed as

$$\sigma_{\rm KN} = \pi r_e^2 \frac{1}{x}\left(\ln 2x + \frac{1}{2}\right). \tag{2.14}$$

The cross-section roughly decreases as x^{-1} at higher energies and consequently this results in significant decrease of luminosity in Klein-Nishina regime.

2.2.3 $\gamma\gamma$ Absorption

When two photons have sufficiently high energy, they can annihilate and generate an electron-positron pair. For this process to take place, the total energy of the two photons has to be above at least the rest mass energy of the electron and positron. Let us first consider that a high energy photon of energy E_1 collides with a target photon of energy E_2 and derive the minimum threshold energy E_2 required for $\gamma\gamma$ annihilation to occur.

The four-momenta of the two photons before collision are,

$$\boldsymbol{P}_1 = \left[\epsilon_1/c, (\epsilon_1/c)\,\boldsymbol{i}_1\right], \quad \boldsymbol{P}_2 = \left[\epsilon_2/c, (\epsilon_2/c)\,\boldsymbol{i}_2\right], \tag{2.15}$$

Energy and momentum conservation requires,

$$\boldsymbol{P}_1 + \boldsymbol{P}_2 = \boldsymbol{P}_3 + \boldsymbol{P}_4, \tag{2.16}$$

where $\boldsymbol{P}_3$ and $\boldsymbol{P}_4$ are the four-momenta of electron and positron. To calculate the threshold energy, the produced electron and positron need to be just at rest, and hence

$$\boldsymbol{P}_3 = [m_e c, 0]\,, \quad \boldsymbol{P}_4 = [m_e c, 0]\,. \tag{2.17}$$

By squaring both sides of Eq.(2.16) and using the following equations,

$$\boldsymbol{P}_1 \cdot \boldsymbol{P}_1 = \boldsymbol{P}_2 \cdot \boldsymbol{P}_2 = 0, \tag{2.18}$$

$$\boldsymbol{P}_3 \cdot \boldsymbol{P}_3 = \boldsymbol{P}_4 \cdot \boldsymbol{P}_4 = \boldsymbol{P}_3 \cdot \boldsymbol{P}_4 = m_e^2 c^2, \tag{2.19}$$

the threshold condition can be derived as follows,

$$E_2 \geq E_{\rm th} = \frac{2 m_e^2 c^4}{E_1 \left(1 - \cos\theta\right)}, \tag{2.20}$$

where θ is the angle between the directions of the two photons. For example, considering the head-on collision ($\theta = \pi$), $\gamma\gamma$ annihilation occurs when

$$E_2 \geq \frac{m_e^2 c^4}{E_1} = \frac{0.26 \times 10^{12}}{E_1}\ \text{eV}. \tag{2.21}$$

Considering the BLR photon whose energy is typically $\sim 10\,\text{eV}$, the gamma-ray above $30\,\text{GeV}$ begin to be absorbed by BLR photon field.

2.3 Observations of Blazars

2.3.1 Spectral Characteristics

Spectral Energy Distribution (SED) for several blazars including BL Lacs and FSRQs are shown in Figure 2.4. Kubo et al. (1998) first claimed that despite the differences in the continuum shapes of different sub-classes of blazars, a unified scheme is possible, whereby blazar continua can be described by a family of analytic curves with the source luminosity as the fundamental parameter. The main suggested trend is that with increasing luminosity both the synchrotron peak and the inverse Compton peak move to lower frequencies and that the latter becomes energetically more dominant (e.g., Kubo et al. 1998, Fossati et al. 1998). The proposed scenario, in which the intrinsic jet power regulates, in a continuous sequence, the observational properties from the weaker High-frequency peaked BL Lac (HBL), through Low-frequency-peaked BL Lac (LBL),

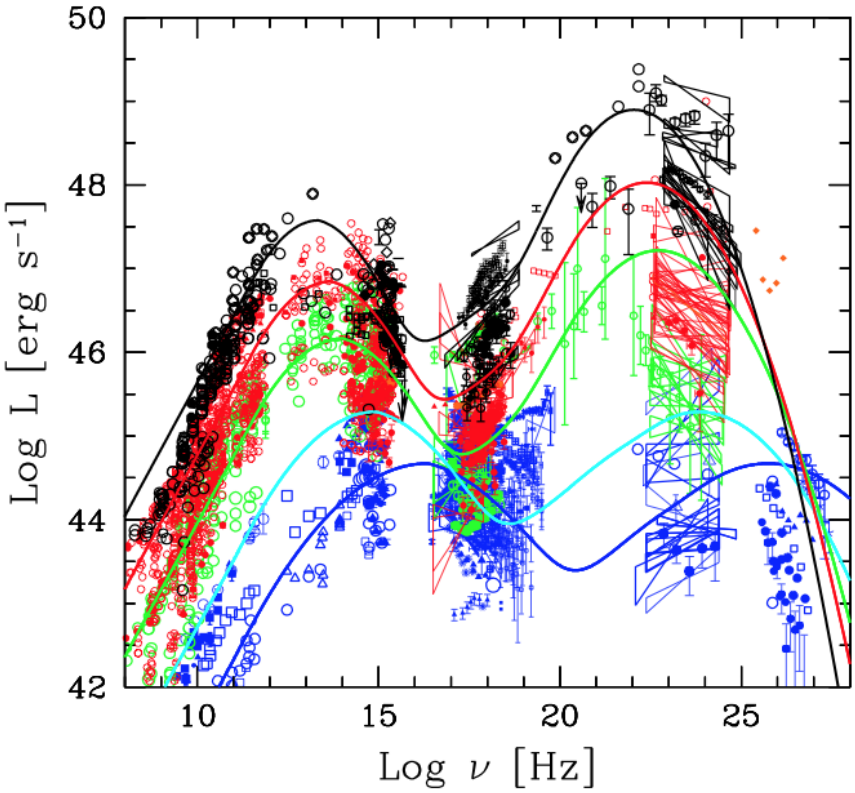

Figure 2.4: Broadband Spectral Energy Distribution (SED) for blazars (Ghisellini 2013). Solid lines represent the phenomenological models presented in Fossati et al. (1998).

to the most powerful FSRQs, also fits in very nicely with the unification of FR I and FR II type radio galaxies as proposed by Bicknell (1995). The whole radio-loud AGN population could be unified in a two parameter space one being the intrinsic jet power, and the other the viewing angle.

2.3.2 Temporal Studies

One of the main features of blazars is their rapid time variability, and intense flares have been detected in various wavelengths. Most strikingly, the shortest variability of the order of several minutes has been detected mainly in TeV band by ground-based Imaging Atmospheric Cherenkov Telescopes (IACTs). *HESS* detected rapid variability from High-frequency peaked BL Lac (HBL) PKS 2155−304 and the variability timescale was $\sim$ 200 s (Aharonian et al. 2007). Similar rapid variability of the timescale of minutes was also detected by MAGIC in sub-TeV range from FSRQ 4C 21.35 (Aleksic et al. 2011). Since sub-TeV photons of $E \gtrsim 100$ GeV cannot escape from the region within BLR due to $\gamma\gamma$ annihilation, detection of sub-TeV photons from FSRQ implies that the

emission region is outside BLR, possibly pc-scale from central SMBH (e.g., Aleksic et al. 2011, Tanaka et al. 2011). Very recently, VERITAS also detected similar TeV flare from BL Lac and the decay time was obtained as 13 ± 4 min (Arlen et al. 2013).

Temporal analysis has been a powerful tool to understand working processes and derive physical quantities in blazar dissipation region (e.g., Takahashi et al. 1996, Takahashi et al. 2000, Kataoka et al. 2001). For example, from *ASCA* X-ray data, Takahashi et al. (1996) reported a time lag of about 4000 s between soft (0.5–1.0 keV) and hard X-ray bands(2–7.5 keV) (soft X-ray variation lags behind the hard X-ray one) from a famous BL Lac object Mrk 421. The authors also found that the X-ray spectrum correspondingly evolved in a clockwise way within the flux and index plane. This clockwise variation is naturally interpreted in terms of energy-dependent synchrotron cooling and magnetic field strength at the emission region was derived only from the observed time lag as $B \sim 0.2$ G for $\delta = 5$).

X-ray variability timescale was first derived as ~ 0.5 days based on structure function analysis for *ASCA* continuous X-ray light curve of 7 days for Mrk 421 (Takahashi et al. 2000). Figure 2.5 shows the calculated structure function in which a sharp turnover was clearly seen at ~ 0.5 day. The variability timescale allows us to roughly estimate the location of the emission region. Under the assumption of a conical jet geometry of opening angle $\theta \sim 1/\Gamma$, where Γ is the Lorentz factor of the jet and $\Gamma \sim 10$ is supposed, the location of the emission region (distance from the central SMBH, D) is evaluated as $R \sim D/\Gamma$. Here, R is the size of the emission region and is grossly evaluated to be $R \sim ct_{\rm var}\delta \sim 10^{16}\,(\delta/10)$ cm, where δ is the beaming factor and $\delta \sim 10$ is assumed. Symmetric flare shapes were also observed from the same *ASCA* data, implying that the dominant timescale is the light crossing time through the emission region (Takahashi et al. 2000).

2.3.3 One Zone Emission Model

In 1980s, the observed emissions from blazars were considered to be produced everywhere in the jet, depending on magnetic field and number density of emitting particles (Marscher (1980), Konigl (1981)). In this picture, higher energy photons were considered to be produced at close position to the SMBH, and the variability timescales were different for different energy photons.

In 1990s, however, this picture of emission was abandoned because of the development of new gamma-ray observatories such as *Compton Gamma Ray Observatory (CGRO)*. EGRET onboard *CGRO* discovered that blazars are strong gamma-ray emitters, and the

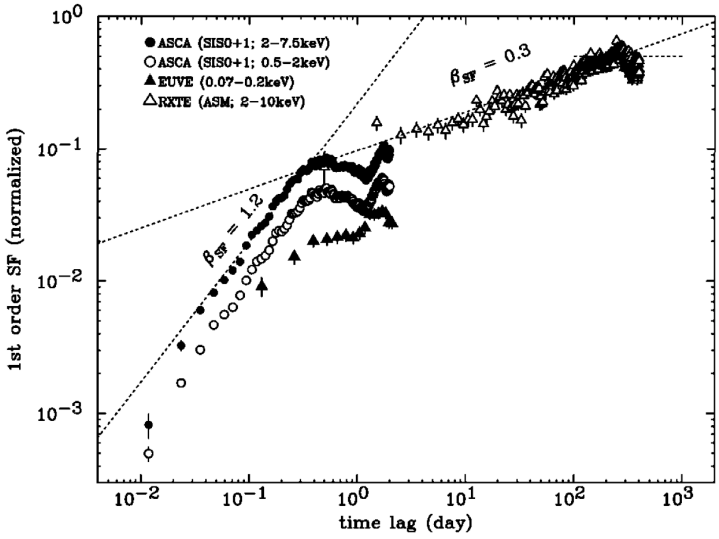

Figure 2.5: Structure function of Mrk 421 calculated from *ASCA*, *RXTE* and *EUVE* data (Takahashi et al. 2000).

gamma-ray time profile often changes simultaneously with X-ray and optical emission (Hartman et al. (1999)). This Observational evidence caused a paradigm shift from the multi emitting zone paradigm to the one zone model, which had been a successful model for describing variability of broadband emission with fewer parameters.

Finally, recent observation revealed that the situation is not simple that we could understand whole emission from blazars based on the one zone model. Radio VLBI maps show that the jet is actually composed of several distinct knots, which possibly contribute to observed flux from the jet (Kellermann et al. (2004)). Furthermore, as a result of progress in observation technique, very often the broadband SED could not be explained by the one zone model (Nalewajko et al. (2012)).

2.4 Beaming Effects in Relativistic Jets

Since the jets accompanied with blazars have ultra relativistic speed ($\Gamma \gg 1$ where Γ is the bulk Lorentz factor of jets), relativistic effects affect observed properties of blazars. We briefly review such effects in this section. When a blob is moving relativistically and radiating isotropically in the rest frame K', the emission is strongly beamed or anisotropic in the observer's frame K. As a result, the following three effects emerge.

2.4.1 Aberration of Light

According to the well-known Lorentz transformation formula, light traveling direction can be related as

$$\tan\theta = \frac{\sin\theta'}{\Gamma\left(\cos\theta' + v/c\right)}, \tag{2.22}$$

$$\cos\theta = \frac{\cos\theta' + v/c}{1 + (v/c)\cos\theta'}. \tag{2.23}$$

Here Γ is the blob's Lorentz factor and defined as $\Gamma = (1-\beta^2)^{-1/2}$. In the case of $\theta' = \pi/2$, the above two equations provide the direction of the light in the observer's K frame as

$$\tan\theta = \frac{c}{\Gamma v}, \tag{2.24}$$

$$\sin\theta = \frac{1}{\Gamma}. \tag{2.25}$$

This suggests that half of the photons emitted isotropically in the forward direction in the K' frame are concentrated in a narrow cone of $\theta \sim 1/\Gamma$.

2.4.2 Time Dilation

It should be noted that emission time interval $\Delta t_{\rm e}$ is different from arrival time interval $\Delta t_{\rm a}$ for a moving source. By taking into account the difference in the traveling distance of light, relation between the two quantity is derived as,

$$\Delta t_{\rm a} = \Delta t_{\rm e}\left(1 - \beta\cos\theta\right). \tag{2.26}$$

On the other hand, Lorentz transformation gives the following relation,

$$\Delta t_{\rm e} = \Gamma \Delta t'_{\rm e}. \tag{2.27}$$

Finally, we obtain

$$\Delta t_{\rm a} = \Gamma\left(1 - \beta\cos\theta\right)\Delta t'_{\rm e} = \Delta t'_{\rm e}/\delta. \tag{2.28}$$

Here $\delta = \left[\Gamma\left(1-\beta\cos\theta\right)\right]^{-1}$ is beaming factor. As is known, if the viewing angle θ is small, the beaming factor exceeds unity.

2.4.3 Frequency and Luminosity Enhancements

Since frequency is the inverse of the time, relation of frequency is derived as

$$\nu = \delta\nu'. \tag{2.29}$$

It is known that a quantity of $I(\nu)/\nu^3$, which is specific intensity $I(\nu)$ divided by the cube of the frequency ν^3, is Lorentz invariant. Hence, we obtain

$$I(\nu) = \delta^3 I'(\nu') = \delta^3 I'(\nu/\delta). \tag{2.30}$$

The integration over the frequency provides

$$I = \int I(\nu)\, d\nu = \delta^4 \int I'(\nu')\, d\nu' = \delta^4 I' \tag{2.31}$$

Hence, by assuming isotropic emission, we obtain the relation between emitted and observed luminosities as

$$L_{\rm obs} = \delta^4 L'_{\rm src}. \tag{2.32}$$

Thus, if the viewing angle is small ($\delta \sim 10$), the observed luminosity is enhanced by factor of 10^4 compared to the total emitted luminosity.

2.5 Internal Shock Model

An internal shock model is the most successful among various models for describing multi-band and time-dependent emission from blazar jets (e.g., Rees 1978, Sikora et al. 1994), and hence we briefly describe the details. The key idea is that the central engine intermittently injects the energy into the jet, implying the ejection of individual shells that have different bulk Lorentz factors and energies. A faster shell catches up and collides with a slower one and shock is formed within the colliding region. The internal shock is considered to accelerate particles up to ultra-relativistic energies by first-order Fermi or other unknown processes.

As is shown schematically in Figure 2.6, let us assume first that two shells of bulk Lorentz factor Γ_1 and Γ_2 and mass of M_1 and M_2 are ejected from the central SMBH with a time interval of t_0. When $\Gamma_2 > \Gamma_1$, the faster shell catches up with the slower one. Using the conservation of energy and momentum, the Lorentz factor of the merged shell could be calculated as follows (Kobayashi et al. (1997), Sari & Piran (1995)).

$$\Gamma \simeq \sqrt{\frac{M_1\Gamma_1 + M_2\Gamma_2}{M_1/\Gamma_1 + M_2/\Gamma_2}} \tag{2.33}$$

The internal energy of the merged shell could be defined as the difference of kinetic energy before the collision and after the collision,

$$E_{\rm int} = M_1 c^2(\Gamma_1 - \Gamma) + M_2 c^2(\Gamma_2 - \Gamma) \tag{2.34}$$

The efficiency of the conversion of the kinetic energy into the internal energy is expressed as,

$$\eta = 1 - \frac{(M_1 + M_2)\Gamma}{M_1\Gamma_1 + M_2\Gamma_2} \tag{2.35}$$

This efficiency is maximized when $M_1 = M_2$, which is the condition we are thinking of in the following arguments.

Velocity of the emerged shock which propagates along the merged shell could be calculated as follows. The considering situation is shown in Figure 2.7. We note that values measured in the upstream region rest frame (moving with the Lorentz factor of Γ_1 relative to the observer rest frame) are expressed by double-prime and those measured in the emitting region rest frame (moving with the Lorentz factor of Γ relative to the observer rest frame) are expressed by single-prime. The Lorentz factor of the generated shock and velocity of emitting region in the upstream region rest frame could be calculated as follows (Stawarz et al. (2004), Komissarov & Falle (1997)).

$$\Gamma''_{\rm sh} = \sqrt{\frac{(\Gamma'' + 1)(4\Gamma'' - 1)^2}{8\Gamma'' + 10}} \tag{2.36}$$

$$\beta'' = \frac{\beta - \beta_1}{1 - \beta\beta_1} \tag{2.37}$$

$$\beta'_{\rm sh} = \frac{\beta''_{\rm sh} - \beta''}{1 - \beta''_{\rm sh}\beta''} \tag{2.38}$$

If $\Gamma_2 \gg 1$ and $\Gamma_2/\Gamma_1 \gg 1$, the velocity of the emerged shock in the emitting region rest frame is known to take marginally constant value; $\beta'_{\rm sh} \simeq 0.1$ (Stawarz et al. (2004)).

Since particle acceleration takes place while the shock is going through the merged shell, the observed (rising) timescale of flares should be directly coupled with the time interval the shock runs in the merged shell. If we assume τ' as the time since collision in the emitting region rest frame, the extent of the shocked region in along the jet in the emitting region rest frame could be expressed as,

$$l'_{\rm sh} = c\beta'_{\rm sh}\tau' \tag{2.39}$$

Finally we obtain the corresponding shock length in the observer rest frame as,

$$l_{\rm sh} \simeq c\beta'_{\rm sh}\delta\Gamma\tau_{\rm obs} \tag{2.40}$$

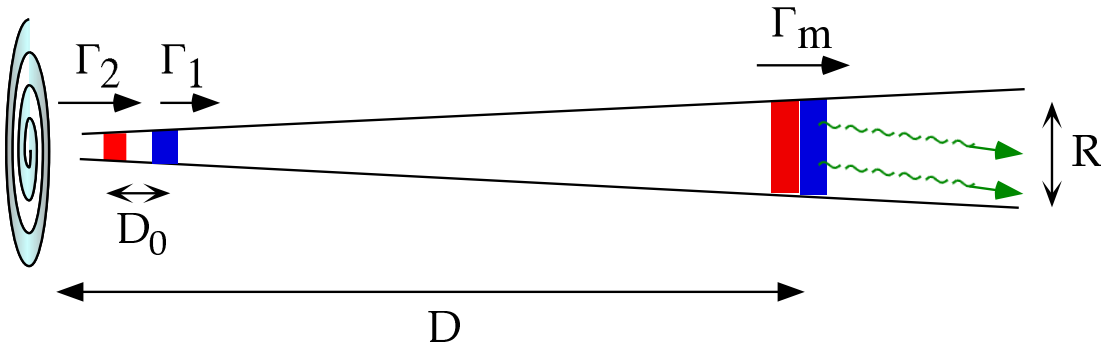

Figure 2.6: A figure illustrating the internal shock scenario, which is taken from Tanihata 2001 (Ph.D. thesis). Relativistic shells are ejected intermittently from the central black hole, and when a faster shell catches up to a slower shell, a shock is formed, where particle acceleration takes place.

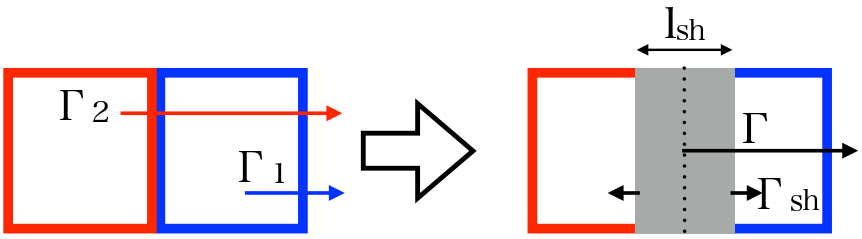

Figure 2.7: A figure illustrating the internal shock propagating along the merged shell. Γ and $\Gamma_{\rm sh}$ represent Lorentz factor of the merged shell and the forward shock. $l_{\rm sh}$ is the length of the shocked region measured in the observer rest frame.

Chapter 3

Fermi Gamma-ray Space Telescope

3.1 Overview

The *Fermi Gamma-ray Space Telescope* has been continuously observing the entire sky in the high-energy gamma-ray domain with an unprecedented sensitivity and an improved angular resolution. The Large Area Telescope (LAT) onboard the *Fermi*, which is the main instrument covering an energy range from 20 MeV to 300 GeV, has a large effective area, a large field of view (FOV), a good time resolution, and dead time short enough to investigate transient phenomena (See Table 3.1 for the detailed values). The LAT adopts active background rejection and discrimination against the large flux of charged particles such as cosmic rays and Earth-albedo gamma-rays. The Fermi Gamma-ray Burst Monitor (GBM) onboard *Fermi* performs spectral and temporal measurements in an energy range from 10 keV to 40 MeV. The GBM mainly detects and localizes transient phenomena such as gamma-ray bursts (GRBs) and solar flares, and alerts the observatory control unit of a GRB trigger for a more refined search with the LAT instrument. *Fermi* can autonomously repoint to the direction of strong GRBs in order to observe so-called afterglow emission during and after the prompt phase, and can provide rapid notification to the science community. Details of the instruments is described in the following sections.

3.1.1 Mission Timeline

Fermi was launched in June 11th, 2008, from Cape Canaveral by a Delta rocket (also known as a Delta II Heavy) into an initial orbit of $\sim$ 565 km altitude at a 25.6 degree inclination with an eccentricity of 0.01. The period of one orbit is 96.5 minutes, and has a 53.4-day precession period (so the sky coordinates, RA and Dec., of the orbit poles

trace a 25.6 degree circle on the sky every 53.4 days). The mission design lifetime is currently planned to be 10 years as a goal.

After the launch, the mission first entered 2-month initial in-orbit checkout (Phase 0). Then, it started one-year science verification during which a all-sky survey was performed (Phase 1). It is currently in normal science operation phase determined by the scientific goals and requirements of guest investigations (Phase 2). Annual guest investigation cycles has continued during Phase 2. The LAT and GBM data become publicly available immediately after the data are processed.

3.1.2 Observing Modes

The LAT and GBM have very large FOVs, and the observatory is capable of pointing flexibly to most directions. One observational constraint is to avoid pointing at or near the Earth to detect astrophysical photons as much as possible. The Earth's limb is indeed a very strong source of albedo gamma-rays, which the LAT sometimes observes for instrument calibration. The South Atlantic Anomaly (SAA) is known as a high particle-background region over the South Atlantic where charged particles trapped by the Earth's magnetic field have high density. While the observatory is passing through the SAA, no science data are taken because the instruments lower the high voltage of their photomultiplier tubes (PMTs). The SAA passage costs $\sim$15% of the total potential observation time of the LAT and GBM.

The *Fermi* spacecraft operates mainly in two observing modes: the survey and pointing modes. Transition between the two modes can be commanded from the ground or by the spacecraft itself. The observatory has been operated in the all-sky survey mode during most of the mission life ($>$ 80% of the observing time). In this mode, the LAT telescope is pointed toward the zenith (the opposite direction to the Earth), and therefore the pointing position gradually and constantly changes relative to the sky. The uniformity of the telescope exposure is realized by rocking the pointing position perpendicular to the orbital motion.

During the first year operation, the instrument axis was rocked 35 degrees north for one orbit, then 35 degrees south for the next orbit, resulting in a two-orbit periodicity. This rocking profile was changed in September 2nd 2009 to a 50 degree rocking angle as a result of optimizing the uniformity of sky coverage. The maximum rocking angle (in case of e.g., sun maneuver) is set to 60 degrees. This observation mode gives uniform sky coverage when averaged over 2 orbits ($\sim$ 3 hours) with the $\sim$30 minutes of on axis exposure for every portion of the sky. Figure 3.3 shows the sensitivities for exposures on

Table 3.1: Summary of LAT instrument parameters and estimated performance (Atwood et al. (2009)).

Parameter	Value
Energy range	20 MeV to 300 GeV
Effective area at normal incidence	9,500 cm^2
Energy resolution (equivalent Gaussian 1σ)	
100 MeV – 1 GeV	9%–15%
1 GeV – 10 GeV	8%–9%
10 GeV – 300 GeV	8.5%–18%
Single photon angular resolution	
on-axis, 68% containment radius:	
>10 GeV	$< 0.15^\circ$
1 GeV	0.6°
100 MeV	3.5°
on-axis, 95% containment radius	$< 3 \times \theta_{68\%}$
Field of View	2.4 str
Timing accuracy	$<10\mu$s
Event readout time	26.5μs

various timescales.

Based on the localization information derived onboard using GBM data, an autonomous repoint request can be sent to the spacecraft in order to change the observation mode to monitor the location of a GRB or another short-timescale transient. This mode keeps the Earth outside of the FOV, and the default Earth Avoidance Angle, which is defined as the minimum angle between the LAT axis and the Earth's limb, is set to 30 degrees. When the target is unocculted but within the Earth Avoidance Angle of the Earth's limb, the spacecraft keeps the target in the FOV with the Earth out of the FOV. After a pre-determined time, which is set to three hours for such autonomous repoint, the telescope will return to the usual survey mode. The pointing accuracy is < 2 degrees (1σ goal of < 0.5 degrees), with a pointing knowledge of < 10 arcsec (goal < 5 arcsec).

3.2 Large Area Telescope

The principal objective of the LAT is highly sensitive gamma-ray observations of celestial sources in the energy range from 20 MeV to 300 GeV. Table 3.1 shows the main characteristics of the LAT instrument. The effective area of the LAT is six times larger, and the field of view is five times larger than the predecessor EGRET onboard *Compton Gamma Ray Observatory (CGRO)*, which was launched in 1991 (Thompson et al. (1993)).

3.2.1 Detection Methodology

The LAT is a pair-conversion type gamma-ray detector. Figure 3.1 and 3.2 show schematic views of the pair conversion process taking place within the LAT instrument. Gamma-rays which penetrate into the detector interact with a high-Z converter material, tungsten, to generate an electron-positron pair. Since the gamma-ray energy is much higher than the rest mass of the electron and positron, the produced pair proceed within the detector in almost the same direction as the incident gamma-ray has. The trajectories of the electron and positron are tracked by silicon strip detectors. At the bottom of the detector there is a calorimeter array made of CsI(Tl) where electromagnetic showers develop and which records the total energy deposited and therefore allows good estimation of the energy of the incident gamma-ray.

Charged particles (e.g. cosmic rays) incident on the LAT also interact with the detectors, resulting in multiple charged-particle tracks. To veto these charged particles, which are "background" for an astrophysical telescope, the LAT is surrounded by an anti-coincidence detector (ACD), which consists of plastic scintillation tiles. Very high energy gamma-rays (E >> 1 GeV) produce thousands of electrons, positrons and gamma-rays some of which escape from the LAT through the ACD ("backsplash"). The EGRET detector onboard *CGRO*, which operated in 1990's, had a monolithic ACD that vetoed an event whenever such $e^-/e^+/\gamma$ hit the ACD. The LAT ACD is on the other hand segmented, and only when such a backsplash hits an ACD tile on the path of the incoming gamma-ray, the event is vetoed. This segmentation also results in a more uniform anti-coincidence threshold over the whole ACD. The segmentation design of the LAT ACD dramatically increases the LAT's effective area for high-energy gamma-rays relative to the EGRET, whose sensitivity decreased above a few GeV.

The output data from the LAT contain the signal pulse heights generated in different parts of the trackers and calorimeters. By combining the pulse heights with the x-y instrumental coordinates on each silicon strip layer, one can reconstruct the particle trajectory. The total energy loss is obtained by summing up the energy deposition over the whole calorimeters. This complete analysis allows us to distinguish between events resulting from photons and background, determine the incident direction, and estimate the energy.

3.2.2 Detector Structure

The LAT consists of an array of 16 tracker (TKR) modules, 16 calorimeter (CAL) modules, and surrounding segmented ACD tiles. The TKR and CAL modules are mounted

at the center of the LAT structure. The three components of the LAT instrument can be seen in Figure 3.1.

Each TKR module has 18 horizontal tracker planes and in each plane an array of silicon-strip detectors (SSDs) is equipped to detect charged particles. The SSDs in each plane are composed of two layers of silicon strips, one extending in the x and the other in the y directions, thereby allowing us to localize the passage of a charged particle. The first 12 planes with tungsten plates which have 0.035 radiation length thickness are put in front of the SSD pairs, and thicker tungsten plates (0.18 radiation length) are put within the next 4 planes. The last 2 planes which are just in front of the CAL do not have tungsten plates. Note that radiation length is defined as the length in a material in which an electron loses 1 - e^{-1} of its energy by bremsstrahlung.

Gamma-rays incident from within the LAT's FOV are converted into an electron-positron pair in one of the TKR's tungsten plates. The directions of the electron and positron are determined from interaction points registered by the SSDs layers after the conversion point. Multiple scattering in the first few tungsten layers causes an angular deflection that is an unavoidable limit to the low energy angular resolution. Cosmic rays also interact within the TKR modules. Reconstruction of each event from the recorded tracks identifies the type of particle, its energy, and incident direction.

Each CAL module has 8 layers each of which consists of 12 CsI(Tl) crystals and are put in an alternating orthogonal manner. The crystals are read out by two PIN diodes at each end. The CAL's segmentation and read-out yield precise three-dimensional localization of the particle shower in the CAL. The CAL's depth is 8.5 radiation lengths at normal incidence. The CAL is a total absorption calorimeter with excellent energy resolution.

The ACD is composed of segmented 89 plastic scintillator tiles, and supplemented with fiber ribbons. The plastic scintillators are read out by waveshifting fibers connected to one PMT at each end.

3.2.3 In-orbit LAT performance

The LAT performance is mainly governed by three things, namely LAT hardware design, event reconstruction algorithms, and background selections and event quality selections. These are described by instrument response functions (IRFs) as a function of photon energy, incidence angle, conversion point within the instrument, and other important parameters. The version of IRFs we utilized in this thesis are Pass 7 version 6, which were developed post-launch using information obtained from flight data. The most evident

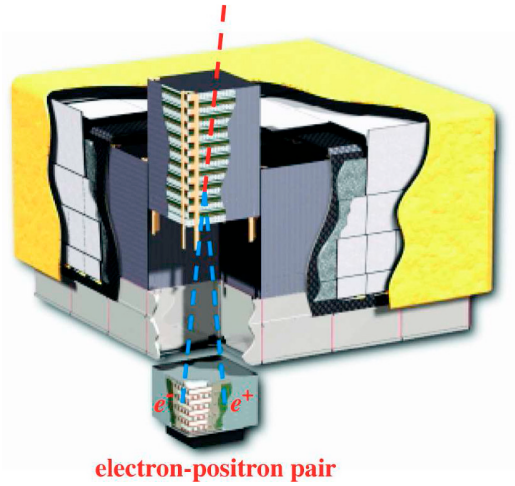

Figure 3.1: Schematic view of the Large Area Telescope onboard *Fermi*. Calorimeters are put below Silicon-strip layers and the overall detector system is surrounded by plastic scintillators to reject particles. The telescope's dimensions are 1.8 m×1.8 m×0.72 m. The power required and the mass are 650 W and 2789 kg, respectively (Hays (2010)).

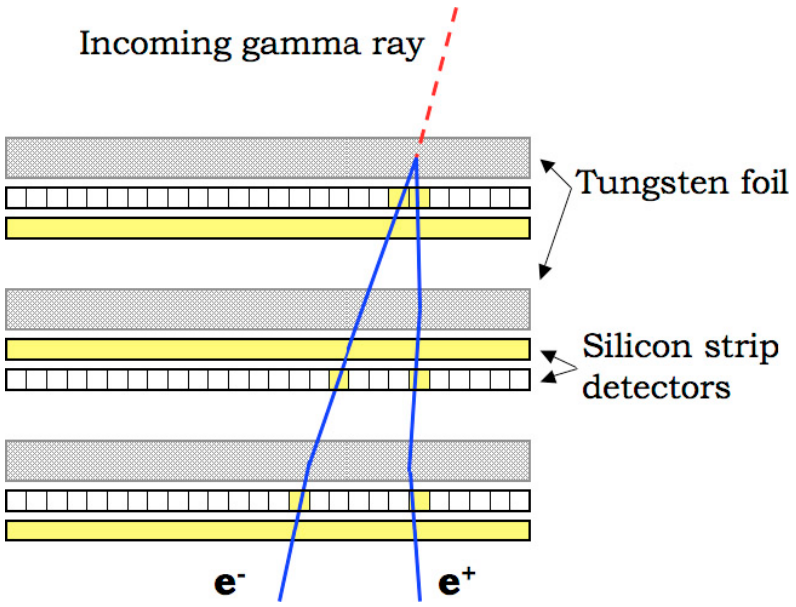

Figure 3.2: Zoomed-up schematic view of pair conversion and propagation processed within the TKR layers in the LAT (Hays (2010)).

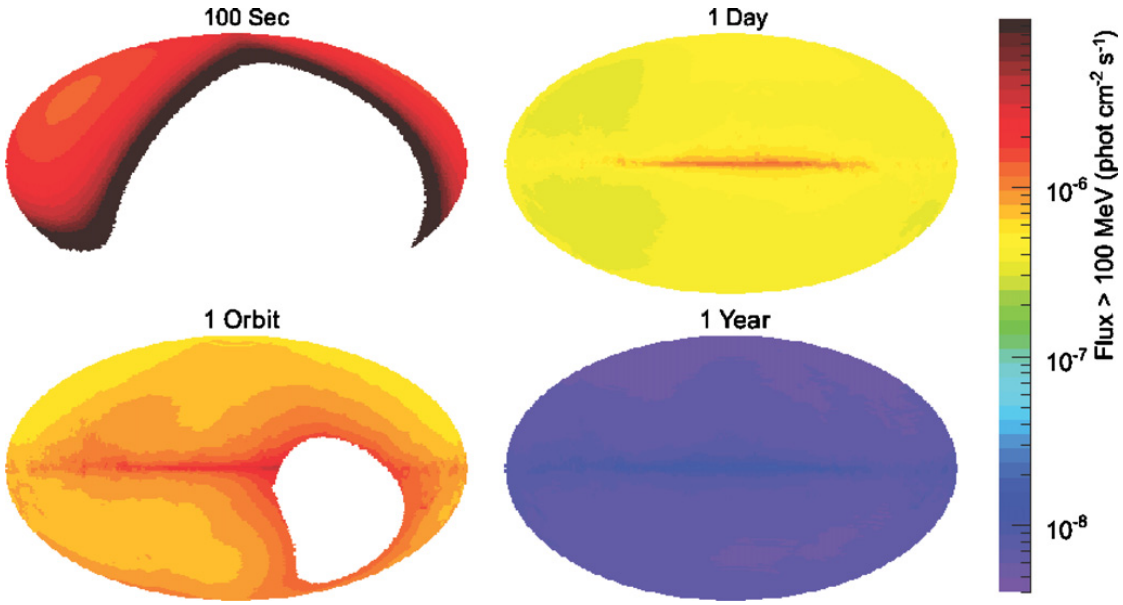

Figure 3.3: A figure illustrating LAT exposures on various timescales, which was taken from Atwood et al. (2009). Each map is an Aitoff projection in galactic coordinates. Nearly uniform exposure would be achieved every two orbits in nominal all sky survey mode. As a result, every point in the sky is viewed for ∼30 minutes every 3 hr.

on-orbit effects such as pile-up effect which occurs when cosmic rays arrive at almost the same time are taken into account when they constructed the response function by the Monte Carlo simulations.

Energy dependence of PSF and effective area of LAT are shown in Figure 3.4. The PSF means accuracy of an incident direction measured by the LAT, which is quantified as angles from the reconstructed incident direction which contains a certain fraction of all the incoming photons. The figure shows that the PSF strongly depends on energy.

Finally, all sky map obtained by 1-year *Fermi*-LAT is shown in Figure 3.5. We can see many bright point sources located in high latitude. Most of them are blazars. Blazars constitute significant fraction among the 1873 sources detected by the first 2-year survey of LAT, which will be discussed in the next chapter.

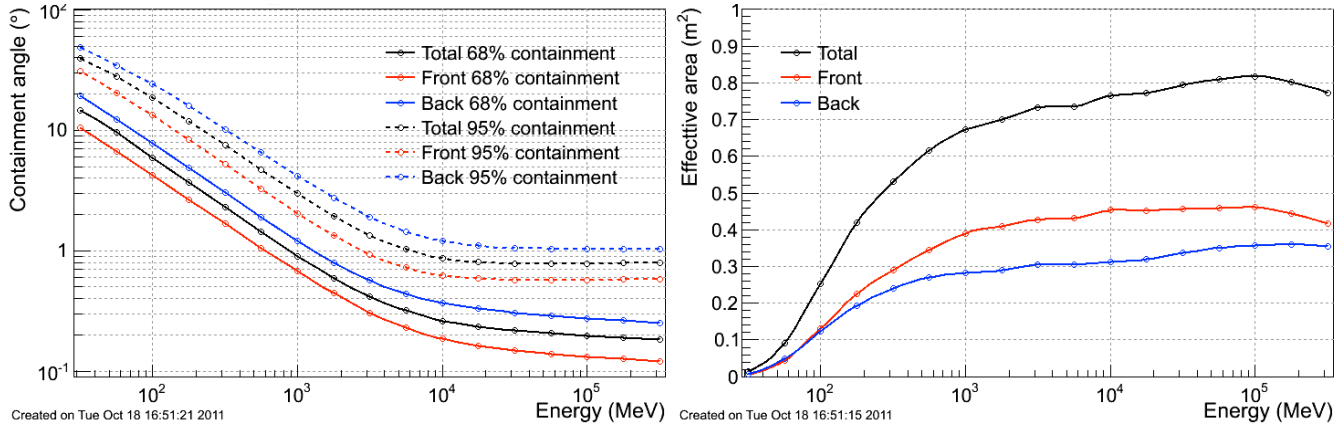

Figure 3.4: LAT PSF and effective area as a function of energy, which is taken from `http://www.slac.stanford.edu/exp/glast/groups/canda/archive/pass7v6/lat_Performance.htm`.

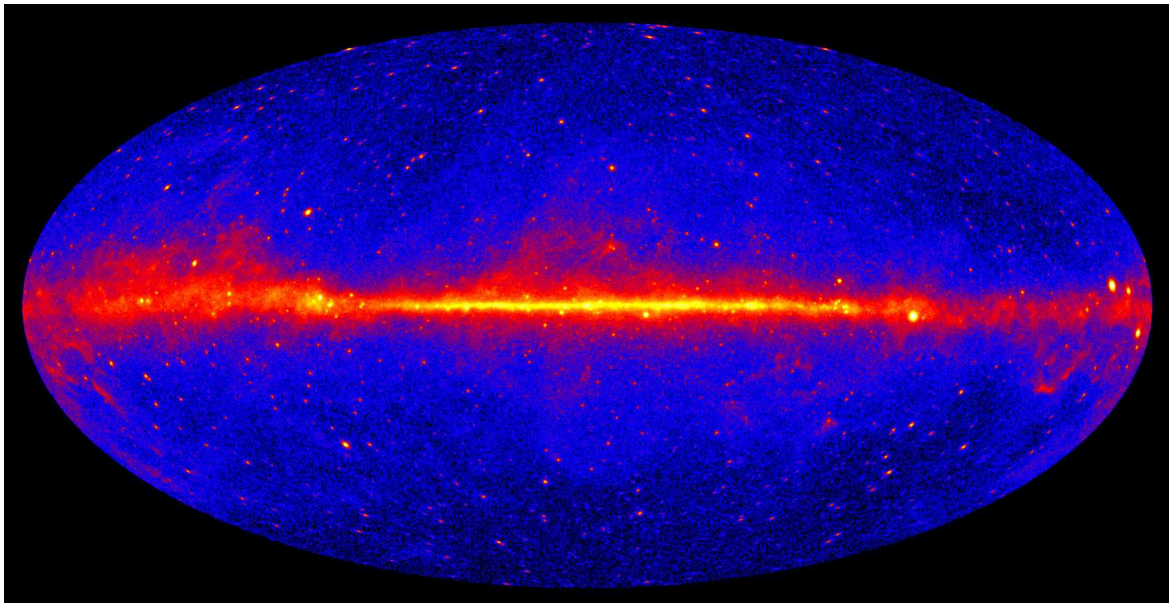

Figure 3.5: *Fermi*-LAT 5-year all sky map generated by using gamma-ray data over 1 GeV. Image Credit: NASA/DOE/Fermi LAT Collaboration.
(`http://fermi.gsfc.nasa.gov/ssc/`)

Chapter 4

The Brightest Blazar Flares Observed with *Fermi*-LAT

Thanks to the large effective area and high sensitivity of the LAT, we are able to study gamma-ray emitting objects with excellent statistics. As a result, a number of blazars have been detected by *Fermi* as variable sources with time scales as short as days or even hours, which had not been reported by studies with previous GeV gamma-ray instruments such as *EGRET* onboard *CGRO* satellite. This unprecedentedly good time resolution for GeV gamma-ray variability study would bring new insights about the blazar jets through their variability patterns, characteristic time scales, and so on. For this comprehensive study, the brightest (high-flux) sample of blazars with the best photon statistics is indispensable. In this chapter, we performed flux-limited selection of the 10 brightest flaring periods from the currently best blazar sample available from 5 year all sky survey data of *Fermi*-LAT.

4.1 Blazars Detected with *Fermi*-LAT

By August 2010, 1,873 gamma-ray sources have been detected with 5σ confidence level during the first 24 month-long *Fermi*-LAT all sky survey which began on 2008 August 4. These sources are included in "the second *Fermi*-LAT catalog (2FGL)" (Nolan et al. 2012) with their associated classifications. (See Figure 4.1) Among them, the detected 436 BL Lac objects and 370 FSRQs account for more than 40% of all the 2FGL sources. We also note that there should be additional contribution to the blazar population from 833 possible blazar candidates classified as "uncertain type AGN" or unassociated sources.

The *Fermi* blazars show characteristic trend on their flux-index plots, as shown in

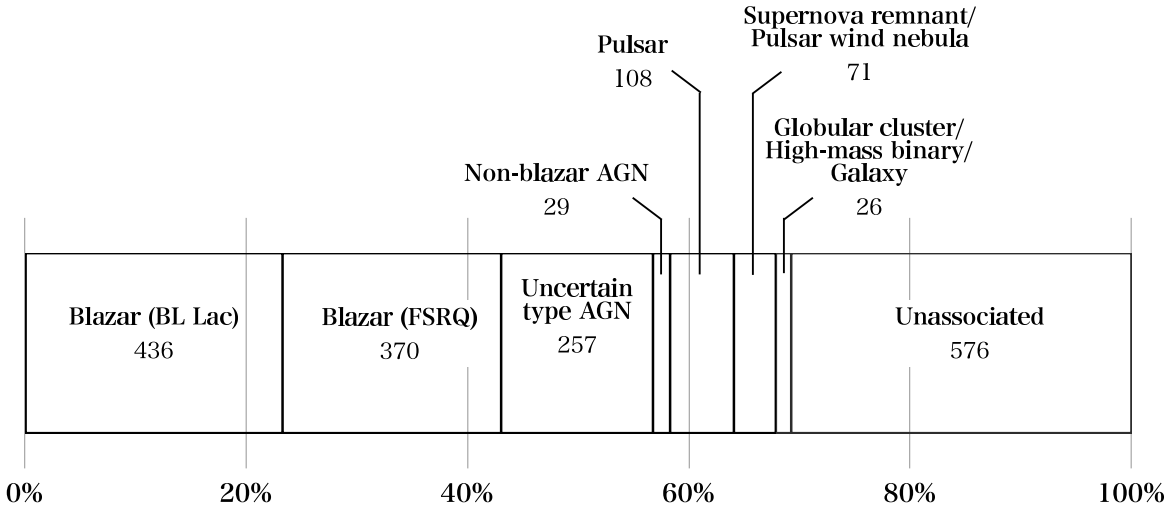

Figure 4.1: Association of the 1,873 2FGL sources.(referred from Nolan et al. 2012)

Figure 4.2. In this figure, no blazars are found in the upper-left region mostly because of the detection limit of *Fermi*-LAT. A source which has hard spectral shape has more high energy photons compared with a softer one, which makes it easy to be detected even with low photon statistics. On the other hand, there is a clear trend that the GeV spectrum of blazars get softer as blazars become brighter. Figure 4.2 shows that there are actually no blazars with high flux and hard spectral shape. This trend coincides with what one expects from the blazar diagram (Fossati et al. (1998)), namely the peak frequency of inverse Compton scattering becomes smaller as the source becomes brighter. Note that Kubo et al. (1998) also claimed that the relativistic electrons are accelerated to higher energies in BL Lacs, thus the GeV photon index become steeper in these objects.

We should be careful that the brightest flares do not always happen in the brightest sources in average. Since what we are interested in is a detailed study during flares, we need to collect a sample of the brightest flares. Both the flux and the index value are "averaged" over the first 24 months LAT survey in Figure 4.2. Since blazars show drastic variability in apparently random timescales, from years to months, days and even shorter scales, the averaged flux would wipe off possible huge variability on short timescales. Thus we need to proceed to investigate variability in each blazar for obtaining the complete flaring sample.

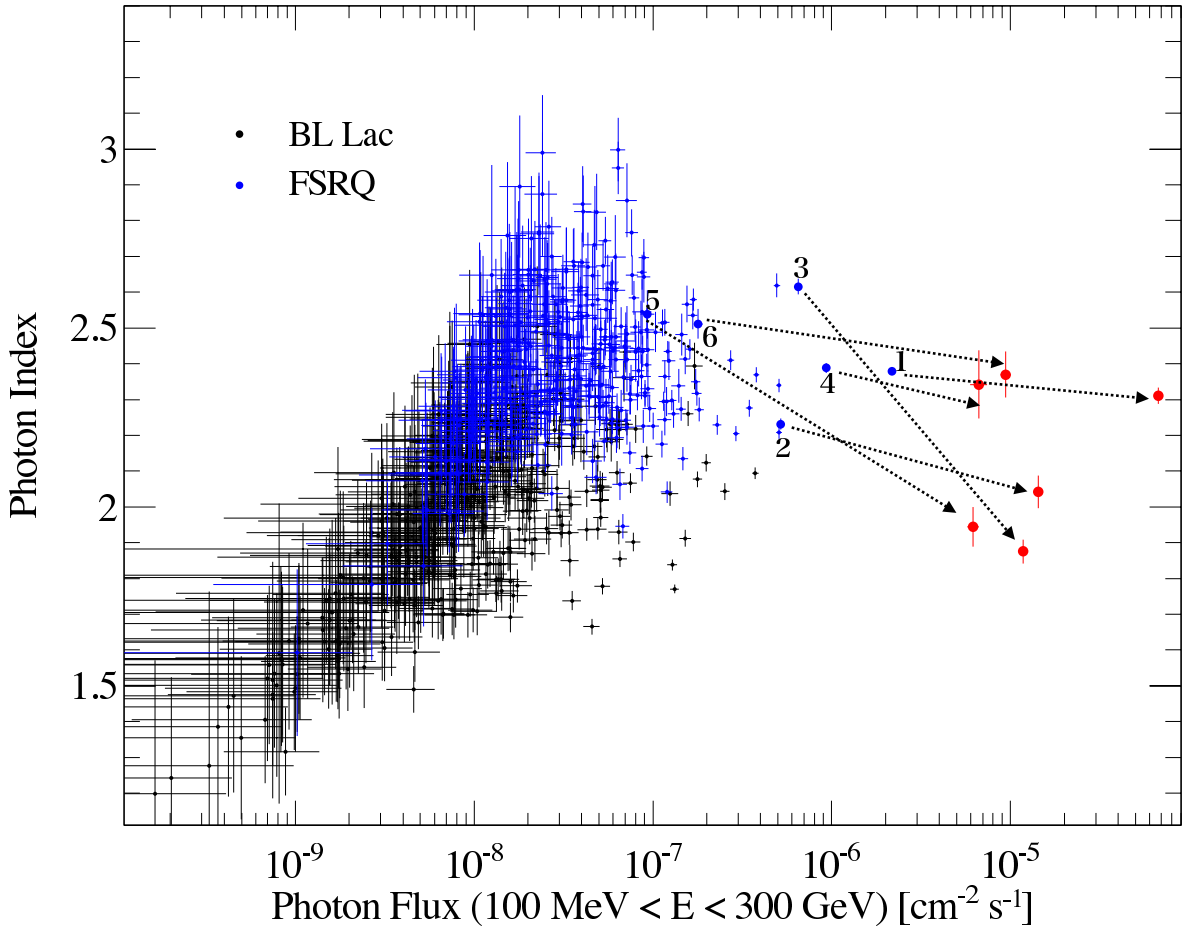

Figure 4.2: Relation of averaged flux and photon spectral index for all the 2FGL blazars (436 BL Lacs and 370 FSRQs). Large blue points represent the brightest blazars selected in this chapter. 1: 3C 454.3, 2: PKS 1510–089, 3: 4C 21.35, 4: 3C 273, 5: CTA 102, 6: PKS 0402–362. Red points represent maximum daily flux and index for the sources.

4.2 The Brightest Blazars in GeV Gamma-ray

4.2.1 *Fermi*-LAT Monitored Sources

We selected the intervals with the highest flux from all the accumulated data of blazars of *Fermi*-LAT survey. As blazars are generally variable on various timescales, collecting blazars with the highest averaged flux is not enough for collecting the brightest flares from all the blazars. We referred to "*Fermi*-LAT Monitored Sources list" for selecting blazars which had experienced bright states in the past 5 years of LAT survey.

Fermi-LAT Science Support Center monitors flux values for a number of bright sources and transient sources(not only blazars) that have shown flares during the mission. As sources exceeded the monitoring flux threshold of 1×10^{-6} cm^{-2}s^{-1}, they are added to the monitored source list. (The initial flux threshold was 2×10^{-6} cm^{-2}s^{-1}, but this value was lowered in June 2009.) Daily-binned and weekly-binned light curves of these sources after they crossed the threshold value for the first time are provided[1]. This monitored source list is being kept updated automatically everyday. They note that source fluxes in the list may have variations of up to 10% uncertainties in addition to overall normalization uncertainties, caused by currently-uncorrected dependencies of the gamma-ray detection efficiency on variations of the particle background in orbit due to preliminary instrument response functions and calibrations.

Currently there are 109 sources in the monitored source list (October 21, 2013). We performed automated search for determining their associations with 2FGL sources, by searching for 2FGL counterparts of the monitored sources. We imposed a condition that the position of the monitored source is included by only one 2FGL source within 95% confidence error radius of the 2FGL source. The results are listed in Figure 4.3. The list consists of 59 FSRQs, 22 BL Lacs, 2 Seyfert galaxies, 2 non-blazar AGN, 1 radio galaxy, 6 uncertain type AGN and 1 high-mass binary. We also note remaining 15 sources were not associated with any source in 2FGL catalog, given 95% confidence error of 2FGL source positions. These sources were newly detected sources after 2FGL catalog was published. Now we have extracted 81 blazars with 15 possible blazar candidates with flux-limited selection from $\sim$ 1000 blazars in the 2FGL catalog.

4.2.2 Selection of the Brightest Blazars

At first, we selected blazars which had been in high flux state at its daily maximum from the monitored source list as in 2013 October 21. The maximum daily flux for 109

[1]Light curves are available at `http://fermi.gsfc.nasa.gov/ssc/data/access/lat/msl_lc/`.

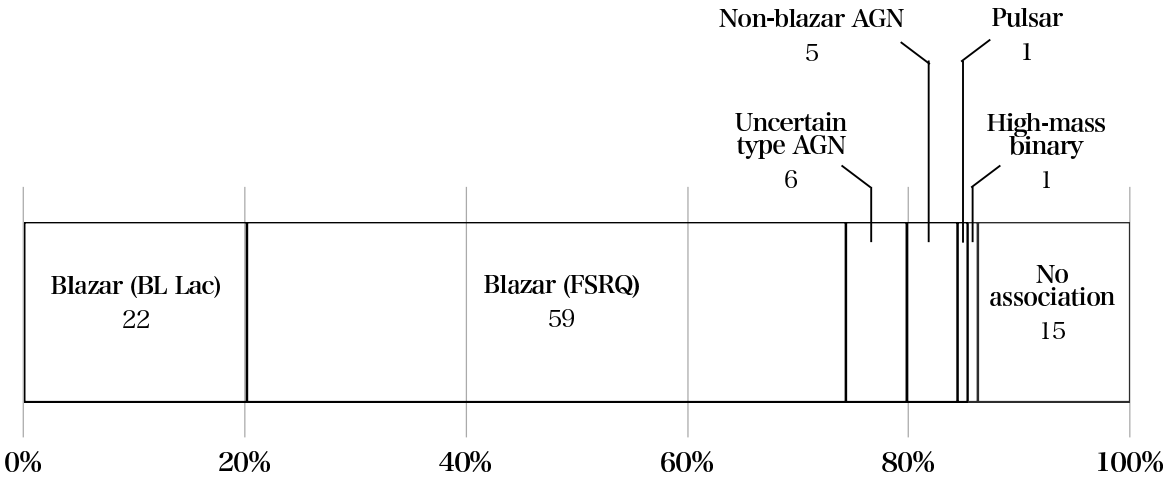

Figure 4.3: Associations for 109 monitored sources. (made from the *Fermi*-LAT monitored source list in October 2013 and the 2FGL catalog.)

monitored sources are presented in Figure 4.4. For extracting the blazars which had large flares, here we set a flux criterion of 5×10^{-6} ph s^{-1} cm^{-2} in 100 MeV – 300 GeV for the source selection. Only 7 objects exceeded this value at their maximum daily fluxes in the past 62 months *Fermi*-LAT survey (MJD 54682 – 56348; 2008 August 4 – 2013 October 21). One of them is Crab pulsar, and all the remainings are FSRQ type blazars which are located away from the Galactic plane ($|b| > 10°$), namely 3C 454.3, PKS 1510–089, 4C 21.35, 3C 273, CTA 102 and PKS 0402–362. These blazars also constitute the brightest population on the 24-month averaged flux value presented in 2FGL catalog (see Figure 4.2).

4.3 Interval Definition of Flares

We need to define the flaring intervals from the six brightest blazars in the next step. In general, we can see very spiky variability with gradually changing components in blazar light curves, and it is difficult to find typical time scale or periodicity in variability of blazars. Thus the definition of a flare is not obvious and one cannot distinguish a flare from a "quiescent" state clearly, which requires a rigorous definition of flaring intervals to proceed the systematic study performed in this work.

Here we propose a method for interval definition of flaring states by using a duty

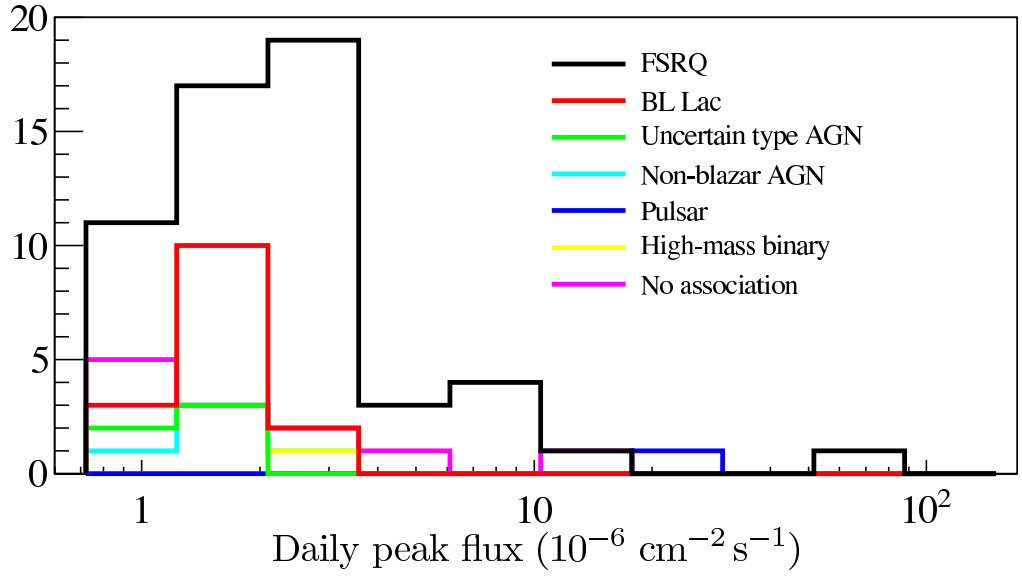

Figure 4.4: Maximum daily flux values of the 109 monitored sources, measured in the energy range of 100 MeV $<$ E $<$ 300 GeV.

cycle of each blazar. At first we set a flux threshold above which each blazar spends 5% of the total number of observing days, and extract intervals in which every observed daily flux value exceeded the threshold in the next step. We applied this method of definition to the 6 blazars selected above.

For calculating flaring intervals, we created daily-binned light curves of 62-month *Fermi*-LAT observation utilizing likelihood analysis method described in chapter 5. The light curves in the monitored source list were not used for two reasons. First, sources in the monitored source list started to be monitored after they first exceeded the threshold flux. In other words, daily flux data before they exceeded the threshold do not appear in the monitored source list even though the sources may be detected at a significant confidence level. This causes the bias when defining threshold value using only the daily flux values recorded in light curves of the monitored sources. Second, a significance of the detection and flux upper limits are useful information for characterizing variability properties, which are however missing in the monitored source list for particular dates (2010-09-14 to 2011-02-21). For these reasons, we performed standard likelihood analysis using event data in the energy range of 100 MeV – 300 GeV utilizing a science tool software provided by *Fermi*-LAT team. Details in the analysis are exactly the same as is described in chapter 5, namely assuming power law spectral shape for the blazars with

photon index and flux set free in the maximum likelihood procedure. Time intervals without significant detection more than 5 σ were eliminated from the flux calculation procedure. Instead, upper limit computation of 95% confidence level was done for these dates. Figure 4.6 and Figure 4.7 show the derived daily light curves of five years.

Figure 4.5 shows the duty cycles for the 6 selected blazars calculated based on 62 months of *Fermi*-LAT daily flux data. Vertical dotted lines indicate the 5% highest flux threshold out of 62-month observation for each blazar. Daily flux determined with more than 5σ significance is presented as black histogram, while red histogram represents upper limit flux values for days with lower significance level. Only the daily data with more than 5σ significance are used for counting the number of bright days, whereas all the data points including dates with upper limits are used for counting the total number of observed days for making the 5% threshould. The flux threshold values are 8.68×10^{-6}, 3.16×10^{-6}, 1.75×10^{-6}, 1.39×10^{-6}, 0.94×10^{-6} and 0.49×10^{-6} ph cm^{-2} s^{-1} for 3C 454.3, PKS 1510–089, 4C 21.35, 3C 273, CTA 102 and PKS 0402–362, respectively.

Finally, flaring periods of these blazars were collected by extracting continuous intervals in which daily fluxes stay over the thresholds for each blazar, together with 1 day extra margin before and after the periods. Intervals with peak flux value exceeding 5.0×10^{-6} ph cm^{-2} s^{-1} are listed in Table 4.1. We selected 10 brightest flares, which is #1 - #9, and #12 in the table, which were analysed in this paper. In this step, intervals whose flux peaks exceeds the threshould for only one day were excluded since those are not suitable for studying flaring profiles in detail. We note all the selected 10 flares have peak fluxes above 5.0×10^{-6} ph cm^{-2} s^{-1}, that makes the selected intervals independent of the threshold value of 5.0×10^{-6} ph cm^{-2} s^{-1} we defined when selecting bright blazars from the monitored source list.

4.4 Properties of the Brightest Blazars

The six selected blazars are flat spectrum radio quasars (FSRQs) that emit majority of their radiatively dissipated energy in GeV gamma-rays. Properties of these blazars are summarized in Table 4.2. All the selected flaring intervals of the brightest blazars have maximum daily flux values over 8×10^{-6} ph s^{-1} cm^{-2} in energy range of 100 MeV $<$ E $<$ 300 GeV, that are extremely bright samples among all the GeV gamma-ray emitters. These selected blazars were overwhelmingly brighter than other neighboring sources over entire LAT energy range as is inferred from count maps for the selected flares presented in Figure 4.8. There are only small contamination from the Galactic and extragalactic diffuse components which would be dealt in chapter 6.

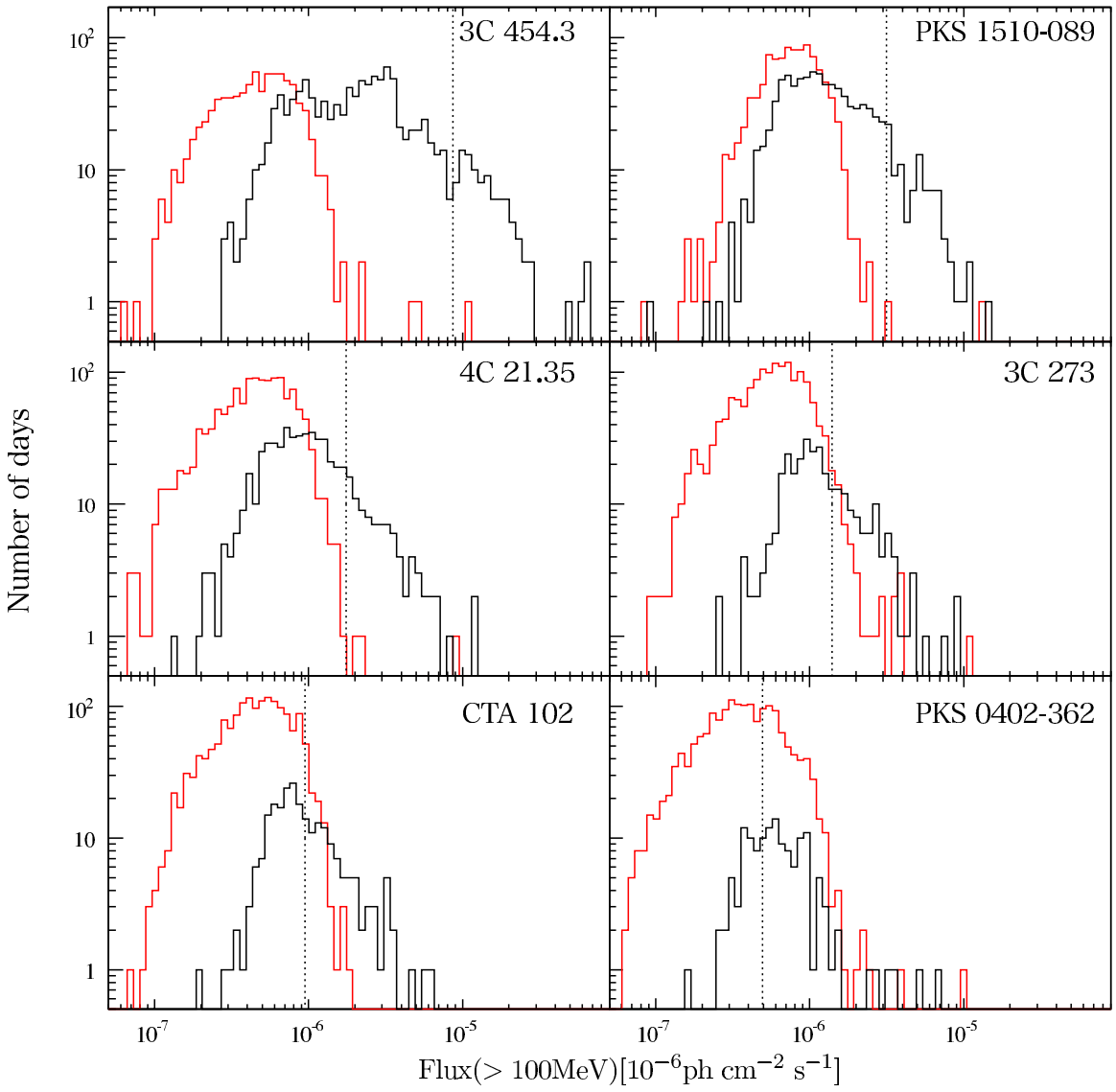

Figure 4.5: Duty cycles of the selected blazars created by *Fermi* LAT daily flux of 62 months. Daily flux value was calculated via likelihood analysis over 100 MeV. Black histograms represent daily flux value when TS value was above 25. Red histograms represent 95% upper limit flux value when daily flux is under 25. Vertical dotted lines shows 5% flux threshold out of 62 months observation.

Table 4.1: Flaring periods with peak flux values above 5.0×10^{-6} ph cm^{-2} s^{-1}. "*" mark means that only single day is over the flux threshold, which is excluded in this study.

ID	Source	MJD_{Start}	MJD_{Stop}	$F_{peak}[10^{-6}$ ph s^{-1} cm$^{-2}]$
1	3C 454.3	55501	55558	67.38
2	3C 454.3	55164	55177	20.10
3	3C 454.3	55561	55572	18.39
4	3C 454.3	55287	55305	15.02
5	PKS 1510-089	55850	55856	14.32
6	4C 21.35	55307	55319	11.82
7	4C 21.35	55362	55393	11.69
8	PKS 1510-089	55865	55878	11.27
9	3C 273	55088	55113	9.43
*10	3C 454.3	55304	55307	8.97
*11	3C 454.3	55194	55197	8.79
12	PKS 1510-089	54944	54955	8.73
13	PKS 1510-089	54913	54919	8.03
14	PKS 1510-089	55743	55748	7.91
15	PKS 1510-089	55979	55995	7.12
16	PKS 1510-089	56552	56560	6.79
17	PKS 0402-362	55820	55915	6.68
18	PKS 1510-089	55997	56005	6.44
19	4C 21.35	55339	55346	6.41
20	CTA 102	56187	56213	6.20
*21	PKS 1510-089	54960	54963	5.87
*22	PKS 1510-089	55766	55769	5.76
23	4C 21.35	55355	55363	5.42
24	PKS 1510-089	55957	55964	5.29
*25	PKS 1510-089	56563	56566	5.27
26	4C 21.35	55232	55241	5.21
27	PKS 1510-089	54844	54848	5.01

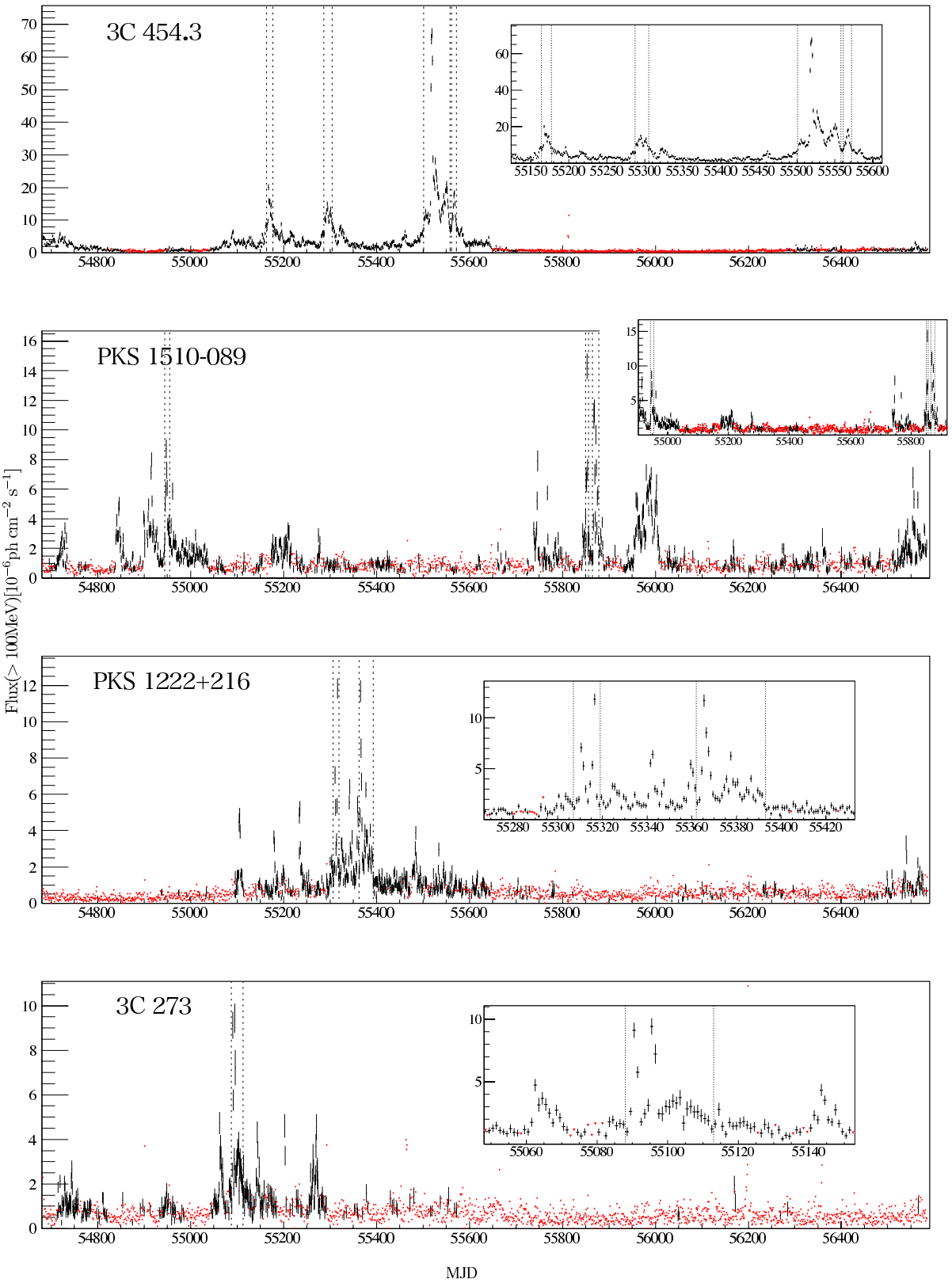

Figure 4.6: 62-month LAT light curves of the brightest blazars with daily binning. Red triangles represent upper limits with 95% confidence level, calculated for points with daily TS value less than 25. Vertical dotted lines show flaring intervals analysed in this paper.

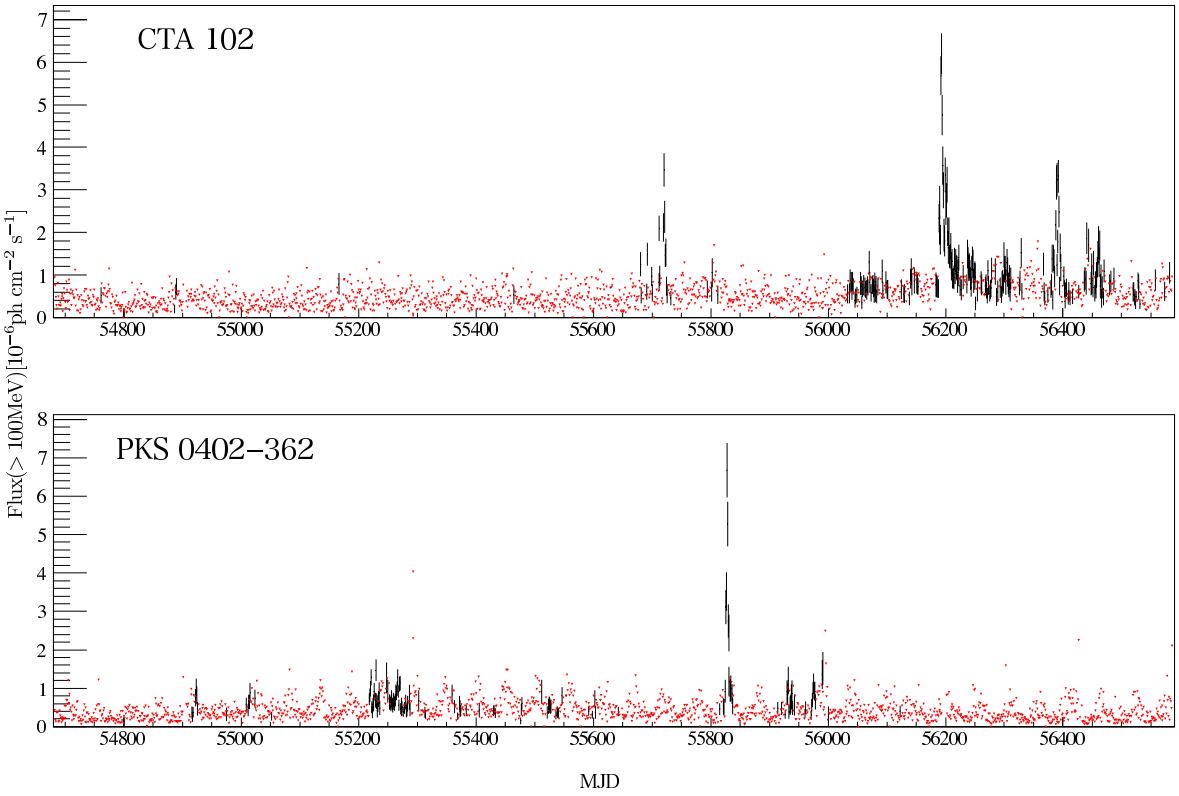

Figure 4.7: 62-month LAT light curves created in the same manner as Figure 4.6.

Table 4.2: Properties of the selected blazars. Viewing angle, bulk Lorentz factor, and Doppler factor for the blazars are referred from Hovatta et al. 2009.

Source Name	RA (L)	DEC (B)	Type	z	Viewing angle(°)	Lorentz factor	Doppler factor
3C 454.3	343.49 (86.11)	16.15 (-38.18)	HPQ	0.859	1.3	19.9	33.2
PKS 1510-089	228.21 (351.29)	-9.10 (40.14)	HPQ	0.36	3.4	20.7	16.7
4C21.35	186.23 (255.07)	21.38 (81.66)	LPQ	0.43	5.1	45.5	5.2
3C 273	187.28 (289.95)	2.05 (64.36)	LPQ	0.16	3.3	14.0	17.0

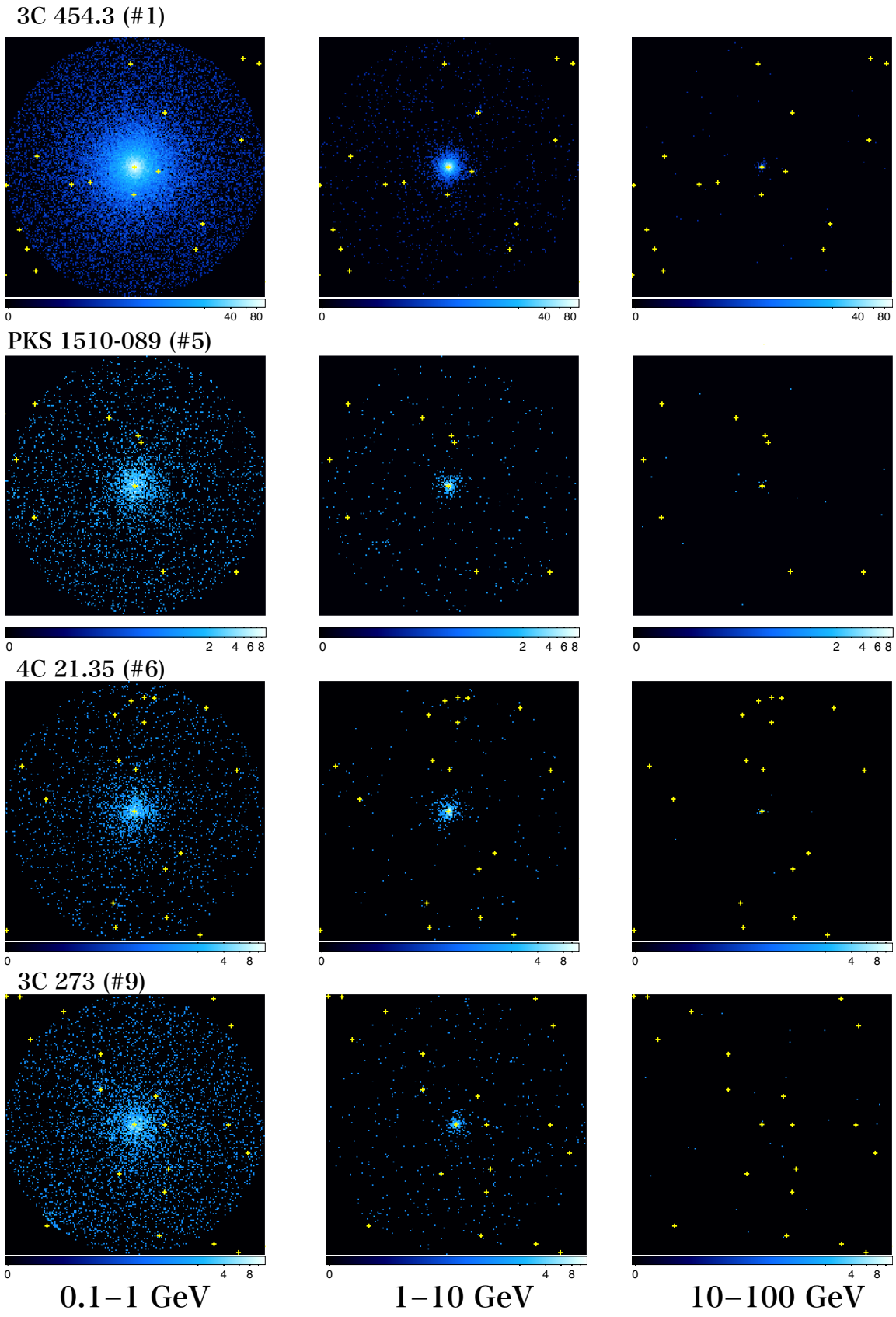

Figure 4.8: Count maps for the selected flares within 10° radius around the blazars. Yellow crosses represent positions of 2FGL sources which were detected above 5σ significance in the first 2-year of *Fermi*-LAT all sky survey.

Chapter 5

Systematic Analysis of Short Time Variability

Most of the contemporary blazar investigations with *Fermi*-LAT have utilized data integrated for relatively long time duration such as days or months due to the limited photon statistics. We should keep in mind that such data integrated for long duration not only obscure rising and decaying profile of variability but also mask fine structures of flares which last for less than days. Moreover such short variability of blazars in GeV range are indeed quite possible considering rapid variability reported in other wavelength, such as sub-daily variability in X-ray, and sub-hour variability recently detected in TeV gamma-ray and optical band. Photon statistics of the sample of blazar flares collected in the previous chapter have never been available in GeV energy range before, and now we can study hour-scale variability for the first time in this range. In this chapter, we search for variability in the selected blazars with timescale as short as 3 hours, which is possible only for these blazars with excellent photon statistics.

5.1 Data Reduction

5.1.1 Analysis Method

Standard data analysis method of *Fermi*-LAT is presented in this section. The LAT analysis is based on maximum likelihood method in order to treat the extent of the LAT PSF. The standard analysis software provided as "*Fermi*-LAT science tools"[1]. We briefly introduce the method of likelihood analysis below. See Mattox et al. (1996) for the throughout arguments.

[1] *Fermi*-LAT science tools are available at `http://fermi.gsfc.nasa.gov/ssc/data/analysis/software/`

Maximum Likelihood Analysis

The likelihood equals the probability of the data observed given a predicted model of high energy gamma-ray emission. The likelihood analysis for the LAT utilizes a gamma-ray count map, and a corresponding exposure map provides the exposure ($\mathrm{cm}^2\,\mathrm{s}\,\mathrm{sr}$) for each pixel. In the case of *Fermi*-LAT analysis, the predicted model consists of the distribution of gamma-ray sources in the sky, and flux and spectral shape of each source. The model parameters are estimated by maximizing the likelihood. The likelihood is written as the product of the probability of observed counts for each pixel on a count map.

$$L = \prod_{i,\,j} p_{ij} \tag{5.1}$$

where

$$p_{ij} = \frac{\theta_{ij}^{n_{ij}} e^{-\theta_{ij}}}{n_{ij}!} \tag{5.2}$$

is the Poisson probability that n_{ij} counts are observed in pixel ij when the predicted number of counts in the pixel by the model is θ_{ij}. The logarithm of the likelihood is used.

$$\ln L = \sum_{i,\,j} n_{ij} \ln(\theta_{ij}) - \sum_{i,\,j} \theta_{ij} - \sum_{i,\,j} \ln(n_{ij}!) \tag{5.3}$$

Since the last term is model independent, it can be eliminated for the parameter estimation. The second term represents a total number of predicted counts on the count map, thus can be written as $\sum_{i,\,j} \theta_{i,\,j} = N_{\mathrm{pred}}$. Then the above equation can be rewritten as,

$$\ln L = \sum_{i,\,j} n_{ij} \ln(\theta_{ij}) - N_{\mathrm{pred}} \tag{5.4}$$

In the likelihood analysis of the LAT data, we run `gtlike` in the standard analysis package for performing maximum likelihood fit to optimize spectral parameters of the input model. The `gtlike` could be performed in two ways, namely unbinned and binned likelihood analysis. The binned analysis divides observed data into bins which have finite sizes in energy and spatial position, that are specified by the user. Note that the data are integrated over the full time interval, thus information of arrival time for each photon is abandoned. A bin may include more than two photons. Since the binning decrease the information, smaller bins would bring more accurate likelihood. In this sense, the unbinned likelihood analysis offer us the most accurate estimations of parameters since it utilizes bins with infinitesimally small size that every pixel includes at most one photon. (See 6.1.1 for more general arguments for unbinned likelihood analysis.) The following analysis performed in this chapter was done by unbinned likelihood analysis.

Test Statistic

The likelihood ratio is often used for comparing different predicted models. The ratio of likelihood when there is no point source at the position under consideration (null hypothesis; L_0) and the likelihood when there is a point source there (alternative hypothesis; L_1) is defined as "test statistic", which is given by,

$$\mathrm{TS} = -2(\ln L_0 - \ln L_1) \tag{5.5}$$

According to the Wilks's theorem (Wilks (1938)), TS is distributed as χ^2 with Δm degrees of freedom where Δm is the number of additional parameters that are optimized for the alternative hypothesis. Basically, the square root of the TS is approximately equal to the detection significance for a given source.

5.1.2 Event Selection of LAT Data

The data discussed in this chpater were collected from the brightest sample of blazar flares extracted in the previous chpater. Only the events with energies greater than 100 MeV were used in this analysis since current response functions (Pass 7, see chapter 3 for detail) have large systematic uncertainties in the parameter estimation below 100 MeV. Zenith angles $< 100°$ were included in this analysis. The maximum zenith angle selection is designed to exclude time periods when any portion of the region of interest is close to the Earth's limb, which causes higher background levels. The Earth's limb lies at a zenith angle of 113°, that means the zenith cut with 100° provides protection against significant contamination by atmospheric gamma-ray. We selected good time intervals (GTIs) by using a logical filter of "`DATA_QUAL==1`" and "`LAT_CONFIG==1`", which excludes time periods when some spacecraft event has affected the quality of the data.

5.1.3 Source Modeling

We should consider contributions from nearby sources even if we want to analyse one particular source, because LAT PSF is large at lower energy (68% containment angle at 100 MeV is 3.5 degree; see Table 3.1). Therefore we should choose sufficiently large region of interest (ROI) in order not to miss source photons. In the following analysis, the gamma-ray photons were extracted from a circular ROI with radius of 10°, centered at the radio position of the four selected blazars.

Point Sources

The target blazar and other point sources within the ROI and the surrounding 5°-wide annulus taken from the second-year LAT catalog (Nolan et al. (2012)) were considered for the source model of each blazar. In addition, for each interval of flares analysed in this chapter, count maps were made to check if there were another bright nearby sources that should be considered in this source modeling.

We approximated the gamma-ray emission of the selected blazars with a simple power-law model, keeping both photon indices and fluxes free. For the other point sources within 10° radius around the target blazar, normalizations were set free, while spectral parameters (e.g. index) were fixed following the second-year LAT catalog. For the point sources located in the surrounding 5°-wide annulus, all the parameters were fixed following the second-year LAT catalog. For each time bin analysed, point sources with the test statistic (TS) values ≤ 0 were removed from the source model, since these sources are extremely faint and introduce unnecessary degree of freedom for the maximum likelihood procedure.

Diffuse Sources

In addition to the nearby sources, diffuse emission from the Galactic plane and unresolved isotropic emission from extragalactic sources contribute the observed count maps. The Galactic diffuse emission template version "`gal_2yearp7v6_v0.fits`" and the isotropic diffuse emission template version "`iso_p7v6source.txt`" were assumed in the modeling. "`gal_2yearp7v6_v0.fits`" is a spatial and spectral template, which was developed by deriving the distribution of interstellar gas from spectral line surveys of H_I and CO (as a tracer of H_2) in Galactocentric rings. "`iso_p7v6source.txt`" is an isotropic spectral template, which provides the spectral form by fitting the emissions at Galactic latitudes above 30 degree that includes both extragalactic diffuse gamma-rays and remaining residual cosmic-ray emission. In the following analysis of light curves, we fixed the fluxes of the diffuse emission components at the values obtained by fitting the data collected over the entire period of each flare.

As for the source modeling of PKS 1510−089, we included an additional variable gamma-ray point source located at (R.A., Dec.) = (233.168, −13.311), i.e. about 6.4° away from PKS 1510−089. This object, tentatively associated with the FSRQ TXS 1530–131 (Gasparrini & Cutini (2011)), did not appear in the 2FGL, although it was clearly detected

during the period MJD 55834 (2011 September 30) to MJD 55903 (2011 December 8) at relatively high flux level of $F_{>100\,\mathrm{MeV}} \simeq (1.1 \pm 0.1) \times 10^{-7}\,\mathrm{ph\,cm^{-2}\,s^{-1}}$.

5.2 Results of Systematic Analysis with 3-hour Binned Light Curves

We analysed the ten brightest flaring intervals selected in chapter 4 with 3-hour binned light curves. Since *Fermi*-LAT sweeps all the sky in 3 hours in its nominal mode, generally 3-hour binning is the minimal time binning for obtaining nearly constant exposure for each bin. The excellent photon statistics allowed us to study these flares with shorter time binning, down to the minimum 3 h dictated by the survey mode of the LAT instrument. Derived variability of photon flux and spectral index during the flares were shown in Figure 5.1 (3C 454.3), Figure 5.2 (PKS 1510–089), Figure 5.3 (4C 21.35), and Figure 5.4 (3C 273), respectively.

We assumed power law spectral shape for these blazars with flux and photon index set free, which are fitted by the maximum likelihood method for each bin in the light curves. In these figures, photon flux and index were calculated for bins with TS>10. 95% confidence level flux upper limits correspond to the detection significance values TS < 10, which is a conventional choice in the analysis of daily-binned light curves of bright LAT sources (see, e.g., Tavecchio et al., 2010; Orienti et al., 2013).

These figures clearly show there were high amplitude rapid variability in sub-daily timescale, moreover even as short as 3 hours, for all the selected blazars. On the other hand, the spectral indices during the flares are around 2.0, and become even harder during the huge outbursts. Photon spectral index of 2.0 corresponds a peak in the νF_ν SED, since $\nu F_\nu \propto E^2 F_{\mathrm{ph}} \propto E^{2-\gamma}$ where F_{ph} is photon flux at certain energy and γ is photon spectral index of power law. This means GeV gamma-ray is located at the peak of SED and the most luminous energy band in the inverse Compton spectrum.

Next, we confirmed how dramatically flux changes within the timescale of 3 hours. We performed systematic search for high-amplitude variability based on the 3-hour binned light curves for the ten selected flares. Flux ratios for every consecutive bins were calculated to pick up bins indicating high-amplitude variability. Consecutive points in the light curves which show the highest amplitude within 3 hours in the energy band 100 MeV – 300 GeV were summarized in Table 5.1. Since the bin-width is constant (3 hours), the highest amplitude variability means the shortest timescale of τ_d calculated as follows.

$$\tau_d = (t_2 - t_1) \times \frac{\ln 2}{\ln(F_2/F_1)} \tag{5.6}$$

Table 5.1 lists variability with both of consecutive bins have TS values larger than 25 and characteristic variability timescale τ_d calculated via Eq.(5.6) less than 2 hours, where F_i is the observed flux value at time t_i (i = 1,2). For rising phase ($F_2 > F_1$), τ_d represents duration it takes to flux increases by factor 2. For decaying phase ($F_2 < F_1$), $-\tau_d$ represents duration it takes to flux decreases by factor 2. Thus the formula of τ_d is widely used as flux doubling/halving timescale.

From this analysis, FSRQs were discovered to show high-amplitude variability with timescale as short as a few hours. Though flaring time profiles with the flux doubling timescales of the order of several hours has been reported for some other flaring FSRQs observed with LAT, namely PKS 1454–354 (Abdo et al. (2009a)) and PKS 1502+106 (Abdo et al. (2010a)) for example, their confidence level were low due to large errors related with lower flux level of the source. The selected sample of the brightest blazar flares allows us to investigate hour-scale variability with relatively small errors and discover the shortest variability timescale claimed for all the AGN in GeV so far.

Among the high-amplitude variability listed in Table 5.1, PKS 1510–089 showed the most spectacular variability by factor ∼6 in only 3 hours, which is the highest amplitude variability found in this analysis. Furthermore, the flux value of 45×10^{-6} cm^{-2} s^{-1} was extreme among the analysed intervals. Such a high amplitude and rapid variability would be masked in the conventional daily-binned analysis despite its importance for constraining physical parameters of jets.

5.3 Discussions on Very Rapid Gamma-ray Variability in PKS 1510–089

We discovered the variability with timescale of ∼1 hour in PKS 1510–089 from our analysis in 3-hour binning, which is indicated from flux change by factor of 6 in 3 hours (See Table 5.1). This is the shortest variability timescale found for all the blazars in GeV range. Our analysis showed rapid variability with the timescale of hours indeed exists for blazars in GeV energy range. Such a rapid variability could have been masked in conventional longer time binning so far. We discuss how apparent flaring profiles change by different time binning based on further analysis of #5 and #8 in PKS 1510–089, and implications of rapid variability for underlying physics in blazar jets.

Table 5.1: Summary of the highest amplitude flux variability observed in the selected flares of the brightest blazars, analysed based on 3-hour binned light curves. $F_1,\ F_2$ are photon fluxes of consecutive bins in the light curves. Unit of $T_1,\ T_2$ is MJD, and $F_1,\ F_2$ is 10^{-6} ph cm^{-2} s^{-1}(100 MeV – 300 GeV). Characteristic timescales are calculated for two consecutive bins with TS values larger than 25 (5σ) in both bins via Eq 5.6. The consecutive bins which show variability timescale $|\tau_d|$ (hours) less than 2 hours are listed below.

Flare ID	T_{start}	T_{stop}	F_1	F_2	$\lvert\tau_d\rvert$	Rise/Decay
PKS1510-089						
#5	55853.6875	55853.8125	7.76±4.50	44.81±4.55	1.19±0.40	Rise
#5	55853.0625	55853.1875	5.24±1.42	15.39±2.13	1.93±0.54	Rise
#5	55852.0625	55852.1875	13.27±2.00	4.54±1.40	1.94±0.62	Decay
#8	55869.0625	55869.1875	13.54±2.40	3.80±1.15	1.64±0.45	Decay
#12	54947.1875	54947.3125	4.10±1.86	15.17±4.37	1.59±0.65	Rise
4C 21.35						
#6	55317.4375	55317.5625	1.35±0.57	4.92±1.47	1.61±0.64	Rise
#7	55386.6875	55386.8125	1.49±0.68	5.60±1.30	1.57±0.61	Rise
#7	55369.5625	55369.6875	1.47±0.57	4.57±1.13	1.83±0.74	Rise
#7	55386.8125	55386.9375	5.60±1.30	1.80±0.79	1.83±0.80	Decay
3C 273						
#9	55094.9375	55095.0625	3.74±1.47	11.25±1.95	1.89±0.73	Rise

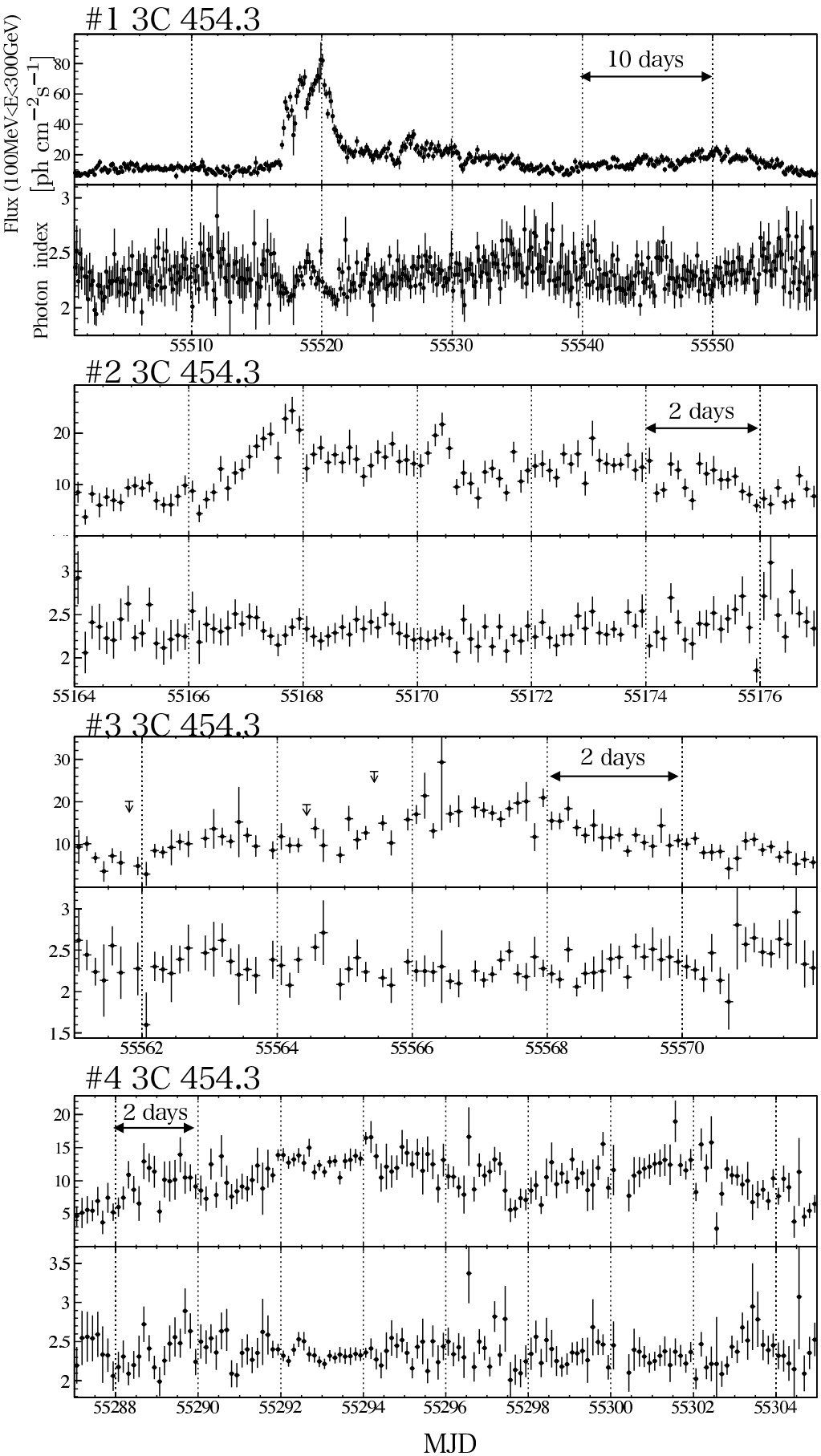

Figure 5.1: Flux and spectral variability during the selected flares in 3C 454.3 shown in 3-hour binned light curves.

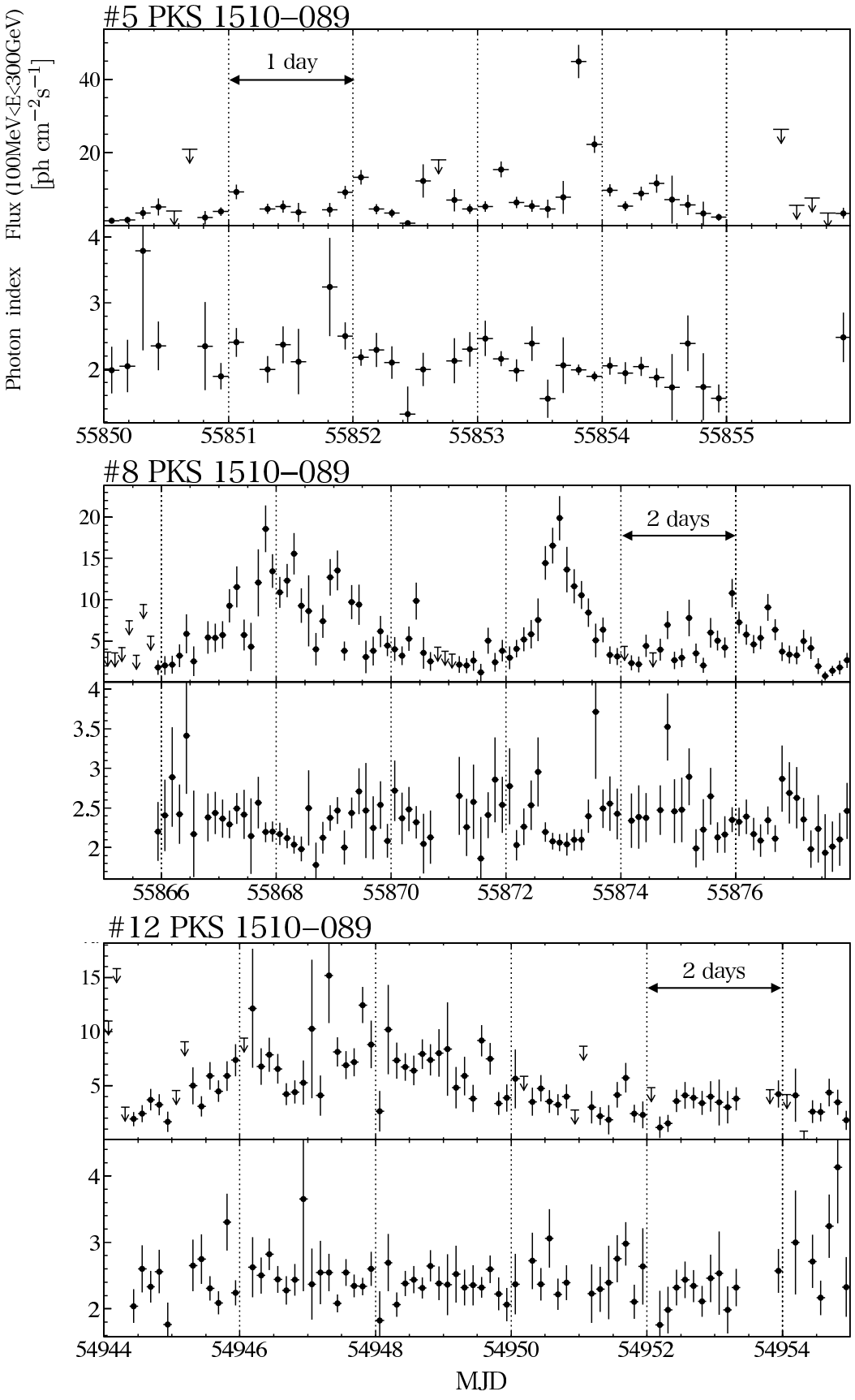

Figure 5.2: Flux and spectral variability during the selected flares in PKS 1510–089 shown in 3-hour binned light curves.

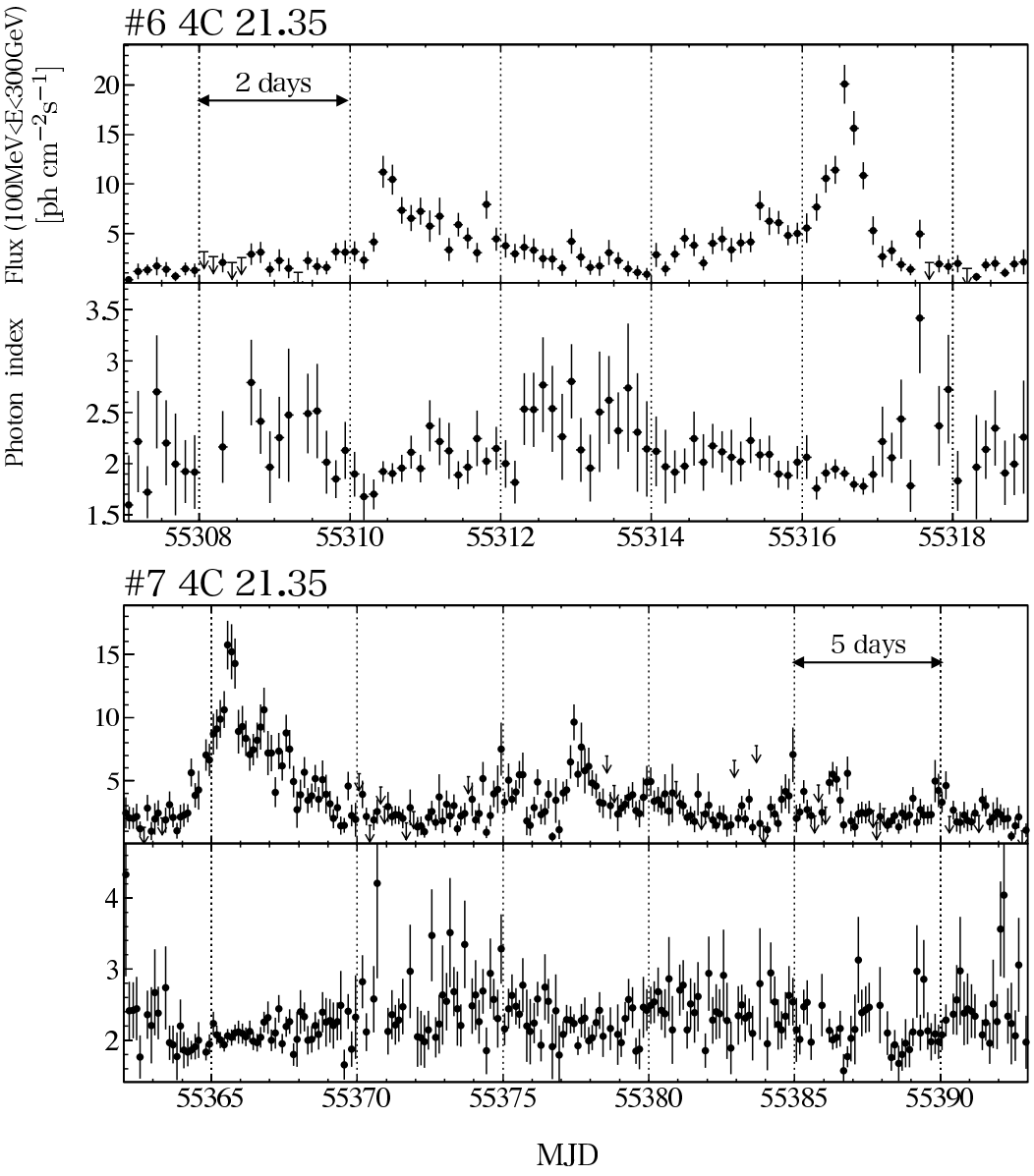

Figure 5.3: Flux and spectral variability during the selected flares in 4C 21.35 shown in 3-hour binned light curves.

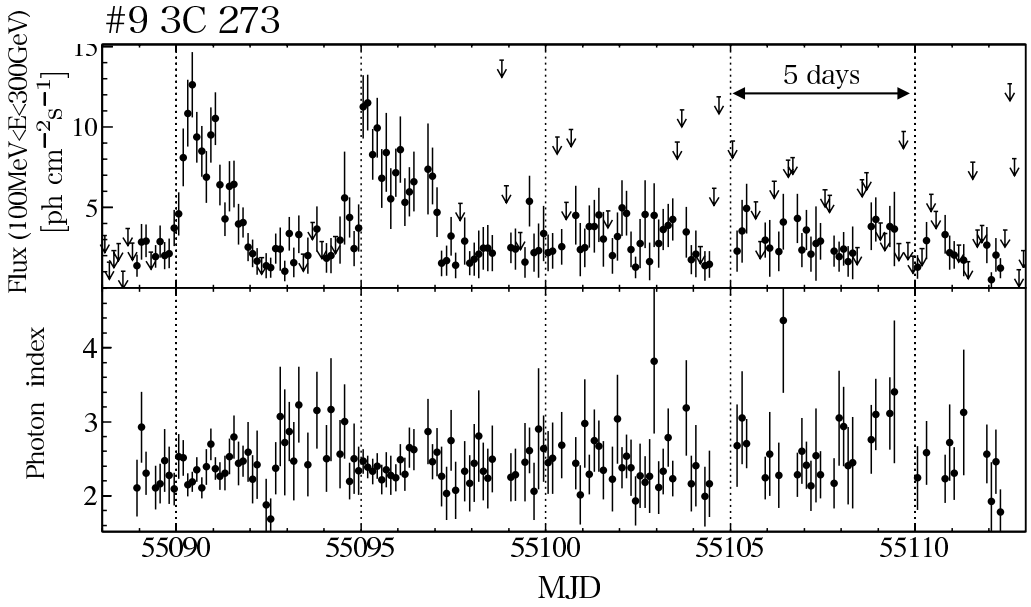

Figure 5.4: Flux and spectral variability during the selected flares in 3C 273 shown in 3-hour binned light curves.

5.3.1 Effect of Binning

Flaring interval of PKS 1510–089 including flare #5 and flare #8 were analysed in 24-hour, 12-hour, 6-hour, and 3-hour binning for clarifying how apparent characteristics of flares change and rapid variability of ∼hour appears. The analysis procedure is the same as is discussed in the previous section. Figure 5.5 presents the daily gamma-ray light curve of PKS 1510−089 at photon energies 0.1–300 GeV during the period 2011 September – December. As shown, during the discussed time interval three major high-amplitude gamma-ray outbursts of the source were detected with photon fluxes $F_{>100\,\mathrm{MeV}} \sim 10^{-5}\,\mathrm{ph\,cm^{-2}\,s^{-1}}$ and flux doubling timescales less than a day.

The upper left panel in Figure 5.6 presents the light curves of PKS 1510−089 around the time of the first major gamma-ray outburst, binned in the intervals of 12 h, 6 h, and 3 h (upper, middle, and lower panels, respectively). As shown, the rising segment of the flare is unresolved down to the timescale of 3 h.Previously all the high-amplitude flux changes of FSRQs detected in the GeV range were characterized by longer (≥ 1 d) timescales, while any shorter variability consisted of a small-amplitude flickering only. Here, instead, the recorded flux increases from about $F_1 \simeq 8 \times 10^{-6}\,\mathrm{ph\,cm^{-2}\,s^{-1}}$ up to $F_2 \simeq 45 \times 10^{-6}\,\mathrm{ph\,cm^{-2}\,s^{-1}}$ within 3 hours, giving formally the flux doubling timescale

of ∼1 hour only (See Table 5.1). This value should be considered as an upper limit only, because of a limited exposure of PKS 1510−089 during the analyzed 3 h visibility window. Interestingly, the decay segment of the flare seems to be marginally resolved with the 3-hour binning. Such an apparently well resolved decaying profile of rapid flare would provide crucial information for constraining blazar emission as is discussed in chapter 7.

The second gamma-ray outburst of PKS 1510−089 for which the LAT light curves in 12, 6, and 3 hours bins are presented in the upper right panel in Figure 5.6, constitutes a very different case. Here the flare seems to be resolved with 12-hour binning, displaying shorter exponential growth and a slower linear decay, as expected in most of the models of FSRQs' variability involving a fast injection of accelerated electrons and their slower radiative cooling dominated by the Comptonization of the soft photons produced externally to the jet (e.g., Sikora et al., 2001). However, with the minimum 3-hour binning a significant sub-structure of a flare becomes prominent, consisting of several apparently chaotic and unresolved yet still large-amplitude events, often characterized by the flux doubling timescales < 3 hours. This clearly illustrates the fact that with the limited time resolution, the apparent profiles of high-energy outbursts in blazar sources may not reflect the exact temporal characteristics of the source flux changes.

Finally, the lower left panel in Figure 5.6 presents the light curves of PKS 1510−089 around the time of the third major gamma-ray outburst, binned again in the intervals of 12 hours, 6 hours, and 3 hours. As shown, the flare seems to be nicely resolved in short binning, displaying a moderately asymmetric profile with a faster flux increase (doubling timescale between 3 hours and 6 hours), and a longer flux decay (e-folding timescale of about 11 h). However, we cannot exclude a possibility that with even shorter binning of the light curve, this smooth and seemingly coherent flaring event would be decomposed into a series of rapid overlapping but not necessarily related sub-events.

5.3.2 Energetics

From the observed *daily-averaged* gamma-ray flux of $\sim 15 \times 10^{-6}\,\mathrm{ph\,cm^{-2}\,s^{-1}}$ in the first flare (shown in Table 5.2), it turned out that most of kinetic energy of the jet was emitted as GeV gamma-rays. The isotropic *daily-averaged* HE luminosity of the first flare analyzed here is $L_{\gamma,\,\mathrm{iso}} \simeq 7 \times 10^{48}\,\mathrm{erg\,s^{-1}}$. The corresponding total power emitted in gamma-rays (i.e., the power as would be measured by the detector completely surrounding the emitting region; e.g., Sikora et al., 1997) is therefore $L_{\gamma,\,\mathrm{em}} \simeq L_{\gamma,\,\mathrm{iso}}/4\Gamma_{\mathrm{j}}^2 \simeq 5 \times 10^{45}\,\mathrm{erg\,s^{-1}}$ (assuming $\Gamma_{\mathrm{j}} \simeq 20$), which is almost exactly the same as the total kinetic power of the PKS 1510−089 jet emerging from broad-band modeling based on different datasets and

model assumptions, $L_{\rm j} \gtrsim 5 \times 10^{45}\,{\rm erg\,s^{-1}}$, and also as the observed UV disk luminosity in the system, $L_{\rm disc} \simeq 5 \times 10^{45}\,{\rm erg\,s^{-1}}$ (Kataoka et al., 2008; D'Ammando et al., 2009; Abdo et al., 2010c). This implies that, during the discussed flaring event, the power dissipated in the jet within less than a day and emitted as gamma-ray photons constitutes the bulk of the total kinetic luminosity carried out by the outflow, $L_{\gamma,\,{\rm em}}/L_{\rm j} \lesssim 1$, and also a substantial fraction of the entire available accretion power, $L_{\gamma,\,{\rm em}}/L_{\rm acc} \simeq 0.1$ (assuming the standard $\eta_{\rm disk} \simeq 10\%$ radiative efficiency for the accretion disk, $L_{\rm acc} \simeq L_{\rm disc}/\eta_{\rm disk} \simeq 5 \times 10^{46}\,{\rm erg\,s^{-1}}$). Note in this context that, for the black hole mass in the system $\mathcal{M}_{\rm BH} \simeq 5 \times 10^{8} M_{\odot}$ (Abdo et al., 2010c), the active nucleus in PKS 1510−089 accretes at the maximum Eddington rate, $L_{\rm acc} \sim L_{\rm Edd}$. A very similar set of the source parameters, implying the extremely efficient conversion of the accretion power to the jet gamma-ray luminosity has been established before by Tanaka et al. (2011) for the analogous blazar PKS 1222+216 observed with LAT during its flaring state.

5.3.3 Emitting Region

We briefly discuss how such a rapid variability constrains the blazar emission zone in a conventional framework, though we would perform more dedicated modeling in chapter 7. This argument is based on the emerging timescales and the related (via the causality arguments) emission zone spatial scales. In particular, the observed flux doubling timescale of $\tau_{\rm d} \simeq 1\,{\rm h}$ and the bulk Lorentz factor $\Gamma_{\rm j} \simeq 20$ (equal by assumption to the jet Doppler factor, consistently with the expected jet inclination $\theta_{\rm j} \simeq 3^{\circ}$) give the spatial scale of the emitting region $R_{\rm var} \leq c\tau_{\rm d}\Gamma_{\rm j}/(1+z) \simeq 1.5 \times 10^{15}\,{\rm cm}$. Meanwhile, the gravitational radius of the PKS 1510−089 supermassive black hole is $r_{\rm g} = G\mathcal{M}_{\rm BH}/c^2 \simeq 7 \times 10^{13}\,{\rm cm}$. Assuming a very basic scenario in which the scale of the event horizon sets a lower limit on the spatial scale of the jet disturbances that can be identified with the zones of the enhanced energy dissipation, one should expect such structures, when created near the black hole, to be advected along the outflow and to release the bulk of their power around $r_{\rm em} \simeq \Gamma_{\rm j}^2 r_{\rm g} \simeq 3 \times 10^{16}\,{\rm cm}$ distances from the core (Begelman et al., 2008). The characteristic radial scale of the outflow at that point is then expected to be approximately $R_{\rm j} \simeq r_{\rm em}/\Gamma_{\rm j} \simeq 1.5 \times 10^{15}\,{\rm cm}$, following the standard expectation for the jet opening angle $\simeq 1/\Gamma_{\rm j}$. The agreement between the derived values of $R_{\rm var}$ and $R_{\rm j}$ is striking.

This identified blazar zone would be located inside the region of the highest ionization of the broad line-emitting circumnuclear clouds ('broad line region'; BLR), for which the characteristic scale in the discussed system is $r_{\rm BLR} \simeq 2 \times 10^{17}\,{\rm cm}$ (Abdo et al., 2010c;

Nalewajko et al., 2012). There the energy density provided by the line-emitting clouds should exceed energy densities of the other photon fields in the jet rest frame, and hence the dominant production of the gamma-ray photons should be related to the IC upscattering of the UV emission (observed energies $\varepsilon_0 \simeq 10\,\mathrm{eV}$) reprocessed with the $\xi_{\rm BLR} = 10\%$ efficiency within the BLR (e.g., Ghisellini & Tavecchio, 2009; Sikora et al., 2009). The corresponding cooling timescale for the electrons emitting gamma-rays with the energies of $\varepsilon_\gamma = 100\,\mathrm{MeV}$, as measured in the observer frame, would then be $\tau_{\rm rad} \simeq (3m_e c/4\sigma_T u'_{\rm BLR}) \times [\varepsilon_0(1+z)/\varepsilon_\gamma]^{1/2} \gtrsim 10\,\mathrm{min}$, for the jet comoving BLR photon energy density $u'_{\rm BLR} \simeq \xi_{\rm BLR}\, L_{\rm disk}\Gamma_{\rm j}^2/4\pi r_{\rm BLR}^2 c \simeq 10\,\mathrm{erg\,cm^{-3}}$. This timescale is shorter by a factor of $10-50$ than the observed e-folding decay timescales of the flares, implying that the observed flux decrease is shaped not solely by the radiative energy losses, but instead by a combination of different factors. These other factors may be related either to the geometry and sub-structure of the emitting region (e.g., Tanihata et al., 2001), or to a residual particle acceleration still ongoing after the peak of a flare.

The 'near-dissipation zone' scenario, with the dominant emission region located relatively close to the central engine ($\lesssim 0.1\,\mathrm{pc}$), was advocated in the literature for FSRQs in general based on the modeling of their HE gamma-ray spectra (Poutanen & Stern, 2010). The complication arises, however, due to the aforementioned detection of a few FSRQs, including PKS 1510−089 and PKS 1222+216, at TeV photon energies (see Tanaka et al., 2011; Tavecchio et al., 2011). The emerging agreement is that such VHE emission, if detected, must be produced instead at further distances from the core, i.e. beyond the characteristic scale of the circumnuclear dust ($> 0.1\,\mathrm{pc}$).

Table 5.2: Major gamma-ray flares of PKS 1510−089.

MJD	$F_{>100\,\mathrm{MeV}}$	Γ_γ
(1)	(2)	(3)
55853.5–55854.5	14.86 ± 0.89	1.97 ± 0.04
55867-55869	10.95 ± 0.57	2.21 ± 0.04
55872–55874	8.39 ± 0.44	2.19 ± 0.04

(1) Dates of the three major gamma-ray flux maxima in the daily-binned light curve of PKS 1510−089; (2) photon fluxes measured at the flux maxima in the units of $[10^{-6}\,\mathrm{ph\,cm^{-2}\,s^{-1}}]$, averaged over the specified time intervals; (3) the corresponding photon indices.

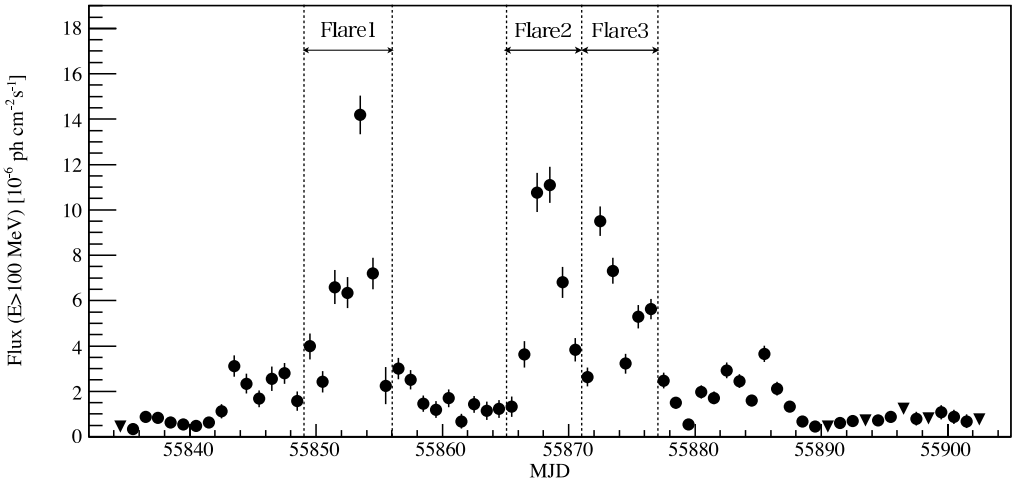

Figure 5.5: Daily γ-ray light curve of PKS 1510−089 during the period MJD 55834–55903 analyzed in this paper. 95% flux upper limits are represented by triangles. Horizontal lines separating the three major flares are chosen arbitrarily just to guide the eye.

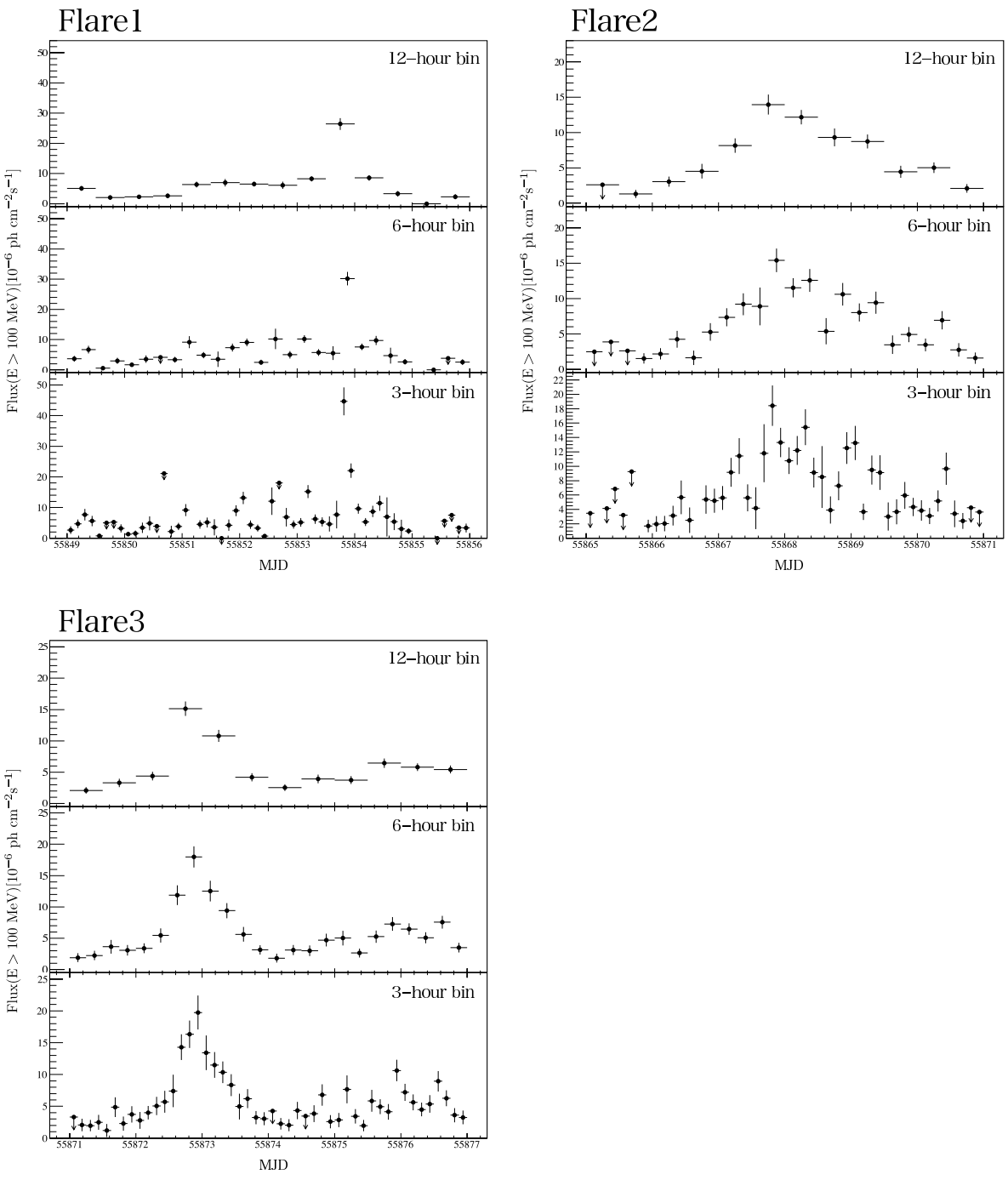

Figure 5.6: *Fermi*-LAT light curves of PKS 1510−089 around the three major γ-ray outburst, binned in the intervals of 12 h, 6 h, and 3 h (upper, middle, and lower panels, respectively).

Chapter 6

New Approach for Finding Shorter Variability

The discovery that apparently coherent single flare could be resolved into superpositions of sub-structures in shorter time binning poses further question, namely what the shortest variability time scale of GeV blazar flares is. We found the shortest GeV variability time scale of $\sim$1 hour in PKS 1510–089, but there might be even shorter high-amplitude variability which would be masked in 3-hour binned light curves.

Photon statistics principally limits further investigation with better time resolution even for the collected samples of the brightest blazar flares. Another thing is that we couldn't obtain continuous data of our target sources due to exposure gaps caused by all-sky survey operation of *Fermi*-LAT. As *Fermi* goes around the earth in 90 minutes and surveys all sky in 3 hours in its nominal operation, we have sources in LAT's FOV typically for < 30 minutes in each orbit. As a result, we have only 10+ photons for each exposure window even in the very bright flaring states. For reducing variability characteristics from such limited photon statistics, in this chapter, we adopted Bayesian approach to search for sub-hour variability.

6.1 Introduction to *Bayesian Block* Method

We introduced *Bayesian block* method which divides time series data into sections represented by piecewise constant model. This method is developed in Scargle (1998) and Scargle et al. (2013). We applied *Bayesian blocks* algorithm to 10 brightest flaring periods of blazars for searching for sub-orbit time scale variability.

6.1.1 *Bayesian Block* Method

Definition of Event Cells

At first, we define event cells for a series of time-tagged events. If we know arrival time for each photon with sufficient timing accuracy, which is the case with *Fermi*-LAT, the event cell could be defined as,

$$\left(\frac{t_n + t_{n-1}}{2},\ \frac{t_{n+1} + t_n}{2}\right) \tag{6.1}$$

where t_k is the arrival time of k th photon. In this representation, every event cell contains single photon as is shown in Figure 6.1.

Unbinned Likelihood Function

Bayesian block utilizes unbinned likelihood function. Fitness function is calculated as follows (Tompkins (1999)). Assume M($\mathbf{x}$) as the number of model prediction counts at given position, energy, and time represented by $\mathbf{x}$. If we construct bins of size $|\mathrm{d}\mathbf{x}|$, where each bin is sufficiently small, the probability of finding more than two photons in the bin could be ignored. Considering the Poisson distribution, the probability of finding a photon in the bin; P_1 and that of finding no photons; P_0 could be calculated:

$$P(X = k) = \frac{\lambda^k e^{-\lambda}}{k!} \tag{6.2}$$

$$P_1(\mathbf{x}) = P(X = 1) = M(\mathbf{x})\mathrm{d}\mathbf{x}e^{-M(\mathbf{x})\mathrm{d}\mathbf{x}} \tag{6.3}$$

$$P_0(\mathbf{x}) = P(X = 0) = e^{-M(\mathbf{x})\mathrm{d}\mathbf{x}} \tag{6.4}$$

If we write the set of bins with a photon as A, and the set with no photons as B, the likelihood function for entire data set is,

$$\begin{aligned} L &= \prod_{i\in A} P_1(\mathbf{x}_i)\mathrm{d}\mathbf{x}_i \times \prod_{i\in B} P_0(\mathbf{x}_i)\mathrm{d}\mathbf{x}_i \\ &= \prod_{i\in A} M(\mathbf{x}_i)e^{-M(\mathbf{x}_i)}\mathrm{d}\mathbf{x}_i \times \prod_{i\in B} e^{-M(\mathbf{x}_i)\mathrm{d}\mathbf{x}_i} \\ &= \prod_{i\in A} M(\mathbf{x}_i)\mathrm{d}\mathbf{x}_i \times \prod_{i\in A,B} e^{-M(\mathbf{x}_i)\mathrm{d}\mathbf{x}_i} \end{aligned} \tag{6.5}$$

$$\begin{aligned} \log L &= \sum_{i\in A} \log M(\mathbf{x}_i) + \sum_{i\in A} \log \mathrm{d}\mathbf{x}_i - \sum_{i\in A,B} M(\mathbf{x}_i)\mathrm{d}\mathbf{x}_i \\ &= \sum_{i\in A} \log M(\mathbf{x}_i) + N\log(\mathrm{d}\mathbf{x}) - \int M(\mathbf{x})\mathrm{d}\mathbf{x} \end{aligned} \tag{6.6}$$

Since the second term in the above equation is independent of the model parameters, it could be eliminated when calculate likelihood ratio or look for the maximum likelihood model. Thus the likelihood fitness function is written as,

$$\log L = \sum_{i \in A} \log M(\mathbf{x}_i) - \int M(\mathbf{x}) \mathrm{d}\mathbf{x} \tag{6.7}$$

Block Fitness Function

Consider a set of time-tagged events, which contains N_k events(photons) within a time interval of T_k. If we represent the set of events with constant model, the likelihood function in Eq.(6.7) could be written as follows by using constant model parameter $M(\mathbf{x}) = \lambda_k$.

$$\log L_k = N_k \log \lambda_k - \lambda_k T_k \tag{6.8}$$

By solving $\mathrm{d}(\log L_k)/\mathrm{d}\lambda_k = 0$, the likelihood function is derived to be maximized at $\lambda_k = N_k/T_k$. Then the maximum likelihood function is written as,

$$\log L_{k,\max} = N_k(\log N_k - \log T_k) - N_k \tag{6.9}$$

Since the last term in the right hand side does not affect calculations of likelihood ratio, it could be ignored. Finally, we obtain the maximum likelihood function for a single data set characterised by (N_k, T_k) as follows.

$$\log L_{k,\max} = N_k(\log N_k - \log T_k) \tag{6.10}$$

Constructing Piecewise Constant Model

Bayesian block method constructs optimum piecewise constant representation of event data, by maximizing the sum of likelihood fitness functions among all the combinations of event cells. That means it explores 2^{N} possibilities by combining/decombining junctions of all the event cells, where N is the total number of events. The amount of calculation could be reduced to N^2 by utilizing dynamic programming (See Jackson et al. (2005) for further detail).

Simply maximizing the sum of the likelihood function; Eq.(6.10) gives the piecewise constant representation which is resolved into N event cells. This could be confirmed by following calculations. Consider the likelihood functions of the first event cell and the second event cell, which are written as

$$\log L_{i,\max} = 1(\log 1 - \log T_i) = -\log T_i, \qquad i = 1, 2 \tag{6.11}$$

Thus the sum of the likelihood function for the 2 blocks is written as,

$$\log L_{\max} = \log L_{1,\max} L_{2,\max} = -\log T_1 - \log T_2 = -\log T_1 T_2 \tag{6.12}$$

On the other hand, if we consider the combined block of the 2 event cells, the likelihood function is written as,

$$\log L'_{\max} = 2(\log 2 - \log(T_1 + T_2)) \tag{6.13}$$

Then the ratio of these two likelihood functions is,

$$\begin{aligned} \log\left(\frac{L_{\max}}{L'_{\max}}\right) &= \log L_{\max} - \log L'_{\max} \\ &= -\log T_1 T_2 - 2(\log 2 - \log(T_1 + T_2)) \\ &= \log \frac{((T_1 + T_2)/2)^2}{T_1 T_2} \\ &\geq 0 \end{aligned} \tag{6.14}$$

Since $L_{\max} \geq L'_{\max}$ is always true, 2 block representation is always favored over the combined representation. Thus the simple maximum likelihood method will inevitably results in N-block representation consisting of N individual event cells, which is rather meaningless representation.

For suppressing the excessive fitting to the data of maximum likelihood procedure, we introduced prior probability in the framework of Bayesian statistics. The likelihood function would be biased with prior probability; ψ^{N_B}, where $0 < \psi \leq 1$ and N_B is the number of blocks.This prior distribution was chosen to set the probability for representations with many blocks lower. Then the alternative function which should be maximized could be written as,

$$L = \prod_{k \in B} L_{k,\max} \times \psi^{N_B} \tag{6.15}$$

$$\begin{aligned} \log L &= \sum_{k \in B} \log L_{k,\max} + N_B \log \psi \\ &= \sum_{k \in B} N_k (\log N_k - \log T_k) + N_B \log \psi \end{aligned} \tag{6.16}$$

where B is the set of blocks and N_B is the total number of blocks.

How the prior parameter ψ affects the data representation would be confirmed and calibrated via numerical simulations in the following part of this chapter. Then we tried to obtain the best representation of the LAT data by maximizing the function; Eq.(6.16).

6.1.2 Calibration of *Bayesian Block*

In this section, we characterized effect of the prior parameter ψ on the resulting representations. We could choose ψ within $0 < \psi \leq 1$ in order to avoid the excessive fitting to data, and suppress the resulting number of blocks of the *Bayesian Block*.

For quantifying the relation of ψ and resulting block representations in comprehensive way, "false positive probability"; fp is introduced here. fp is the probability that the *Bayesian Block* falsely find change points in uniformly random data. In other words, it is the probability that the algorithm results in more than two blocks for data with merely random series of events. Then $1 - fp$ means the probability algorithm correctly rejects the presence of change points for random events. If we know $fp - \psi$ relation, we could simply choose convenient fp value in running the algorithm.

The $fp - \psi$ relation could be estimated by applying the algorithm to random series of events for many times, which would be done in the next step. fp only depends on ψ and the number of events (N), thus we could write $\psi = \psi(N,\, fp)$ (Scargle et al. (2013)).

Definition of Event Cells

The definition of event cells at the first and the last event is not obvious, and it would significantly affect the $fp-\psi$ relation. In Scargle et al. (2013) event cells are defined like the upper panel in Figure 6.1, namely the edges of the first and the last cells correspond to the arrival times of the first and the last event. However, if considering the case of actual observation, information of exposure beyond the edges of the first and last event cells would be lost in this definition.

For making full of the exposure information provided by the LAT, we applied new definition of event cells by which the edges of the first and the last cells correspond to the time of observation starts and stops (see the lower panel in Figure 6.1). We performed simulations for estimating $fp-\psi$ relation based on this definition of event cells. Definition of event cells except for the first and the last event was following Eq.(6.1).

Numerical Simulations to Obtain $fp - \psi$ Relation

We performed numerical simulations for estimating $fp-\psi$ relation by producing random series of events for various sets of the number of events (N). For given N and ψ, we estimated fp by following procedures.

1. Make random series of events, where the number of events is N.

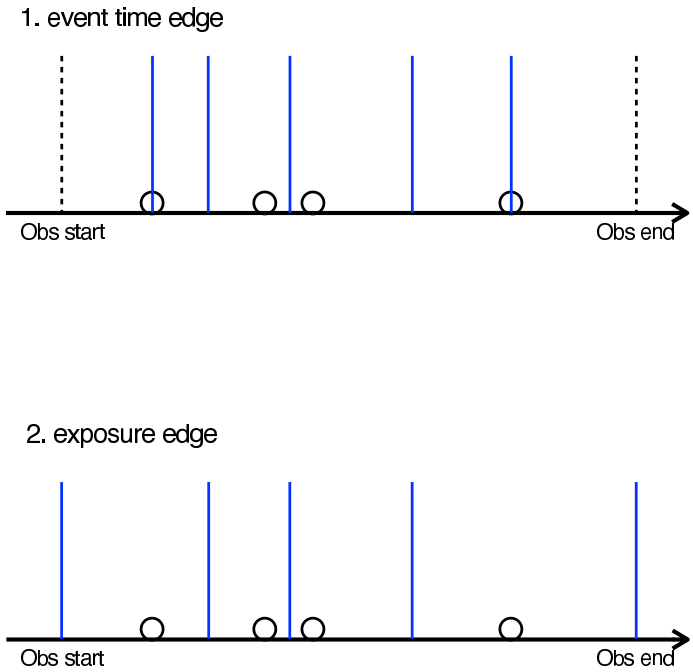

Figure 6.1: Event cell definitions for the *Bayesianblock* analysis. Open circles represent arrival times of photons, and blue vertical lines represent edges of event cells. Difference of two types of definition is whether the first and the last event cells include all the exposure toward the start and end of the observation. We use definition of (2) for the analysis in this thesis.

2. Find block representation which maximizes the likelihood value of Eq.(6.16). (This is the application of the *Bayesian Block*.)

3. Repeat 1. and 2. for 100,000 times.

4. Estimate fp. Assuming the number of trials which result in more than two block representation as n, fp could be calculated as $n/100,000$.

We performed the above simulations for every N within $2 \leq N \leq 200$, and $-\log\psi$ within $0 \leq -\log\psi \leq 9.0$ in every 0.1 steps. We note that $-\log\psi$ always takes positive value since $0 < \psi \leq 1$. Figure 6.2 shows the results of simulations for both manners of event cell definitions. There are obvious differences in the $fp - \psi$ relation, especially for small number of events, while as the number of events becomes larger the difference becomes smaller. We also note that the following formula gives good approximation of the relation for the conventional manner of event cell definition, namely for the first and

the last event cells correspond the arrival times of events (Scargle et al. (2013)).

$$-\log\psi = 4 - \log\left(\frac{fp}{0.0136N^{0.478}}\right) \tag{6.17}$$

The dotted lines in the graphs represent this formula, which is marginally consistent with simulation results over various sets of N and $-\log\psi$ for the case of conventional event cells definition (left panel in Figure 6.2), whereas it completely does not work for the definition of event cells used in this thesis (right panel in Figure 6.2). In the following analysis, we treat the relation of fp and $-\log\psi$ based on the simulated table, not on the Eq. (6.17).

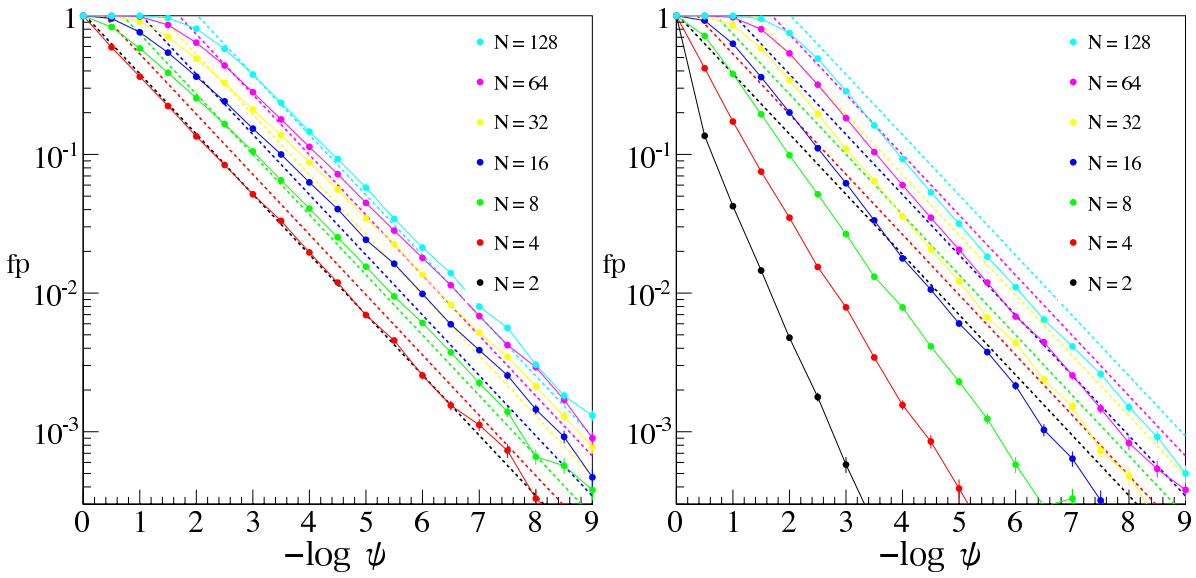

Figure 6.2: Relation between $-\log\psi$ and fraction of false positive detection (fp) obtained from simulations of random event series by varying the parameter of prior distribution ψ for different number of events. We simulated 100,000 times for each point in the plots. Dotted line in both panels represents Eq. (6.17). *(left)* Event cell definition of (1) in Figure 6.1 is utilized. *(right)* Event cell definition of (2) in Figure 6.1 is utilized. Though we simulated all the number of events under 200 and $-\log\psi$ in every 0.1 steps, only a part of them are presented in these figures.

6.2 Analysis Setup for *Fermi*-LAT Data

6.2.1 Optimization of Region of Interest

Region of interest (ROI) should be chosen carefully since the Bayesian analysis discussed in this chapter takes arrival time of all the photons in the ROI into account. We lose significant number of photons due to moderate point spread function (PSF) of *Fermi*-LAT (see Figure 3.4) when small ROI is chosen, while the ROI is contaminated with background photons or photons from nearby sources when large ROI is chosen. Therefore, ROI should be optimized for maximizing the source significance we are intended to analyse. Optimum ROI would be affected by complex effects of energy band, brightness and spectral shape of nearby sources or the Galactic/Extragalactic background, and flux of the target source.

We derived optimum ROI for the selected brightest flares based on estimation of the source and background photons. The number of photons from each source and diffuse emission in the source model file is predicted via the likelihood analysis performed in the previous chapter. Assuming radius of the ROI as θ, the predicted number of photons from the target source as $N_S(\theta)$, and the predicted number of photons from the Galactic/Extragalactic emission and the other sources nearby the target source (including stray photons from outside the ROI) as $N_B(\theta)$, the total number of photons in the ROI could be written as,

$$N(\theta) = N_S(\theta) + N_B(\theta) \tag{6.18}$$

Figure 6.3 shows how $N_S(\theta)$ and $N_B(\theta)$ depend on ROI selection. Full interval of #6 flare in 4C 21.35 is analysed in this case. The ROIs were changed from 1° to 10° by 1° step, with all the ROIs were centered on the source position of 4C 21.35. At first, we compute likelihood analysis for 10° ROI radius with flux and photon index of 4C 21.35 are set free in each energy band. Then varying ROI radius from 9° to 1° with flux and photon index fixed at the values obtained by the analysis of 10° ROI radius, while parameters of other sources and diffuse components are fixed at their nominal values referred from 2FGL catalog. This figure clearly shows that the number of signal photons and background photons become comparable for large ROI such as 10° radius. On the other hand, photon statistics of the target source become significantly worse for small ROI radius especially for lower energy bands. Right panel in the figure represents source fraction over total number of photons in the ROI. Components which consist of observed background photons are shown in Figure 6.4. Extragalactic isotropic background and

the Galactic diffuse background are the major component of total background over all the ROI, while there is a little contribution from point sources near 4C 21.35.

Next, selection of optimum ROI by considering the balance of the number of signal and background photons is described below. We defined the significance S as a ratio of the signal counts to the total counts;

$$S(\theta) = \frac{N_S(\theta)}{\sqrt{N(\theta)}} \tag{6.19}$$

ROI dependence of $S(\theta)$ is shown in Figure 6.5. The ROIs which give maximum source significance are 5°, 4°, and 3° for energy bands of 0.1 - 1 GeV, 0.3 - 1 GeV, and 1 - 300 GeV. There are background contamination of 15%, 7% and 3% for these energy bands, thus systematic increase of source flux by 18%, 11% and 3% would be expected in average mainly due to isotropic extragalactic background when analysed by the aperture photometry analysis.

The optimum ROI radius and background contamination for the selected brightest blazar flares are summarized in Table 6.1. Extragalactic and Galactic diffuse components are major origin of background photons in the ROI through all the flares. We note these dominant diffuse components are not considered to vary in short time scale as studied in this work. In the following Bayesian analysis, we performed the analysis in two energy range, which are 0.3 - 1 GeV and 1 - 300 GeV. From Figure 6.5 we know that ROI radius of 3 degree offers marginally optimum ROI for both energy ranges. We fixed ROI for the event selection at 3 degree in the following analysis.

6.2.2 Treatment of Exposure Variation

As the *Fermi*-LAT surveys all sky with its field of view of 2.4 sr, and covering the entire sky in 3 hours in its survey mode, exposure toward any point in the sky varies with time. Typically arbitrary point in the sky would be included in LAT FOV for $\sim$ 30 minutes in every three hours (we defined this duration as "exposure window" hereafter).

Exposure of the *Fermi*-LAT could be calculated in the minimum time scale of 30 seconds, which corresponds to a cycle that attitude information of the LAT is recorded to the spacecraft data file. Figure 6.6 shows exposure variation during the brightest flare in PKS 1510-089. A region with 5° radius around PKS 1510-089 was chosen for calculating the exposure, using `gtexposure` function in the LAT science tool. In order to provide reasonably accurate flux estimates for broad energy bands, the exposure must be weighted by a function that approximates the spectral shape of the target source. Here we ran `gtexposure` assuming a photon spectral index of 2.

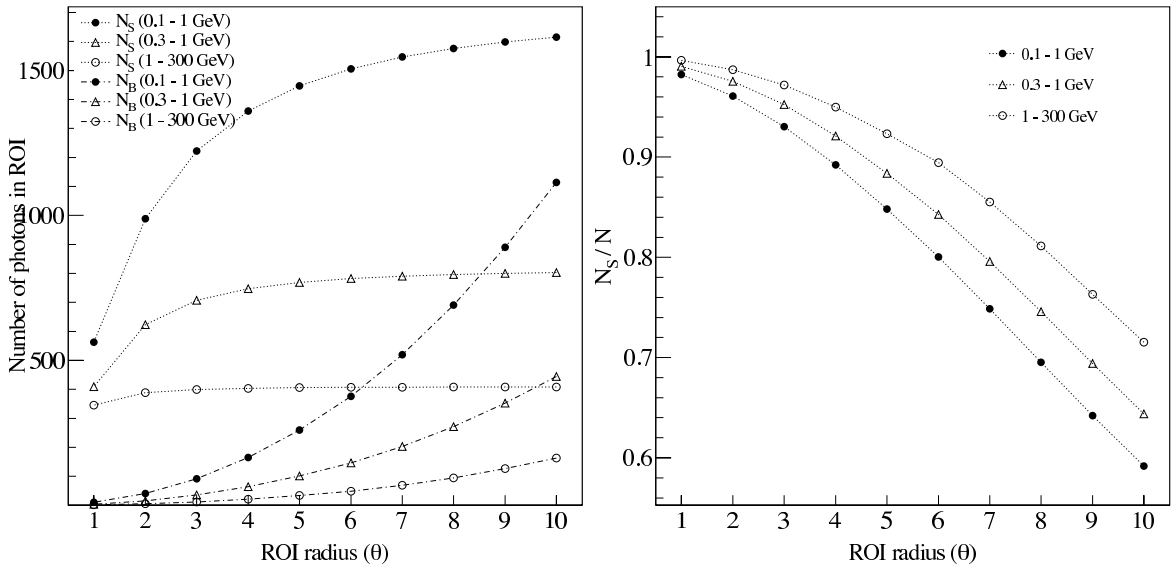

Figure 6.3: (*left*) ROI dependence of the number of signal photons (N_S) and background photons (N_B) in the ROI. (*right*) ROI dependence of the fraction of the number of signal photons relative to the total number of photons in the ROI.

6.2.3 Aperture Photometry Analysis

Since the optimum ROI chosen for the *Bayesian block* analysis is rather small compared to the LAT PSF, source modeling in standard likelihood analysis could not be performed in such small ROI. Thus flux estimation in this chapter is based on aperture photometry analysis instead of a standard likelihood analysis which was discussed in chapter 5. In the aperture photometry analysis, photon flux is calculated by dividing the number of photons by the exposure ($\mathrm{cm}^2\,\mathrm{s}$) in the ROI (Region of Interest). Compared to the likelihood analysis, the aperture photometry analysis calculates photon flux in less model independent way, and enables the use of short time bins whereas likelihood analysis requires that time bins contain sufficient photons for analysis.

For clarifying how aperture photometry works, comparison of aperture photometry and likelihood analysis for 4C 21.35 bright flare is presented in Figure 6.7, where ROI for the aperture photometry was set to 3 degree. Those two methods give very similar fluxes over 1 GeV, though there are more than 20% discrepancy due to background photons under 1 GeV. Above 1 GeV, both calculations almost coincides, which means background photons are negligible compared to source photons.

6.3 Application of *Bayesian block* to the Observed Gamma-ray Flares

6.3.1 Verification of *Bayesian Block* Method Using the 5-year LAT Data

At first, we confirmed how *Bayesian Block* works in characterizing flux variability based on 62-month data of the four selected brightest blazars. 62-month LAT data of the brightest blazars were analysed in 0.3–1 GeV and 1–300 GeV bands to check if there were high-amplitude sub-daily flux changes or variability only in the high energy band which would be missed in the standard daily-binned analysis presented in chapter 4. Figure 6.8 shows 62-month light curves with *Bayesian block* analysis. ROI was set to 3° and false positive probability; $fp = 0.01$ for both energy bands. Compared with the daily-binned light curves produced by standard likelihood method presented in Figure 4.6, variability trends seen in Figure 4.6 were also depicted in the light curves by the *Bayesian block* method. Both very short (sub-daily) spiky structure of flaring profiles which appeared in PKS 1510–089 at MJD 55850 and 3C 273 at 55200 as well as relatively long lasting brightening observed around MJD 55200 in PKS 1510–089 are successfully identified by this method. Moreover, all the selected brightest flares based on daily-binned light curves are confirmed as indeed brightest ones, and the selected intervals are well defined. On the other hand, selection based on the daily binned light curves underestimated amplitudes of flares occurred in very short time scale, as shown in 3C 273 at 55200 for example. We also note that no obvious flarings above 1 GeV were detected with no accompanying low-energy flux change.

6.3.2 Results of Systematic Analysis

We tried to investigate if there is significant variability within the single exposure window (∼30 minutes) under the all sky survey mode of LAT. *Bayesian block* is introduced to search the variability under very limited photon statistics. We applied *Bayesian block* method to the LAT data of the top ten brightest blazar flares presented in Table 4.1, based on the modified false positive probability(fp) relation discussed in the previous section. In collecting photons from the target sources, we chose circular ROIs with radius 3°, centered at the radio positions of the target based on the optimization of ROI. Variability was investigated in two energy bands of 300 MeV – 1 GeV, and 1 – 300 GeV, by varying fp value. More than 70% and 95% of source photons are included in this

ROI above 300 MeV and 1 GeV, and fraction of photons from other sources are less than 10% of the number of photons from the targets at very bright flaring states.

Event cells were defined based on Eq.(6.1) which utilizes arrival times of photons in ROI. For each event cell, the width of the cell was weighted with LAT exposure at the moment. The time profile of exposure (= effective area × observed time) towards the targets is calculated by `gtexposure`. Photon index of 2.0 is assumed when running `gtexposure` for modifying an effect of tails of PSF exceeding ROI for calculating flux.

The analysis results of 3C 454.3, PKS 1510–089, 4C 21.35, and 3C 273 are presented in Figure 6.10, Figure 6.11, Figure 6.12, and Figure 6.13, respectively. *Bayesian block* analysis were performed with $-\log\psi$ value which corresponds to fp value of 0.1. Light curves presented in left panels were created by calculating flux via aperture photometry. Every orbit which has at least 3 photons was analyzed.

Each LAT exposure window during the flares were separately analysed with *Bayesian blocks* in order to investigate sub-orbit variability, which corresponds to sub-hour variability. Examples of outputs from *Bayesian block* analysis applied to single orbit are presented in Figure 6.9. In these cases, *Bayesian block* analysis found one flux change point in the series of data, and resulted in two block representations. However, we could not conclude that sub-orbit variability was confirmed from these results, since there is possibility that the two block representation could be resulted from false positive detection. Thus we applied *Bayesian block* to all the exposure windows during the flares to evaluate significance of positive detection.

In order to evaluate significance of sub-orbit variability, fraction of orbits which are detected as variable was estimated for different fp values from 0.1 to 0.9 in 0.1 steps. The results of detected fraction is presented in right panel in Figure 6.10, Figure 6.11, Figure 6.12, and Figure 6.13. We defined orbits where *Bayesian block* analysis resulted in more than two block representation as positively detected orbits. Here we assumed the number of positively detected orbits follows binomial distribution of $\mathrm{B(n, fp)}$, where n is the total number of orbits (exposure windows) during a flare. Then the error of the number of positively detected orbits were calculated as $\sqrt{n \times fp(1-fp)}$. According to the analysis of the flares, the number of orbits which were detected as variable are consistent with the number expected for false positive detection for uniform and random events for nine of the ten selected flares.

On the other hand, there were deviations from the fp – detected fraction profile expected for uniform random events for flare #5 in PKS 1510–089. The positively detected fraction was 0.8 when fp was set to 0.5, which showed most prominent deviation from fp value. Probability that events subject to constant flux accidentally give such

a deviation could be calculated. Since the positively detected fraction (p) for uniform random events subjects to binomial distribution, the chance probability that the uniform events give $p > 0.8$ is 1.6×10^{-4}, which corresponds to 3.5σ deviation in the context of Gaussian distribution.

6.3.3 Evaluation of Variability via Simulations

From the application of *Bayesian block* to the selected sample of flares, flare #5 in PKS 1510–089 showed some indications for sub-orbit variability. The positively detected fractions in #5 flare were beyond solid line, which corresponds to the expected profile for random events, for all the fp values.

Properties of number of photons per orbit and exposure time were shown in Figure 6.14. Orbits which have more than 3 photons were analysed with the Bayesian method here, and mean exposure time for such orbits was 38.5 minutes for 0.3 – 1 GeV and 35.4 minutes for 1 – 300 GeV.

To quantify the variability amplitude expected in sub-orbit timescale during the flare, we performed *Bayesian block* simulations assuming rectangle flux profiles to compare with observation results as is shown in the left panel in Figure 6.15. We chose the variability profile of rectangular shape simply because there is only one parameter which need to characterize the variability.

The procedure of the simulation is,

1. Assume rectangular variability profiles with T/5, T/3, T/2, and T(this means constant flux) which lie in the middle of time window in the LAT exposure.

2. Multiply the variability profile and LAT exposure profile for each orbit to obtain expected count distribution profile when the rectangular variability is observed with LAT.

3. For each orbit, simulate events subject to the distribution obtained in 2.. The number of events simulated is set at the same number as is observed in real data. Orbits which has at least 3 photons were selected for the simulation.

4. Apply *Bayesian block* to the sets of events obtained in 3. by changing fp.

5. Repeat 3. and 4. for 100 times for suppressing statistical errors with simulations.

6. Make "fp - positively detected fraction" profile.

Finally the simulated profiles of fp – detected fraction were compared with the derived profile of #5 flare in PKS 1510–089 in the right panel of Figure 6.15. Comparison with simulation results indicates sub-orbit variability, corresponding to ∼15 minutes variability which is approximately the half-width of the exposure window, with the power of T/2 or T/3 in this flare.

6.3.4 Conclusions

In this chapter, we introduced Bayesian method to investigate sub-hour variability during the flares. According to the analysis of variability during exposure windows lasting for ∼30 minutes, nine of the ten flares showed no sub-hour variability, and only one flare in PKS 1510–089 showed an indication of sub-hour variability. However, the fact that the deviation is 3.5σ at the optimum fp value and the expected power of variability estimated with simulations is rather moderate made us conclude that sub-hour variability in FSRQ is not general.

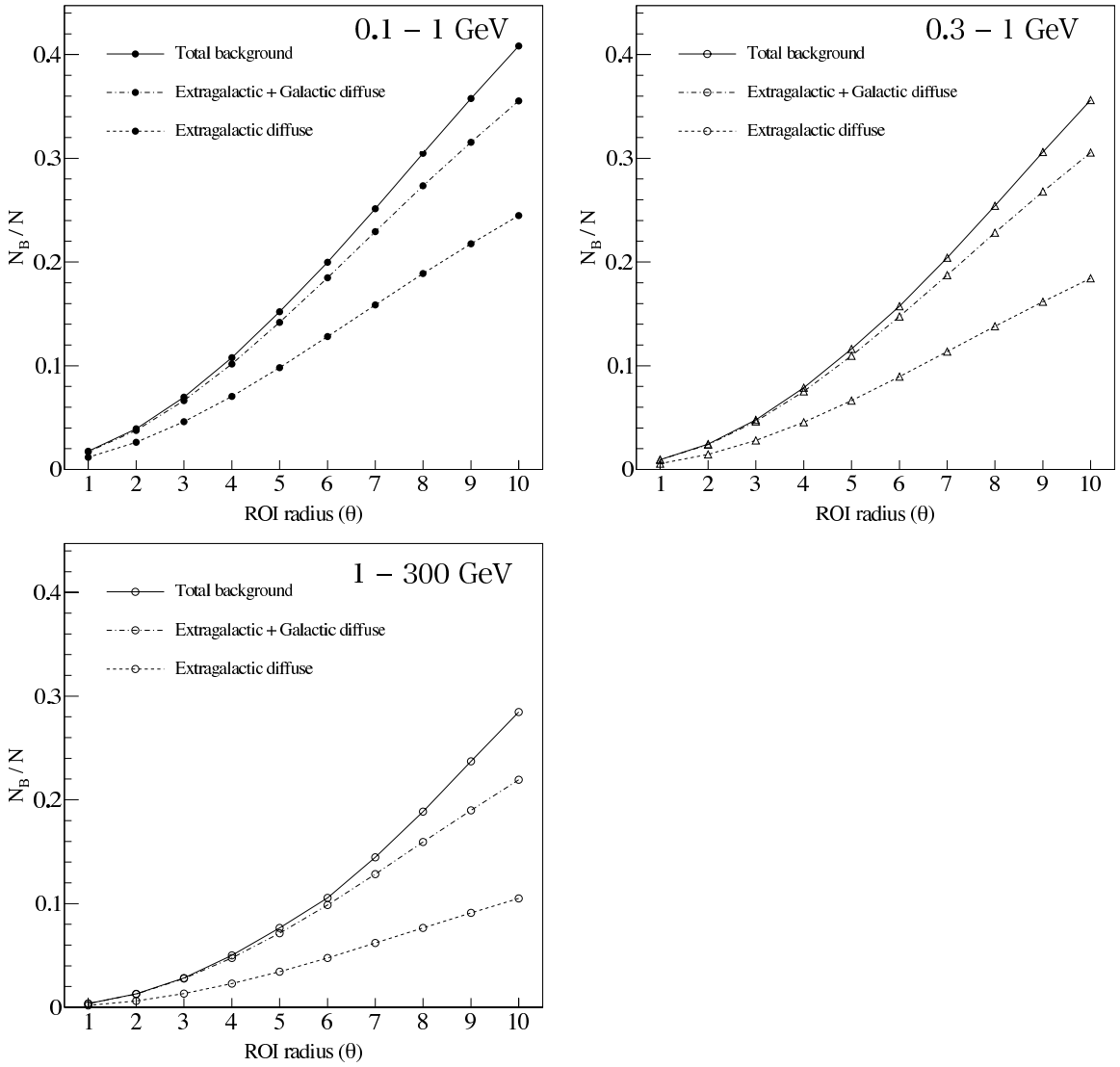

Figure 6.4: ROI dependence of background components to total photons. (*upper left*) 0.1 - 1 GeV, (*upper right*) 0.3 - 1 GeV, (*lower left*) 1 - 300 GeV.

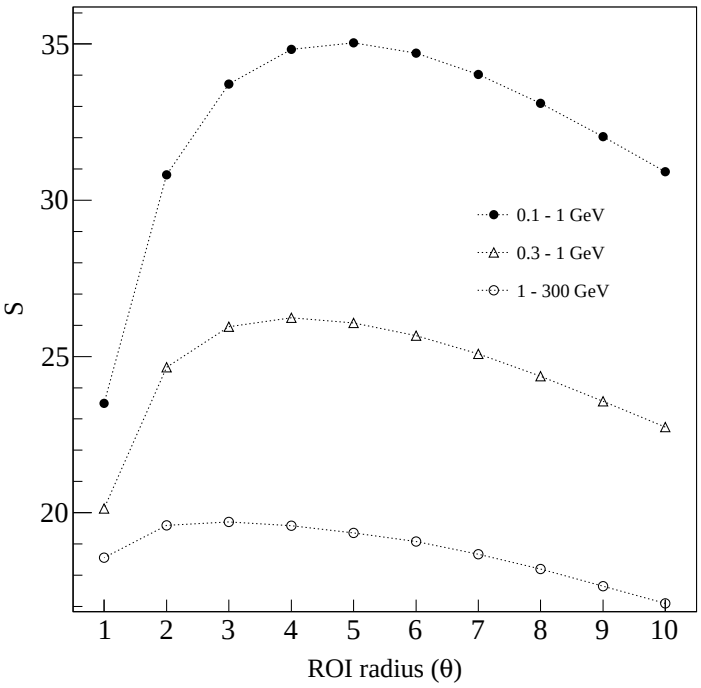

Figure 6.5: ROI dependence of source significance over background for several energy bands.

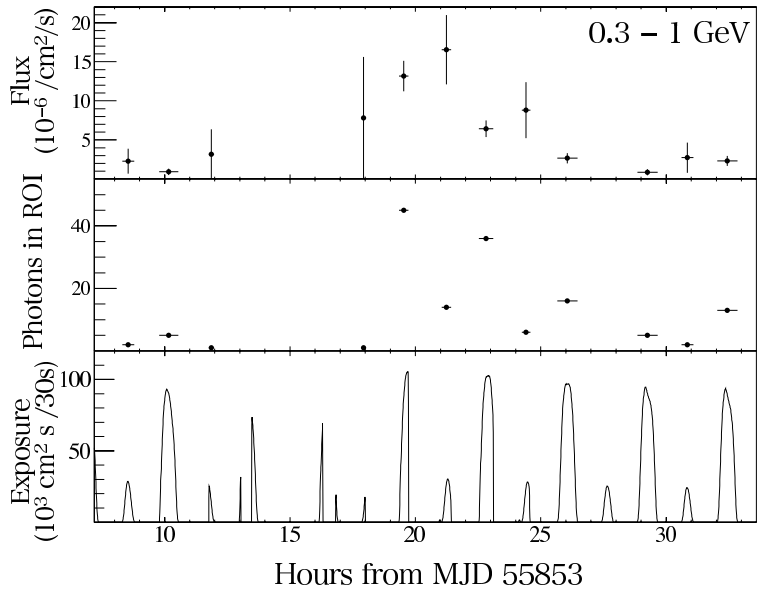

Figure 6.6: Exposure variation toward PKS 1510-089 during flare #5. ROI was set to 3°.

Table 6.1: Optimum ROI radius for the selected blazar flares.

ID	Source	Energy(GeV)	Optimum ROI (°) (Significance)	Background fraction	Galactic + Extragalactic
1	3C 454.3	0.1 - 1	7 (181.2)	0.089	0.08
		0.3 - 1	5 (114.4)	0.051	0.046
		1 - 300	3 (65.0)	0.021	0.019
2	3C 454.3	0.1 - 1	7 (69.9)	0.123	0.112
		0.3 - 1	5 (45.0)	0.073	0.066
		1 - 300	3 (25.5)	0.032	0.029
3	3C 454.3	0.1 - 1	6 (54.6)	0.099	0.089
		0.3 - 1	5 (33.9)	0.074	0.068
		1 - 300	3 (18.9)	0.032	0.029
4	3C 454.3	0.1 - 1	6 (86.3)	0.104	0.094
		0.3 - 1	4 (52.2)	0.056	0.050
		1 - 300	3 (28.2)	0.038	0.034
5	PKS 1510-089	0.1 - 1	5 (24.3)	0.148	0.138
		0.3 - 1	4 (17.4)	0.093	0.087
		1 - 300	3 (12.8)	0.042	0.042
8	PKS 1510-089	0.1 - 1	5 (38.0)	0.189	0.177
		0.3 - 1	4 (26.0)	0.129	0.121
		1 - 300	2 (15.6)	0.041	0.041
12	PKS 1510-089	0.1 - 1	5 (31.7)	0.221	0.206
		0.3 - 1	3 (20.8)	0.101	0.097
		1 - 300	2 (11.0)	0.066	0.065
6	4C 21.35	0.1 - 1	5 (35.0)	0.152	0.142
		0.3 - 1	4 (26.2)	0.079	0.075
		1 - 300	3 (19.7)	0.028	0.028
7	4C 21.35	0.1 - 1	5 (53.3)	0.172	0.161
		0.3 - 1	4 (36.1)	0.101	0.096
		1 - 300	2 (23.4)	0.021	0.021
9	3C 273	0.1 - 1	5 (42.8)	0.207	0.166
		0.3 - 1	3 (26.7)	0.094	0.079
		1 - 300	2 (13.5)	0.053	0.051

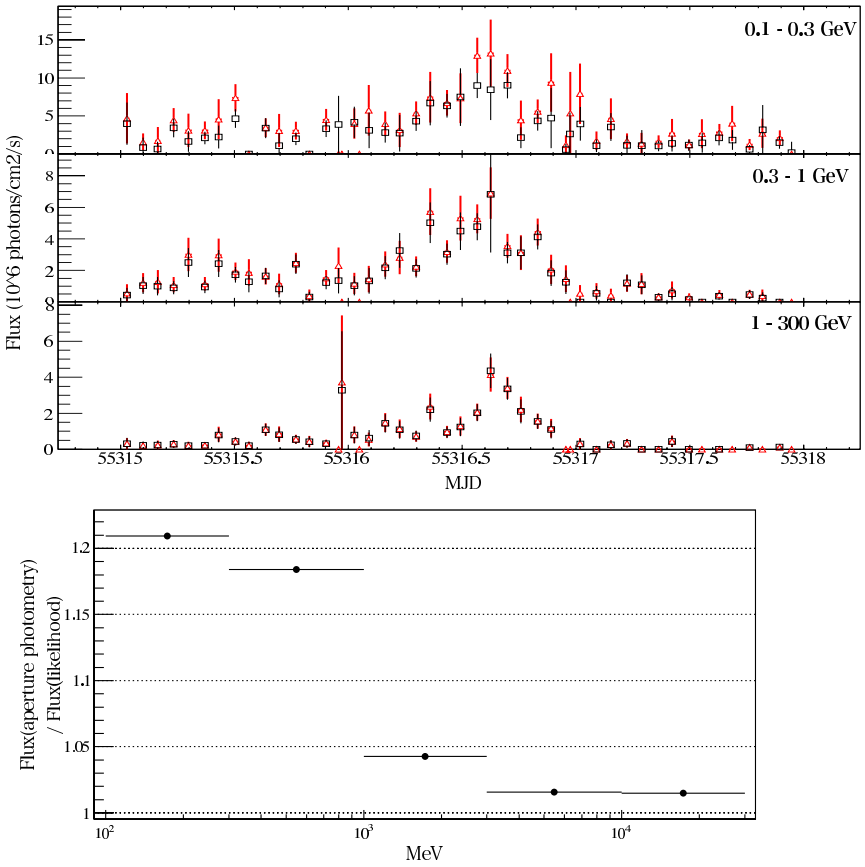

Figure 6.7: Comaprison of aperture photometry and likelihood method for the flare of 4C21.35. *(upper panel)* Comparison in orbit-binned light curve. black point–likelihood, red point–aperture photometry. *(lower panel)* Comparison in different energy bands.

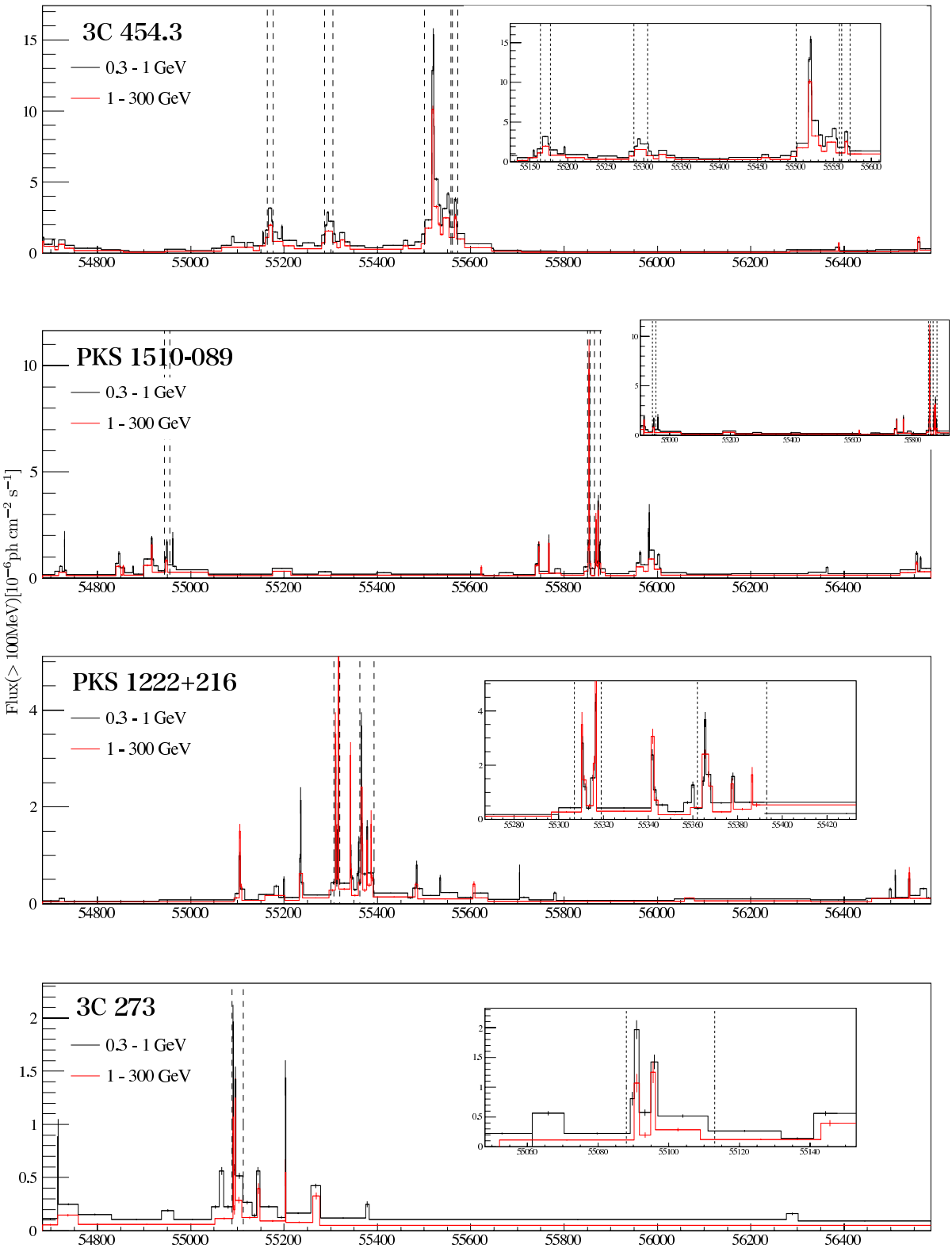

Figure 6.8: 62-month LAT light curves of the brightest blazars analysed by Bayesian block. Flux in 1 - 300 GeV was multiplied by 3. fp=0.01, ROI=3. Vertical dotted lines represent selected intervals by daily-binned analysis. Detail description of *Bayesian block* method is described in Chapter 6.

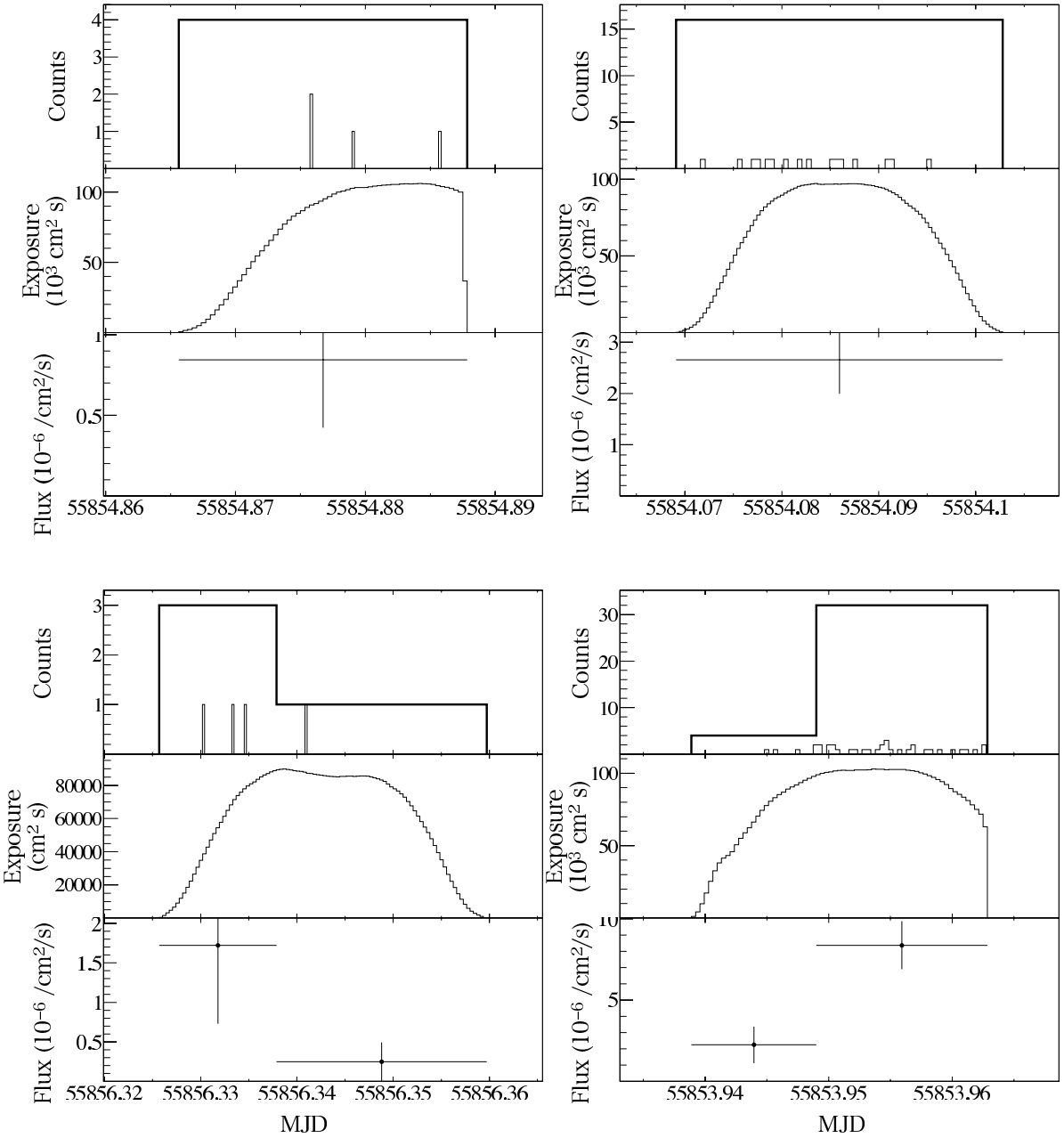

Figure 6.9: Examples illustrating how the *Bayesian block* works to detect sub-orbit variability for different statistics. Four examples of orbits presented were taken from flare #5 in PKS 1510–089, and analysed with $fp = 0.1$. Each exposure typically lasts ∼30 minutes. (*upper panels*) Raw count histogram with piecewise constant blocks obtained with *Bayesian* blocks. (*middle panels*) Exposure variation during a single orbit. (*lower panels*) Flux values calculated by dividing counts by exposure.

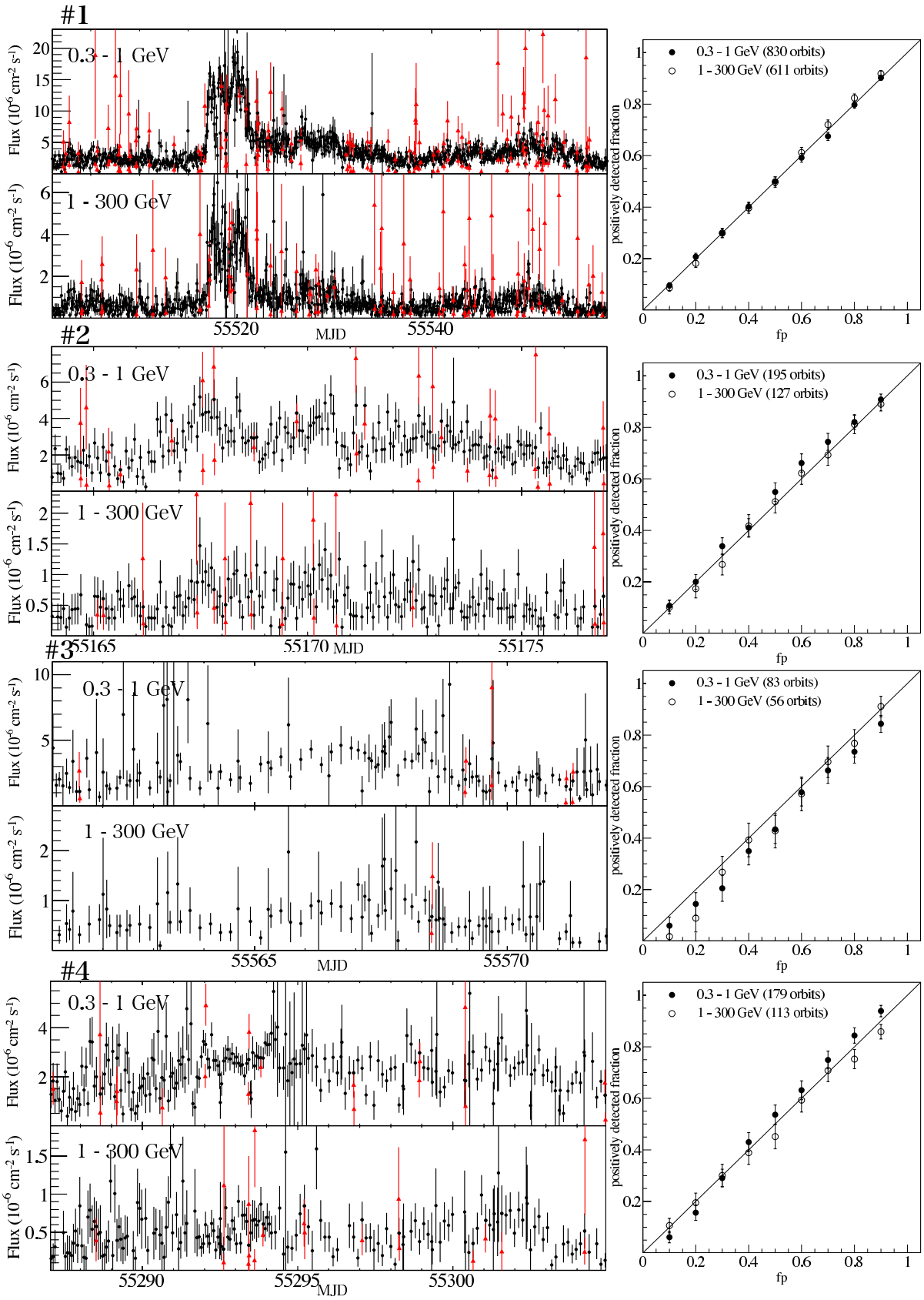

Figure 6.10: Results of *Bayesian blocks*. 3C 454.3. (*left*) Orbit-binned light curves with BB results. Black points represent orbital-binned light curves calculated by aperture photometry. Red triangle points show flux change. fp value was fixed at 0.1.(*right*) Relation of fp value and positively detected fraction. Observational error is added assuming binomial distribution following B(n, fp).

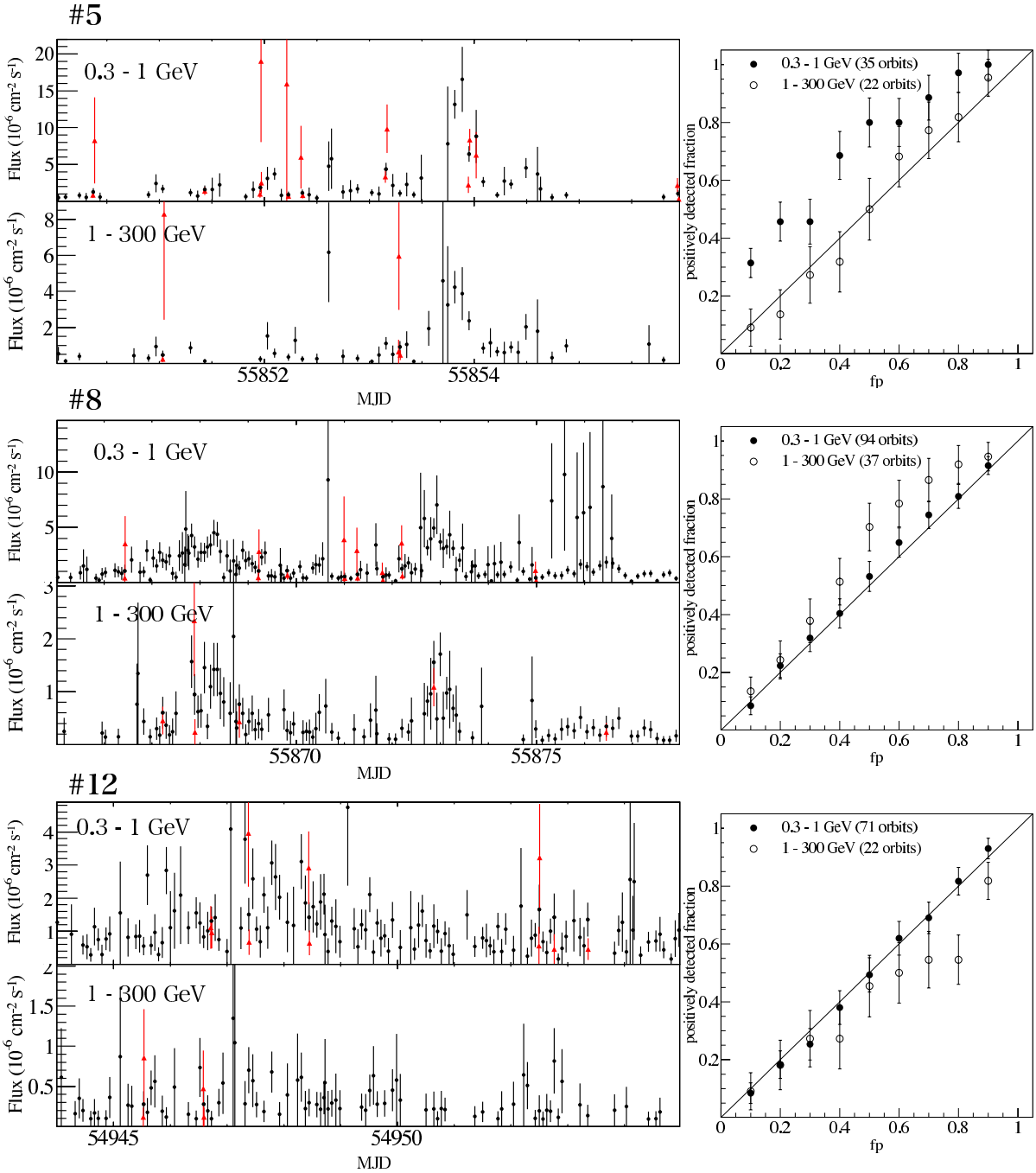

Figure 6.11: Results of *Bayesian blocks*. PKS 1510–089. (*left*) Orbit-binned light curves with BB results. Black points represent orbital-binned light curves calculated by aperture photometry. Red triangle points show flux change. fp value was fixed at 0.1.(*right*) Relation of fp value and positively detected fraction. Observational error is added assuming binomial distribution following B(n, fp).

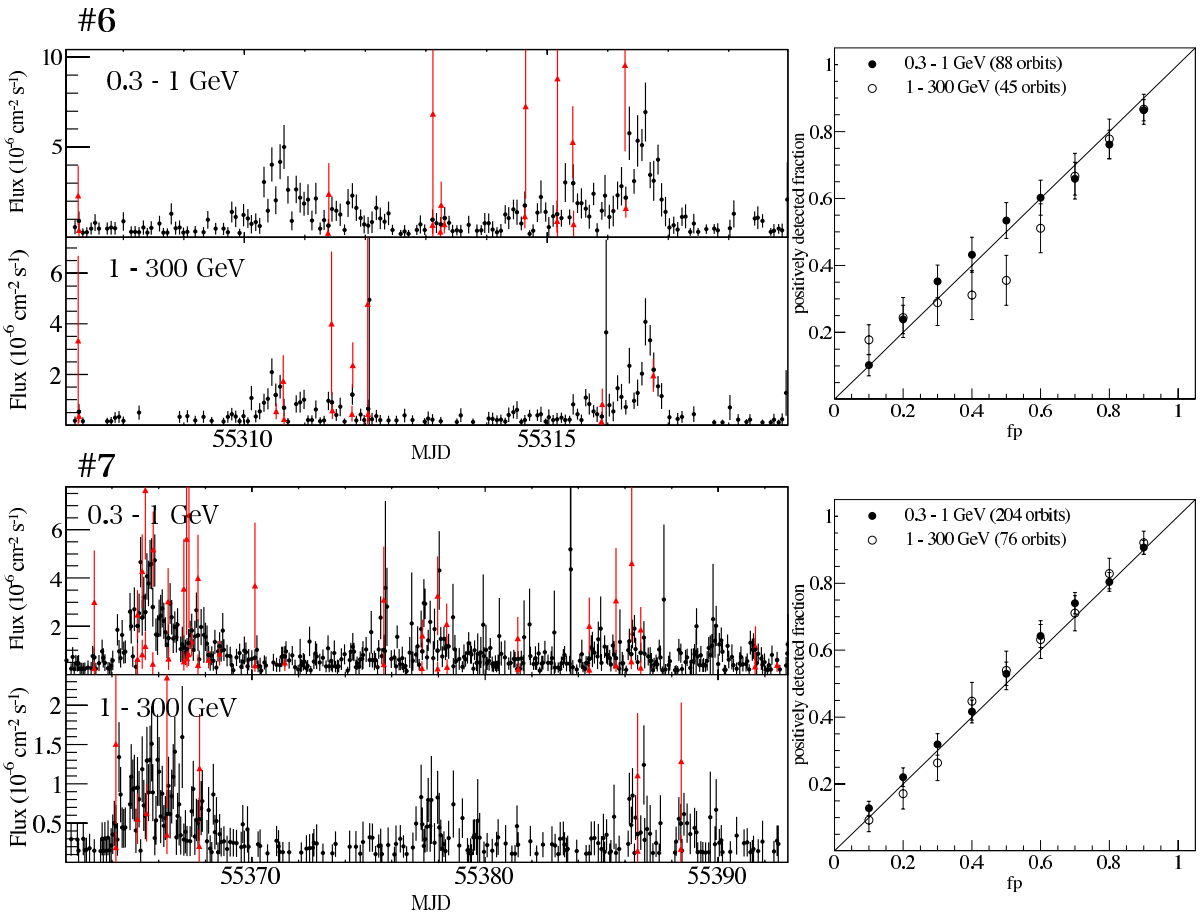

Figure 6.12: Results of Bayesian blocks. 4C21.35. (*left*) Orbit-binned light curves with BB results. Black points represent orbital-binned light curves calculated by aperture photometry. Red triangle points show flux change. fp value was fixed at 0.1.(*right*) Relation of fp value and positively detected fraction. Observational error is added assuming binomial distribution following B(n, fp).

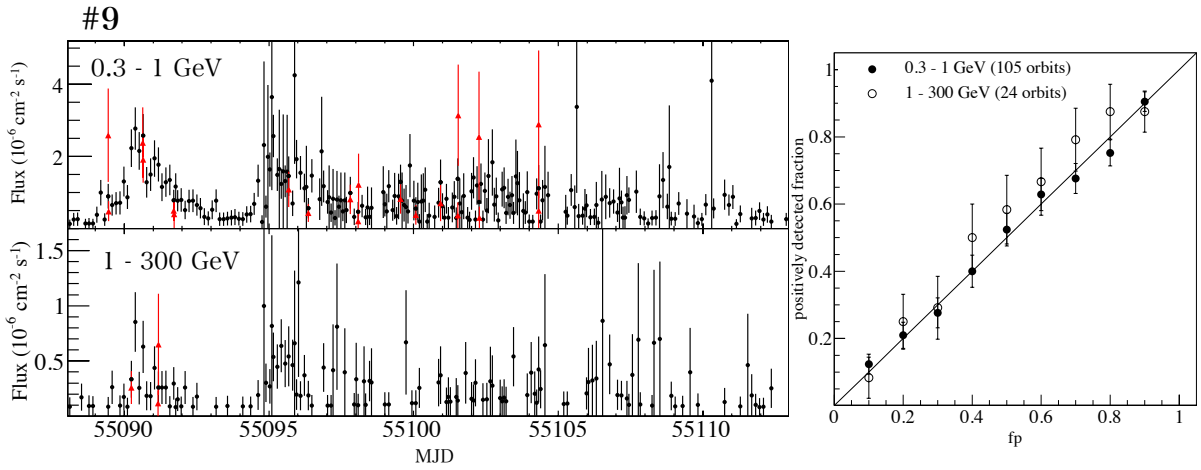

Figure 6.13: Results of Bayesian blocks. 3C 273. (*left*) Orbit-binned light curves with BB results. Black points represent orbital-binned light curves calculated by aperture photometry. Red triangle points show flux change. fp value was fixed at 0.1.(*right*) Relation of fp value and positively detected fraction. Observational error is added assuming binomial distribution following $\mathrm{B}(\mathrm{n}, \mathrm{fp})$.

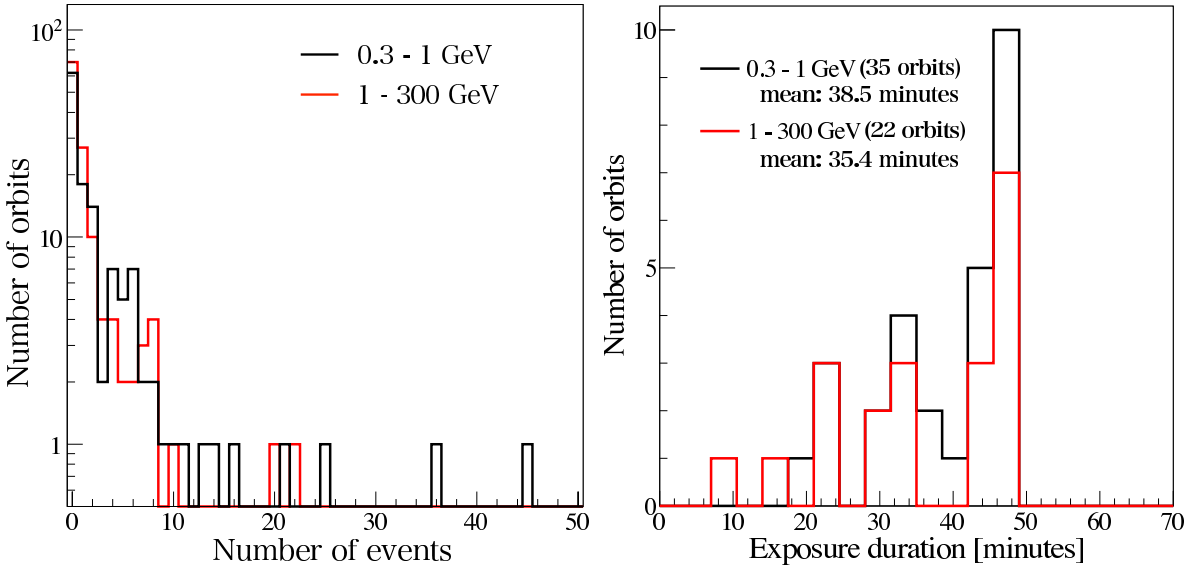

Figure 6.14: Distributions of exposure duration and number of events per orbit during flare #5 in PKS 1510–089. (*left panel*) Distribution of number of photons in ROI(3°) for each orbit during the flare. Orbits with more thant 3 photons were taken into account for the Bayesian analysis. (*right panel*) Distribution of exposure duration for orbits with more than 3 photons.

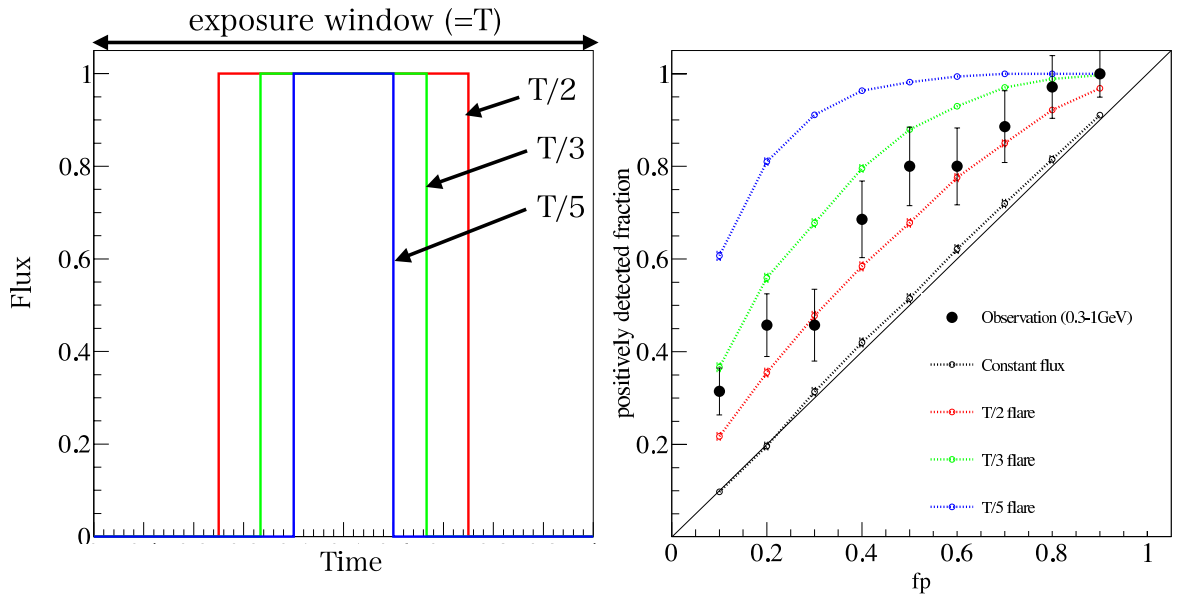

Figure 6.15: Bayesian block simulations with rectangle flare profile compared with #5 flare in PKS 1510-089 (0.1 - 3 GeV). (*left*) Assumed rectangle flare profile with duration of T/2, T/3, and T/5, where T corresponds to time window of the LAT exposure. (*right*) Simulated detected fraction and observation results.

Chapter 7

Numerical Modeling of Jets

From the systematic analysis of the brightest blazar flares in this thesis, blazars were discovered to be drastically variable in GeV energy range with time scale of hours, even as short as one hour. Moreover, further search for shorter time scale variability with *Bayesian block* method found no significant sub-hour variability for nine of the ten selected flares, while there was only a slight indication for sub-hour variability in only one flare which took place in PKS 1510–089. Now the question is how these findings improve our understandings of relativistic jets. In this chapter, we interpreted the observed GeV short time variability with numerical modeling method to extract physical evolution involved during the flares, and impose new constraints on emissions from relativistic jets.

7.1 Issues in Locating the Blazar Emission Zone

Current studies have never reached an agreement on location of emitting region(s) in blazar jets.The combined radio and optical polarization studies of blazar sources suggest the dominant emitting region to be located as far as $\sim 10\,\mathrm{pc}$ from SMBHs ("far-dissipation zone" scenario; e.g., Marscher et al. 2010). On the other hand, other study based on the overall SED modeling suggests much closer distances from the central engine, $\sim 0.01\,\mathrm{pc}$ ("near-dissipation zone" scenario; e.g., Ghisellini 2010).

The huge disagreement seems to be caused by two problems regarding the conventional modeling of balzar jets which utilizes multi-wavelength data of observations ranging from radio to gamma-ray. First, the collected multi-wavelength data is usually quasi-simultaneous or non-simultaneous due to operational issues for the instruments of each wave band, such as weather or observation mode of satellites. As blazars show rapid variability during flares, we could not infer multi-wavelength time evolution of flares

with sufficient quality by utilizing unevenly sampled data set. Second, current modelings have been done for data integrated over relatively long duration, e.g. more than days. This introduces a concern for reaching wrong interpretation by modeling data with such insufficient time resolution, since apparently coherent single flare would be resolved into superpositions of sub-flares, as we noticed from the analysis in chapter 5. Furthermore, the one zone emission model which is widely used for modeling broadband SEDs often could not explain the simultaneous observation results (see 2.3.3 for detail). Thus putting constraints on emitting region from single-wavelength data is of importance, and that is why we focused on only the *Fermi*-LAT data in the analysis in this thesis.

A common method for locating blazar emitting region simply utilizes the timescale of variability observed in certain wavelength. The conventional argument goes like this. Let us assume time interval between flare starts and flux changes by factor 2 in observer rest frame as Δt. In the jet rest frame, the interval between flare starts and emitting power changes by factor 2 is expressed as $\delta\Delta t$, assuming the jet moving toward the Earth with the Doppler factor δ. On the other hand, the size of the emitting region (R) should be less than its light crossing time R/c. Considering above conditions, we could obtain $R/c \leq \delta\Delta t$ which constrains R, $R \leq c\delta\Delta t$. Thus $c\delta\Delta t$ means the maximum size of the emitting region allowed for producing variability time scale of Δt. Then assuming conical jet with simple opening angle of about the inverse of bulk Lorentz factor; $1/\Gamma$ yields the location of emitting region from the super massive black hole as $c\delta\Gamma\Delta t$. According to this argument, producing 1 hour variability requires GeV emitting region to be 0.01 pc from the core in the case of PKS 1510–089.

However, problems arise if we consider such a close dissipation region to the central blackhole. First, high energy emissions from FSRQs are produced via inverse Compton scattering of photons in broad line region (BLR) and hot dusty torus (HDT), with negligible contribution from synchrotron self Compton radiation (see 2.1.2). Typical sizes of BLR and HDT are considered to be 0.1 pc and 1 pc, and the typical energy of photons in each photon field is 10 eV and 0.1 eV, respectively (Sikora et al. (1994), Pian et al. (2005), Nenkova et al. (2008)). If we consider the gamma-ray emitting zone at 0.01 pc from the central blackhole, the gamma-ray emitting electrons would be very quickly cooled by the dense photon field of BLR. In spite of the estimated cooling time for the gamma-ray emitting electrons of less than ten minutes (see Eq. (7.7) and Figure 7.1 for the calculation), decaying time scale of flares as short as 10 minutes has never been observed for any blazars.

Another problem relevant to the estimation of emitting region from the variability timescale is caused by detection of rapid TeV variability in FSRQs. As is reviewed

in chapter 2, very recently MAGIC detected rapid variability with timescale of several minutes from 4C 21.35 (Aleksić et al. (2011)). According to the rough estimation of the emitting region from this variability timescale yields the emitting zone at $\sim 1 \times 10^{-3}$ pc from the central blackhole. However, TeV gamma-rays could not come from such a close zone to the blackhole since they could not escape from the dense BLR photon field due to $\gamma\gamma$ absorption. According to Eq.(2.21), gamma-rays above 30 GeV would be absorbed by BLR photon with energy of 10 eV.

These observational results clearly show that the rough estimation of balzar emission zone from the observed timescale does not fully work, and require more realistic model for producing rapid gamma-ray variability. In this chapter, we consider particle acceleration by internal shock as the relevant process for producing the rapid variability.

7.2 Constraints on Blazar Emission Zone

In this section, we present how gamma-ray variability is interpreted by the internal shock scenario. Next we present strategy of modeling for observed rapid gamma-ray variability with *Fermi*-LAT.

7.2.1 Rising Time Scale

As is reviewed in chapter 2, the internal shock model assumes two blobs with different velocity collide each other, and the timescale of the shock running inside the merged blob determine the timescale of particle acceleration. This means that we don't have to place the emitting region at very close to the central blackhole to reproduce the observed rapid variability (rapid rising profile). The observed rapid rising profile could be reproduced even at distant position from the central blackhole as long as the shocked wave in thin shell accelerates enough amount of particles accounting for the observed flare. For example, the variability of one hour could be produced by shocked region whose thickness is 3×10^{16} cm ($\sim$0.01 pc) according to Eq.(2.40).

7.2.2 Decaying Time Scale

After the shock ran through the merged blob, there are no more processes for gaining energy of particles, and the accelerated particles lose their energy by physical processes such as synchrotron radiation or inverse Compton scattering. In FSRQs, gamma-ray emitting electrons lose their energy via inverse Compton scattering of soft photons in

external photon fields (BLR or HDT). This means cooling timescale of relativistic electrons via inverse Compton scattering is reflected to the observed decaying timescale of gamma-ray time profile.

Well-resolved decaying time profile during flares would provide important clues to determine gamma-ray emitting region by comparing it with estimated cooling time scales. Energy density of BLR and HDT falls with distance from the central black hole beyond their typical sizes (Sikora et al. (1994), also see the left panel in Figure 7.1). This implies that radiative cooling time scale becomes longer as the emitting region goes away from the central blackhole. Thus, we could put constraints on gamma-ray emitting region by comparing observed decaying time scale with estimated cooling time. (But see the discussion below where we found another factor contributing to the observed decaying profile.) For estimating dependence of cooling time on distance from the central black hole, we presented expected cooling time scale and external photon field.

Cooling Time of Relativistic Electrons

Typical cooling time of relativistic electrons with Lorentz factor γ is described as,

$$t'_{\rm cool} = \frac{\gamma}{|{\rm d}\gamma/{\rm d}t'|} \tag{7.1}$$

where values with primes are measured in jet comoving frame and ${\rm d}\gamma/{\rm d}t'$ is cooling rate of electrons.

Lorentz factor of electrons which emit photon with energy $\epsilon_{\rm IC}$ via inverse Compton scattering of soft photon $\epsilon_{\rm ext}$, which is energy of external photon in observer frame, is calculated as follows (in the Thomson regime).

$$\epsilon'_{\rm IC} \simeq \gamma^2 \epsilon'_{\rm ext} \tag{7.2}$$

Then observed energy of this photon could be calculated considering energy of the external photon would be amplified by bulk Lorentz factor of jet and $\epsilon_{\rm IC} = \delta\epsilon'_{\rm IC}$, where δ is the Doppler factor of jet (Sikora et al. 2002).

$$\epsilon_{\rm IC} \simeq \gamma^2 \delta^2 \epsilon_{\rm ext} \tag{7.3}$$

$$\gamma \simeq \frac{1}{\delta}\left(\frac{\epsilon_{\rm IC}}{\epsilon_{\rm ext}}\right)^{\frac{1}{2}} \tag{7.4}$$

External Compton radiation is the dominant process for electron cooling and the cooling rate is expressed as follows using energy density of external photon field $U'_{\rm ext}$.

$$\frac{{\rm d}\gamma}{{\rm d}t'} = -\frac{4\sigma_{\rm T}}{3m_e c} U'_{\rm ext}\gamma^2 \tag{7.5}$$

Then the formula of cooling time scale is written as,

$$t'_{\rm cool} \simeq \frac{3m_{\rm e}c}{4\sigma_{\rm T}U'_{\rm ext}\gamma} \simeq \frac{3m_{\rm e}c\delta}{4\sigma_{\rm T}U'_{\rm ext}} \left(\frac{\epsilon_{\rm ext}}{\epsilon_{\rm IC}}\right)^{\frac{1}{2}} \tag{7.6}$$

Finally we could derive cooling time scale of relativistic electrons in the observer rest frame considering the jet is going toward us.

$$t_{\rm cool} \simeq \frac{t'_{\rm cool}}{\delta} \simeq \frac{3m_{\rm e}c}{4\sigma_{\rm T}U'_{\rm ext}} \left(\frac{\epsilon_{\rm ext}}{\epsilon_{\rm IC}}\right)^{\frac{1}{2}} \tag{7.7}$$

Energy Density of External Photon Fields

We consider a spherically symmetric external photon field which has monochromatic temperature and distance dependence of energy density by a factor $1/(1 + r^2/R^2_{\rm ext})$, where r is distance from the central black hole and $R_{\rm ext}$ is the typical size of the external photon field (Sikora et al. (1994), Sikora et al. (2002), Sikora et al. (2009)). Emission from this photon field would be described as single black body radiation at temperature $T_{\rm ext}$, which is expressed as below.

$$B_{\rm ext}(\nu,\, T_{\rm ext}) = \frac{2h\nu^3/c^2}{\exp(h\nu/kT_{\rm ext}) - 1} \tag{7.8}$$

The energy density in laboratory frame is obtained by integrating this equation over frequency.

$$\begin{aligned} u_{\rm ext}(r) &= \frac{1}{c}\int B_{\rm ext}(\nu,\, T_{\rm ext}){\rm d}\nu{\rm d}\Omega \frac{1}{1 + (r/R_{\rm ext})^2} \\ &= \frac{4\sigma T^4_{\rm ext}}{c} \frac{1}{1 + (r/R_{\rm ext})^2} \\ &= \frac{L_{\rm ext}}{\pi c R^2_{\rm ext}} \frac{1}{1 + (r/R_{\rm ext})^2} \end{aligned} \tag{7.9}$$

where σ is Stefan-Boltzmann coefficient and $L_{\rm ext} = 4\pi R^2_{\rm ext}\sigma T^4_{\rm ext}$.

The comoving energy density of the external radiation field is calculated as follows.

$$\begin{aligned} u'_{\rm ext}(r) &= \frac{1}{c}\int I'_{\rm ext}{\rm d}\Omega' \\ &= \frac{1}{c}\int I_{\rm ext}\delta^{-2}{\rm d}\Omega \\ &\simeq \Gamma^2 u_{\rm ext} \\ &\simeq \frac{\Gamma^2 L_{\rm ext}}{\pi c R^2_{\rm ext}} \frac{1}{1 + (r/R_{\rm ext})^2} \end{aligned} \tag{7.10}$$

where δ is Doppler factor of the propagating shell.

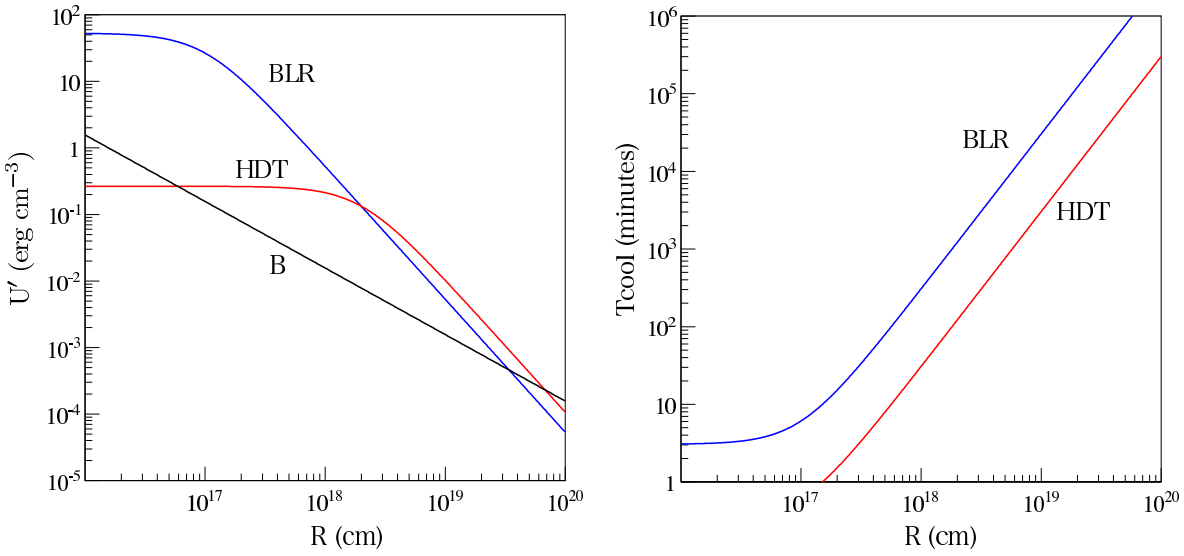

Figure 7.1: (*left*) Energy density of the magnetic field, BLR radiation field, and hot dusty torus. $U_B = B_0^2/8\pi^2 \times R_0/R$ where $R_0 = 0.7 \times 10^{18}$ and $B_0 = 0.75G, L_{BLR} = 0.5 \times 10^{45}, R_{BLR} = 0.12 \times 10^{18}, L_{IR} = 1.0 \times 10^{45}$, and $R_{IR} = 1.94 \times 10^{18}$ are assumed. *right*) Dependence of cooling time scale of relativistic electrons in BLR and HDT on distance from the central core, which was calculated by Eq.(7.7).

Radial Dependence of Electron Cooling Time

Finally we could derive cooling time scale at given distance from the central black hole by combining Eq.(7.5) and Eq.(7.9). For example, distance dependence of the external photon fields and cooling time scale in the laboratory frame is estimated for PKS 1510–089 in Figure 7.1, where parameters of the external fields is taken from Barnacka et al. 2013. Cooling time scale of gamma-ray (100 MeV) emitting electron is very sensitive to its location, namely several minutes at 10^{17} cm and ∼200 minutes at 10^{18} cm for BLR photon field. This makes it very important to probe gamma-ray flux variability with hour-scale time resolution in order to determine the emitting region.

7.3 Application of `BLAZAR` Code to the Gamma-ray Rapid Variability

The `BLAZAR` code was developed to propagate time evolution of emissions from relativistic jets, based on the internal shock scenario. A uniform and expanding shell moving along

a jet is assumed as emitting zone in this model. We utilized "BLAZAR" model developed in Moderski et al. (2003) and Moderski et al. (2005) for our modeling of the rapid flares. The prescription of the code to study the time evolution of relativistic electrons in jets and to calculate the observed emission are briefly described below. For further detail, see Moderski et al. (2003).

7.3.1 Electron Evolution

The code assumes conical jet geometry shown in Figure 7.2. Evolution of electron energy distribution while a shell propagating along the conical jet is obtained by solving the kinetic equation for the total population of relativistic electrons, assuming that electron injection function and energy densities of magnetic field and of external radiation fields are uniform across the shell. The equation is written in the following form.

$$\frac{\partial N_\gamma}{\partial t'} = -\frac{\partial}{\partial \gamma}\left(N_\gamma \frac{\mathrm{d}\gamma}{\mathrm{d}t'}\right) + Q \tag{7.11}$$

which could be rewritten as,

$$\frac{\partial N_\gamma}{\partial r} = -\frac{\partial}{\partial \gamma}\left(N_\gamma \frac{\mathrm{d}\gamma}{\mathrm{d}r}\right) + \frac{Q}{c\beta_\Gamma \Gamma} \tag{7.12}$$

where

$$\frac{\mathrm{d}\gamma}{\mathrm{d}r} = \frac{1}{\beta c \Gamma}\left(\frac{\mathrm{d}\gamma}{\mathrm{d}t'}\right)_{\mathrm{rad}} - \frac{2}{3}\frac{\gamma}{r} \tag{7.13}$$

Q is the electron injection function (defined in 7.3.3), N_γ is number density of electrons which have Lorentz factor γ, r is the location of the emitting shell measured from the central blackhole, Γ and β_Γ are bulk Lorentz factor and velocity of jet (emitting shell) and t' is time measured in jet rest frame. The second therm in above equation represents the adiabatic losses due to two-dimensional conical expansion of the shell.

7.3.2 Physical Processes

Synchrotron radiation and inverse Compton scattering, which are the major radiative processes contributing to blazar emission, are implemented in the code. Also gamma-ray absorption in the broad line region and hot dusty torus, which become significant for observed sub-TeV spectrum is implemented in the code. This code offers correct treatment for cross section of inverse Compton scattering in Klein-Nishina regime which become significant in the high energy gamma-ray emission in blazars (See chapter 2 for the process).

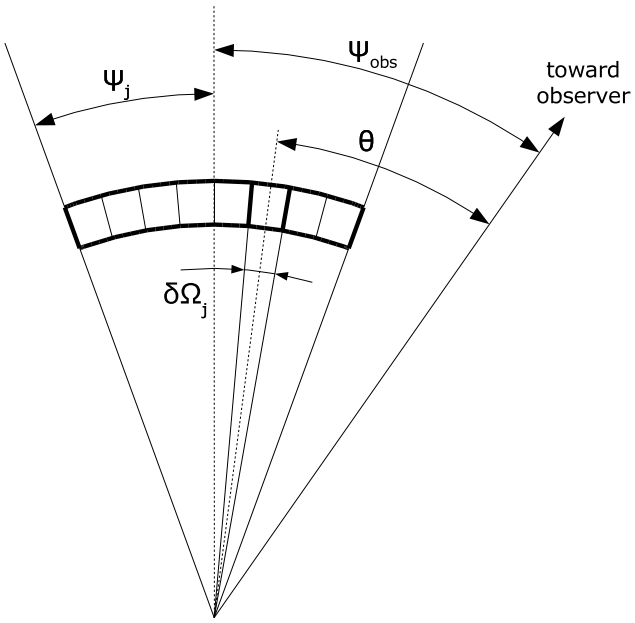

Figure 7.2: A figure illustrating the geometry taken into account in the BLAZAR code, which was taken from Moderski et al. (2003). An shell which encloses relativisric electrons within the opening angle of the jet ($2\psi_j$) is considered. The shell is divided into a number of cells (100 cells in our calculation). The observer is located at the angle $\psi_{\rm obs}$ from the jet axis. Observed SED at given moment is obtained by integrating over θ contributions from cells located at different radii.

7.3.3 Calculation Procedure and Model Parameters

The BLAZAR code assumes particle acceleration via internal shock, which is implemented as constant injection of relativistic electrons while the shell propagating along the jet. The shell is assumed to move along the jet with gradually expanding its volume, and time evolution of the shell is calculated. At first, time evolution of electron distribution, synchrotron spectrum, and synchrotron self Compton (SSC) spectrum in the jet rest frame are calculated. Next, time profile of the observed flux is calculated. Detail of the calculation is described below.

- Step1
  Calculate electron distribution on various distances from the center, and synchrotron luminosity and SSC luminosity in a jet comoving frame at various distances. Continuous injection of relativistic electrons expressed in Eq.(7.14) is assumed while the shell propagates from $R_{\rm start}$ to $R_{\rm end}$, which are also input parameters for the model. After the shell goes beyond $R_{\rm end}$, there is no injection any more. Evolution of the electron distribution and corresponding emission are calculated until the shock reaches at $R_{\rm stop}$.

- Step2
  Calculate the observed luminosity of the source at various times. Observed SED at given time is calculated by integrating over θ contributions from cells located at different radial distances. A set contributing cells at given observation time ($t_{\rm obs}$) is collected by solving $R = ct_{\rm obs}/(1-\beta\cos\theta)$, where R is radial distance from the top of the conical geometry and Γ is the bulk Lorentz factor.

The parameters of the location of electron injection ($R_{\rm start}, R_{\rm end}, R_{\rm stop}$) shown above are input parameters to the code. We could also input the distribution of injected electrons, energy density and size of the external photon fields, that are described below.

Geometry of shocked shell

We could specify bulk Lorentz factor, angular width, and the observation angle of the shell. We could also specify locations where injection starts($R_{\rm start}$), ends($R_{\rm end}$), and calculation stops($R_{\rm stop}$).

Energy distribution of injected electrons

Constant injection of relativistic electrons is assumed in the BLAZAR model. The electron distribution expressed in the following formula is assumed to be produced by the shock

acceleration. The injection function is written as,

$$Q(\gamma) = \begin{cases} K_e \gamma_b^{p-q} \gamma^{-p} & \text{for} \quad \gamma_{\rm min} < \gamma < \gamma_b \\ K_e \gamma^{-q} & \text{for} \quad \gamma_b < \gamma < \gamma_{\rm max} \end{cases} \tag{7.14}$$

where K_e is the normalization of the injection function, p and q are spectral indices for injecting electrons, and γ_b, $\gamma_{\rm min}$, $\gamma_{\rm max}$ are electron Lorentz factors for break, minimum, and maximum energy. The parameters characterizing the injected electron distribution are input parameters to the model.

External photon field

Radial size, temperature, and energy density are input parameters for external photon field. Broad line region and hot dusty torus are taken into account, with radial dependence of the photon fields assumed to obey Eq.(7.9).

7.4 Modeling the Observed Gamma-ray Rapid Variability

7.4.1 Flare Selection for Modeling

We performed modeling of GeV variability for the selected brightest flares. Isolated single flares with well resolved flaring profiles in 3-hour binning were to be extracted from Figure 5.1, Figure 5.2, Figure 5.3 and Figure 5.4. Apparently unresolved flares would introduce extra complexity to the modeling procedure because various flares would be reflected in the light curves as sub-structural components. For example, chaotic and moderate variability in 3C 454.3 suggests the observed time profile is composed of superpositions of many sub-flares, thus inappropriate for the modeling.

On the other hand, outbursts in PKS 1510–089 around MJD 55854 (included in flare #5) and MJD 55873 (included in flare #8) show coherent profile even in 3-hour binning, and an outburst in 4C 21.35 around MJD 55317 (included in flare #6) also shows marginally resolved profile. If observed time profiles of these flares are actually contributed from a single component, we could assume collision of two blobs produced the observed huge flares in the framework of the internal shock scenario. We chose three-hour binned light curves of these three apparently resolved flares for the modeling in this chapter.

7.4.2 PKS 1510–089, #5

Light curve of the recorded huge GeV outburst in PKS 1510-089 which reached daily flux of 14.3×10^{-6} ph s^{-1} cm^{-2} (100 MeV $<$ E $<$ 300 GeV) was modeled here. In principle truly simultaneous multiwavelength data at the moment are needed to model rapidly varying emissions from blazars, however such data do not exist.

Values of parameters decided in Barnacka et al. (2013) provide rough standard since they performed broadband SED fitting based on most recent multi-wavelength observations taken in 2009. We basically used the same parameters as presented in the literature, while only parameters for normalization of electron injection(K_e) and the location of emitting shell ($R_{\rm start}, R_{\rm stop}, R_{\rm end}$) were changed based on observed gamma-ray properties of the flare. Model input parameters for PKS 1510–089 are shown in Table 7.1.

Parameter Constraints

We would briefly describe how the model input parameters for electron injection, external photon fields, and geometry of the jet were constrained from observations. Spectral index of electrons were decided to explain multiwavelength SED data. The thing is that FSRQs including PKS 1510–089 are known to show harder spectra in GeV range during flares, with energy break around several GeV (Abdo et al. (2009b), Tanaka et al. (2011)). In this sense, parameters for electron injection used in Barnacka et al. (2013) provided most reliable values since they modeled multiwavelength observations during a recent flare in PKS 1510–089.

Size and intensity of external photon fields (broad line region and hot dusty torus) were fixed by independent observations and very basic assumptions/modeling results regarding the environment of active SMBH. From UV observations, disk luminosity were estimated as $\sim 5 \times 10^{45}$ erg s^{-1} in several literature (Nalewajko et al. (2012), Celotti et al. (1997), Kataoka et al. (2008)). Luminosity of broad line region and hot dusty torus are commonly estimated from disk luminosity assuming a fraction of reprocessed emission from the accretion disk, which were assumed to be $\xi_{\rm BLR} = 0.1$ and $\xi_{\rm HDT} = 0.2$ here. The size of broad line region was estimated based on the following equation presented in Pian et al. (2005), in which they characterized the relation of size of broad line region obtained by reverberation mapping(Peterson et al. (2004)) and UV spectra observed with *Hubble Space Telescope*.

$$R_{\rm BLR} = (22.4 \pm 0.8) \times \left(\frac{\lambda L_\lambda (1350\text{Å})}{10^{44}\,{\rm erg\,s^{-1}}} \right) \text{light days} \tag{7.15}$$

Thus we could obtain $R_{\rm BLR} = 0.12 \times 10^{18}$ cm. On the other hand, the size of hot dusty

torus is approximately estimated as $R_{\rm DT} \simeq 2.9\,{\rm pc} \times \left(\frac{T}{1000K}\right)^{-2.6} \simeq 1.94 \times 10^{18}{\rm cm}$ (see Tavecchio & Ghisellini (2008), Nenkova et al. (2008), Sikora et al. (2009)), where the temperature of the torus was set to 1,800 K according to Nalewajko et al. (2012). From the estimations of size and luminosity for the external photon fields, finally we obtained the energy density as $u_{\rm BLR} \simeq 0.09\,{\rm erg\,s^{-1}}$ and $u_{\rm HDT} \simeq 5 \times 10^{-4}\,{\rm erg\,s^{-1}}$.

There are some general assumptions regarding the jet geometry and kinematics which are very common for very different models of the blazar emission discussed in the literature. We assume that the jet at the position of the blazar emission zone is (a) conical, (b) free, and (c) characterized by the constant bulk velocity equal to the terminal jet velocity. (a) means that we can relate the jet radius(r) to the distance from the core(R) by a simple scaling relation $R \simeq \theta_{\rm jet} r$, where $\theta_{\rm jet}$ is small (by assumption) jet opening angle. (b) means that the jet opening angle $\theta_{\rm jet} \simeq 1/\Gamma$ where Γ is the jet bulk Lorentz factor, when considering the free expanding jet. (c) means that we can identify the jet bulk velocity Γ within the blazar emission zone with the jet bulk velocity inferred from observations of superluminal motions at larger (>pc) scales, because we assume that at the position of the blazar emission zone the jet is already accelerated up to its terminal (maximum) velocity, which is then roughly constant along the outflow.

Note that in addition we assume that the jet opening angle is of the order of the jet viewing angle, namely $\theta_{\rm obs} \simeq \theta_{\rm jet}$. This assumption can be justified by the presence of a beaming which requires $\theta_{\rm obs} \leq \theta_{\rm jet}$, and the fact that the observations of extreme superluminal motion exceeding $20c$ (Homan et al. (2001), Homan et al. (2002)) requires the observation angle of jet to maximize the superluminal motion, that is, $\theta_{\rm obs} = 1/\Gamma$.

We set blazar zone considering the observed time scale in the gamma-ray flare. Distance of the shock propagation in the observer rest frame, which corresponds to the distance between the position where electron injection starts and stops, was decided considering rising time of the flare. The Distance range of the shock operation dealt in the `BLAZAR` code is written as (Eq.(49) in Moderski et al. (2003)),

$$\Delta {\rm r}_{\rm coll} \simeq \frac{c t_{\rm fl}}{1 - \beta \cos\theta_{\rm obs}} \frac{1}{1+z} = \frac{c t_{\rm fl} \Gamma \delta}{1+z} \tag{7.16}$$

where $t_{\rm fl}$ is rising timescale of the flare, β and Γ are velocity and bulk Lorentz factor of the shocked shell, and δ is Doppler factor defined as $[\Gamma(1 - \beta\cos\theta_{\rm obs})]^{-1}$. Producing a flare with rising time scale of ~ 3 hours which is observed rising profile in flare requires $\Delta {\rm r}_{\rm coll} \simeq 2 \times 10^{17}$ cm assuming the model parameters of $\Gamma = 22,\ \delta = 44,$ and $z = 0.36$. From several trials of simulations, we obtain the distance injection starts at 1.1×10^{18} cm and ends at 1.3×10^{18} cm from the central black hole as the best location of emitting zone which explains the observed time profile. Finally the normalization of the electron

injection is set so that simulated flux coincides with observed GeV flux.

Timing Profile

Simulated light curve is compared with the observed rapid gamma-ray flare in Figure 7.4. Flaring profile generated with `BLAZAR` code is in very good agreement with *Fermi*-LAT observation for both rising and decaying phases. Together with the simulations with different distance from the central blackhole ($R_{\rm start}, R_{\rm stop}, R_{\rm end}$), we could locate the emitting region at $\sim 1.1 \times 10^{18}$ cm with uncertainty of $\sim 0.3 \times 10^{18}$ cm. (See Avni (1976) for the estimation of errors).

In this case, the rising phase of the GeV outburst was contributed from the particle acceleration and emission during the shocked shell propagates from $R_{\rm start}$ to $R_{\rm end}$. The distance the shocked shell propagated is 2×10^{17} cm and radius across the jet cross section is $\mathrm{R_{start}}\theta_{\rm jet} \simeq 1.1 \times 10^{18}\,\mathrm{cm} \times 0.045\,\mathrm{rad} = 5 \times 10^{16}$ cm.

Spectral Profile

Spectral shape significantly changes even within the rapid flare lasting only a day. Time evolution of simulated broadband SEDs is presented in Figure 7.6, and evolution of GeV spectrum during the flare is compared with the simulated SEDs in Figure 7.7. The observed spectra of *Fermi*-LAT were created using data only above 100 MeV, and energy bins which have TS more than 25 (corresponding to 5σ) were plotted on the SEDs. Observed GeV spectrum created in 3-hour binned interval indicates the spectral variation during the flares, namely the spectral break is going to disappear as the flare decays. In other words, the simulated SED peak of inverse Compton scattering gradually became lower as the shell propagates along the jet. Tendency of this profile is well reproduced by the simulations, though still there is some discrepancy.

This trend of break energy during the flare could be understood considering the evolution of electron distribution. The simulated evolution of electron distribution is shown in Figure 7.5. This figure shows that the higher energy electrons lose their energy quicker than lower ones. Since radiative cooling rate is expressed as $\dot{\gamma} \propto \gamma^2$, cooling time scale of electron with energy γ is $\mathrm{T_{cool}} = \gamma/\dot{\gamma} \propto \gamma^{-1}$. Until the injection stops, the number of relativistic electrons grew. After the injection stops, higher energy are cooled very rapidly while lower energy ones are not. As a result, the break energy in electron energy distribution became lower, and this is reflected to the observed spectrum of inverse Compton scattering.

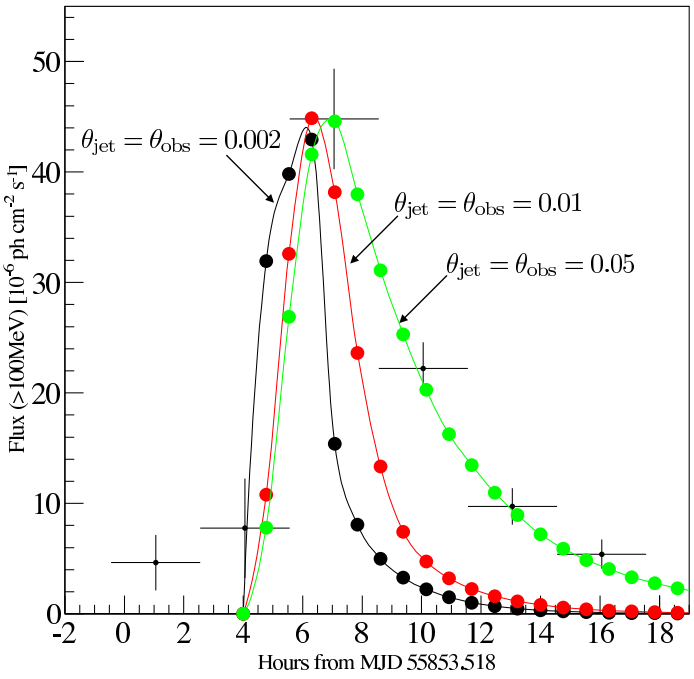

Figure 7.3: Simulated light curves illustrating how the gradient doppler factor affects the observed time profiles. Simulations were performed for different values of $\theta_{\rm jet}$ and $\theta_{\rm obs}$, while the location of emitting region was fixed at $R_{\rm start} = 1 \times 10^{18}$ cm.

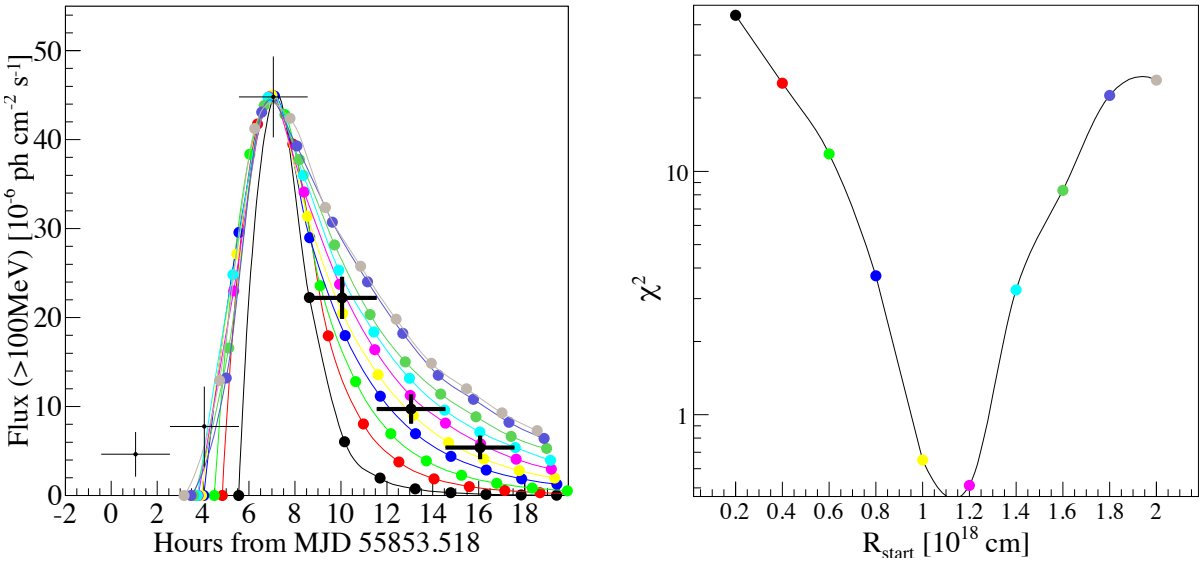

Figure 7.4: Simulated photon flux between 0.1 GeV and 300 GeV superposed on 3-hour binned light curve of the rapid flare (#5) in PKS 1510-089 around MJD 55854. Simulations were performed for different locations of emitting shell. We set $R_{\rm start}$ from 0.2×10^{18} cm to 2×10^{18} cm in 0.1×10^{18} cm steps, and $R_{\rm stop}$ and $R_{\rm end}$ accordingly so that $R_{\rm stop} - R_{\rm start} = 0.2 \times 10^{18}$ cm and $R_{\rm end} - R_{\rm start} = 1.6 \times 10^{18}$ cm. (*left panel*) Simulated light curves where start time of the flare and peak flux were renormalized so that simulated peak flux coincides with observed data. (*right panel*)χ^2 values were calculated for each simulation using decaying three observed points (bold crosses).

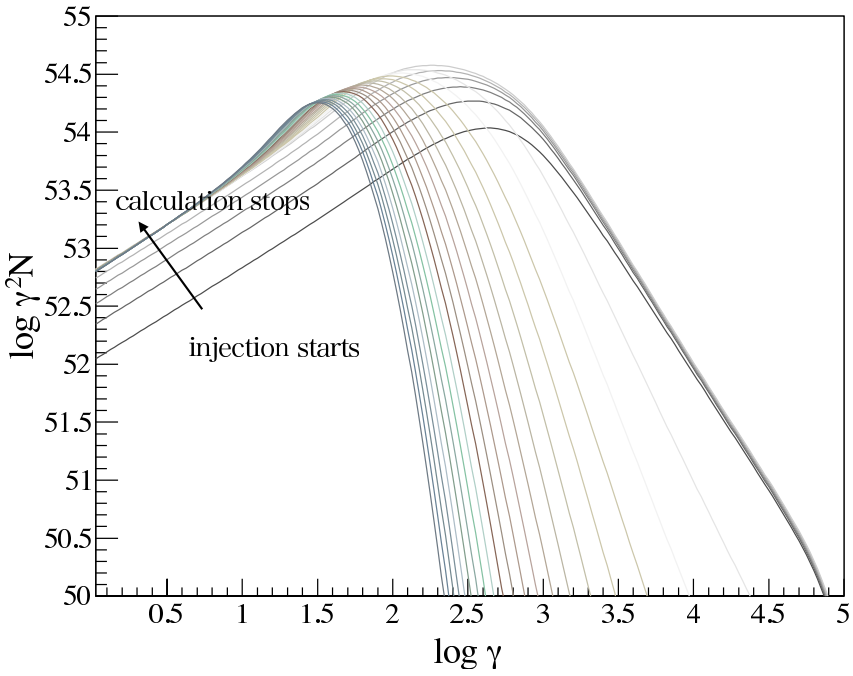

Figure 7.5: Simulated evolution of electron distribution during the flare #5 in PKS 1510–089. γ is Lorentz factor of relativistic electrons and N is the number density of electrons whose Lorentz factor is γ.

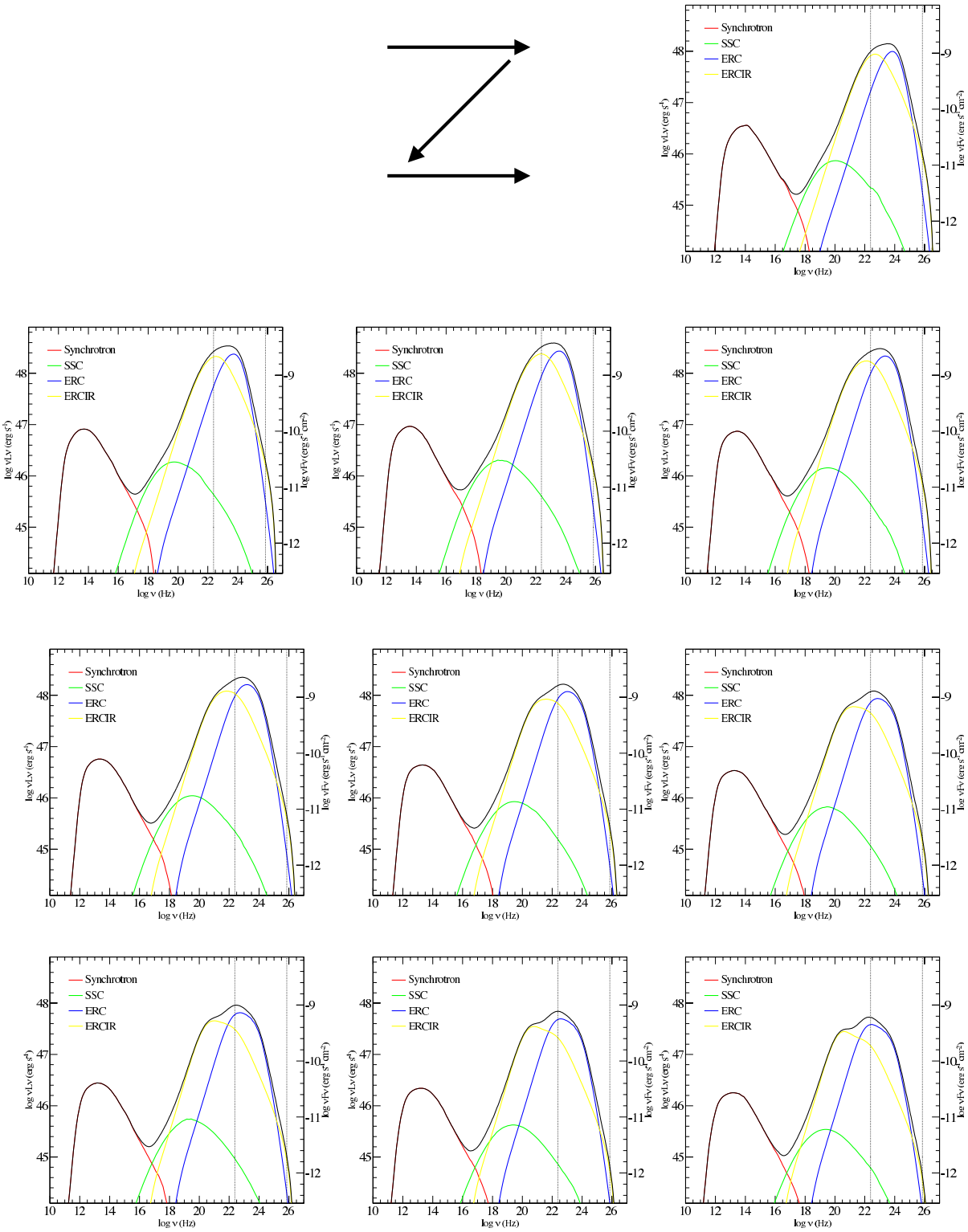

Figure 7.6: Variation of SEDs during the flare #5 in PKS 1510–089. Each SED corresponds to each simulated point in the light curve ($R_{\rm start} = 1.1 \times 10^{18}$ cm) presented in Figure 7.4. Vertical dotted lines show the *Fermi*-LAT energy range (0.1 GeV – 300 GeV).

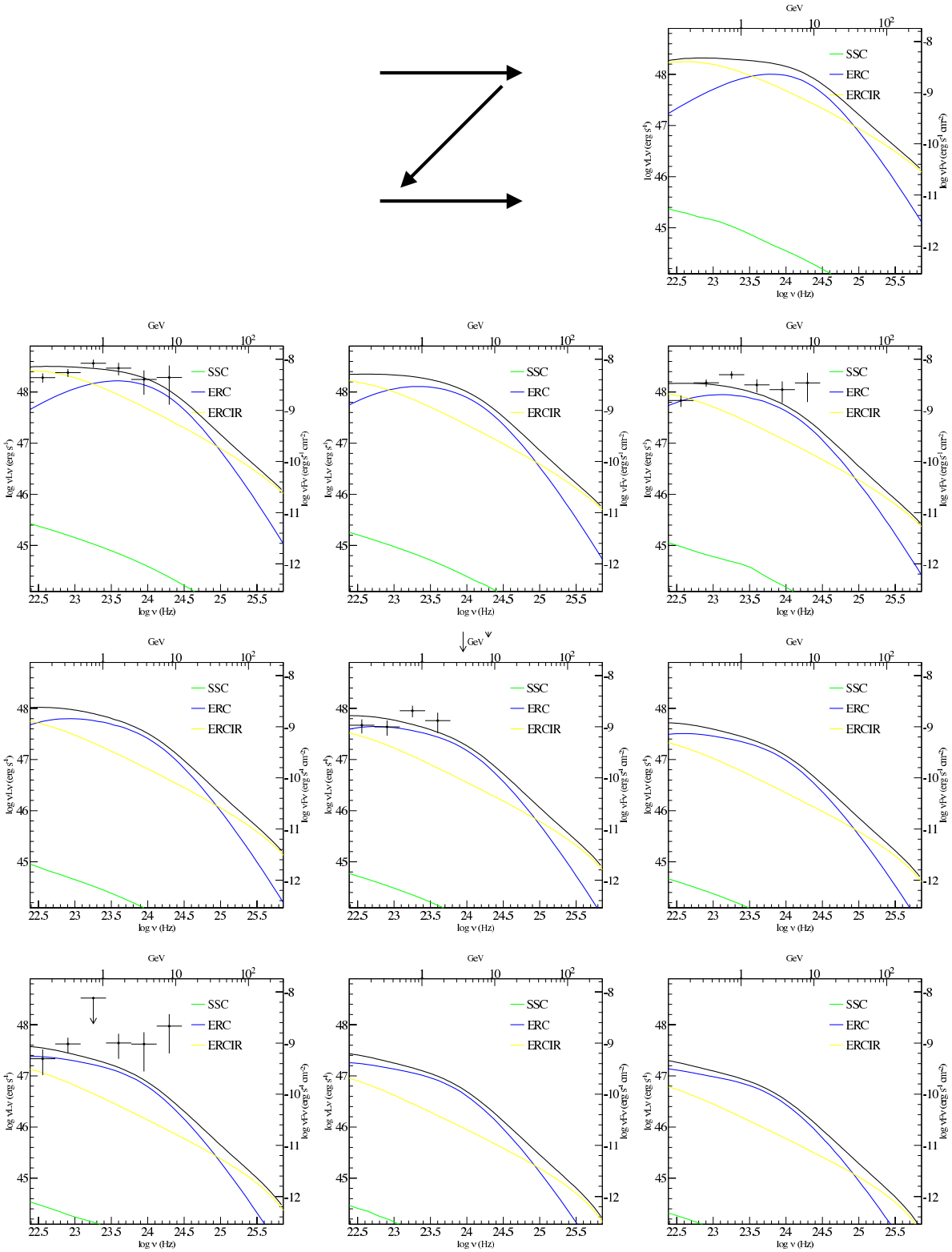

Figure 7.7: Zoomed-up SEDs during the flare #5 in PKS 1510–089 for the *Fermi*-LAT energy range (100 MeV – 300 GeV). Three-hour binned *Fermi*-LAT spectra corresponding to the time of simulated points were drawn on each SED.

Table 7.1: Input parameters for the modeling of flaring state in PKS 1510-089 and 4C 21.35. Parameters of PKS 1510–089 which are changed from those presented in Barnacka et al.(2013) are highlighted.

Parameter name	1510#5	1510#8	4C21#6
Minimum electron Lorentz factor	1		1
Break electron Lorentz factor	900		1000
Maximum electron Lorentz factor	1×10^5		2×10^5
Low-energy electron spectral index p	1.2		2.0
High-energy electron spectral index q	3.4		3.5
Normalization of the injection function $K_e\,(\mathrm{s}^{-1})$	$\mathbf{2.8 \times 10^{47}}$	$\mathbf{3.0 \times 10^{47}}$	$\mathbf{8 \times 10^{48}}$
Bulk Lorentz factor Γ	22		20
Jet opening angle θ_{jet}(rad)	0.045		0.045
Jet viewing angle θ_{obs}(rad)	0.045		0.045
Location where injection starts; R_{start}(cm)	$\mathbf{1.1 \times 10^{18}}$	$\mathbf{3.7 \times 10^{18}}$	0.9×10^{18}
Location where injection stops; R_{stop}(cm)	$\mathbf{1.3 \times 10^{18}}$	$\mathbf{4.6 \times 10^{18}}$	1.5×10^{18}
Location where the calculation stops; R_{end}(cm)	$\mathbf{2.7 \times 10^{18}}$	$\mathbf{8.1 \times 10^{18}}$	2.7×10^{18}
Jet magnetic field intensity(G) at R_{start}	0.75		0.16
Scale of the broad line region r_{BLR}(cm)	0.12×10^{18}		0.2×10^{18}
Energy density of the BLR $U_{\mathrm{BLR}}\,(\mathrm{erg\,cm}^{-3})$	0.055		0.033
Photon energy of the BLR $h\nu_{\mathrm{BLR}}$(eV)	10		10
Scale of the host dusty torus r_{DT}(cm)	1.94×10^{18}		1.0×10^{19}
Energy density of the HDT $U_{\mathrm{BLR}}(\mathrm{erg\,cm}^{-4})$	5×10^{-3}		2×10^{-4}
Photon energy of the HDT $h\nu_{\mathrm{DT}}$(eV)	0.15		0.1

7.4.3 PKS 1510–089, #8

Modeling of another flare in PKS 1510–89 which showed apparently resolved profile shows distinctly different features compared with the former one.Again, parameters were basically taken from Barnacka et al. (2013) except for electron distribution and the locations of electron injection. Comparison of the modeled light curve with the observed three-hour binned light curve is presented in Figure 7.8. In this case, the distance electron injection lasts is set to 0.9×10^{17} cm and the location of injection starts is set to $R_{\mathrm{start}} = 3.3 \times 10^{18}$ cm to reproduce the observed light curve. In this case, the assumed location of emission is significantly farther than the former flare, which causes spectral components contributing to GeV emission different from the former one.

As the emitting region is placed farther in this case, the dominant component contributing to GeV gamma-ray flux becomes inverse Compton scattering of soft photons in hot dusty torus (HDT). Figure 7.9 presents simulated time evolution of SED and Figure 7.10 shows the time evolution of the simulated GeV spectrum superposed on the

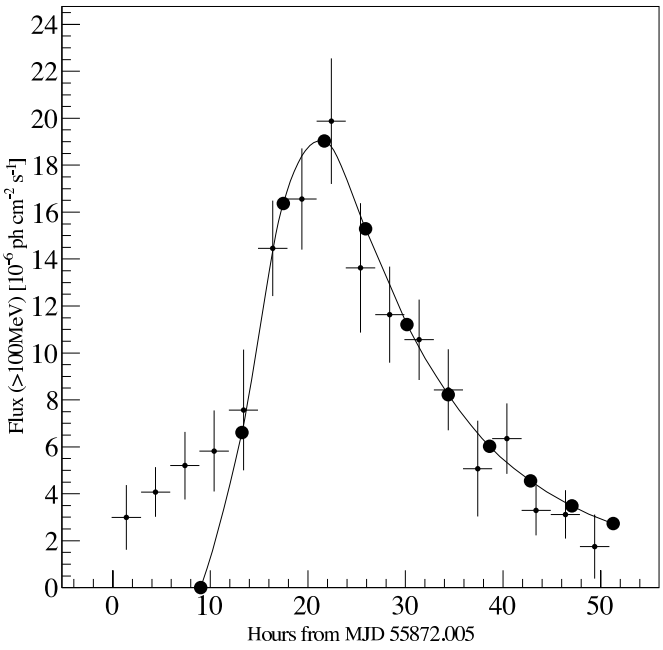

Figure 7.8: Simulated photon flux between 0.1 GeV and 300 GeV superposed on 3-hour binned light curve of the rapid flare (#8) in PKS 1510-089 around MJD 55872.

observed *Fermi*-LAT spectra created in three-hour binning.

7.4.4 4C 21.35, #6

We also modeled the apparently marginally resolved flare in 4C 21.35, which was included in flare #6 according to our definition. In this case, input parameters for the code were collected from literature they estimated parameters based on recent observations. Parameters for the external photon fields were taken from literature (Tanaka et al. (2011)), in which they estimated the $R_{\rm HDT}$ from the observed disk luminosity.

$$R_{\rm HDT} \simeq 4 \left(\frac{L_{\rm disk}}{10^{46}\ {\rm erg\,s^{-1}}} \right)\ {\rm pc} \simeq 10^{19}{\rm cm} \tag{7.17}$$

They also derived the scale and luminosity of BLR based on the optical intensity of Hβ line, that is $R_{\rm BLR} \simeq 2 \times 10^{17}$ cm and $L_{\rm BLR} \simeq 25.3 \times L_{\rm H\beta} \simeq 5 \times 10^{44}$ erg s^{-1}. Finally, we referred the luminosity of the broad line region and hot dusty torus from Malmrose et al. (2011), which are $L_{\rm HDT} \simeq 7.9 \times 10^{45}$ erg s^{-1}.

The modeled light curve is shown in Figure 7.11, and the evolution of SED is shown in Figure 7.12 Figure 7.13. In this case, the location of emitting region is similar with

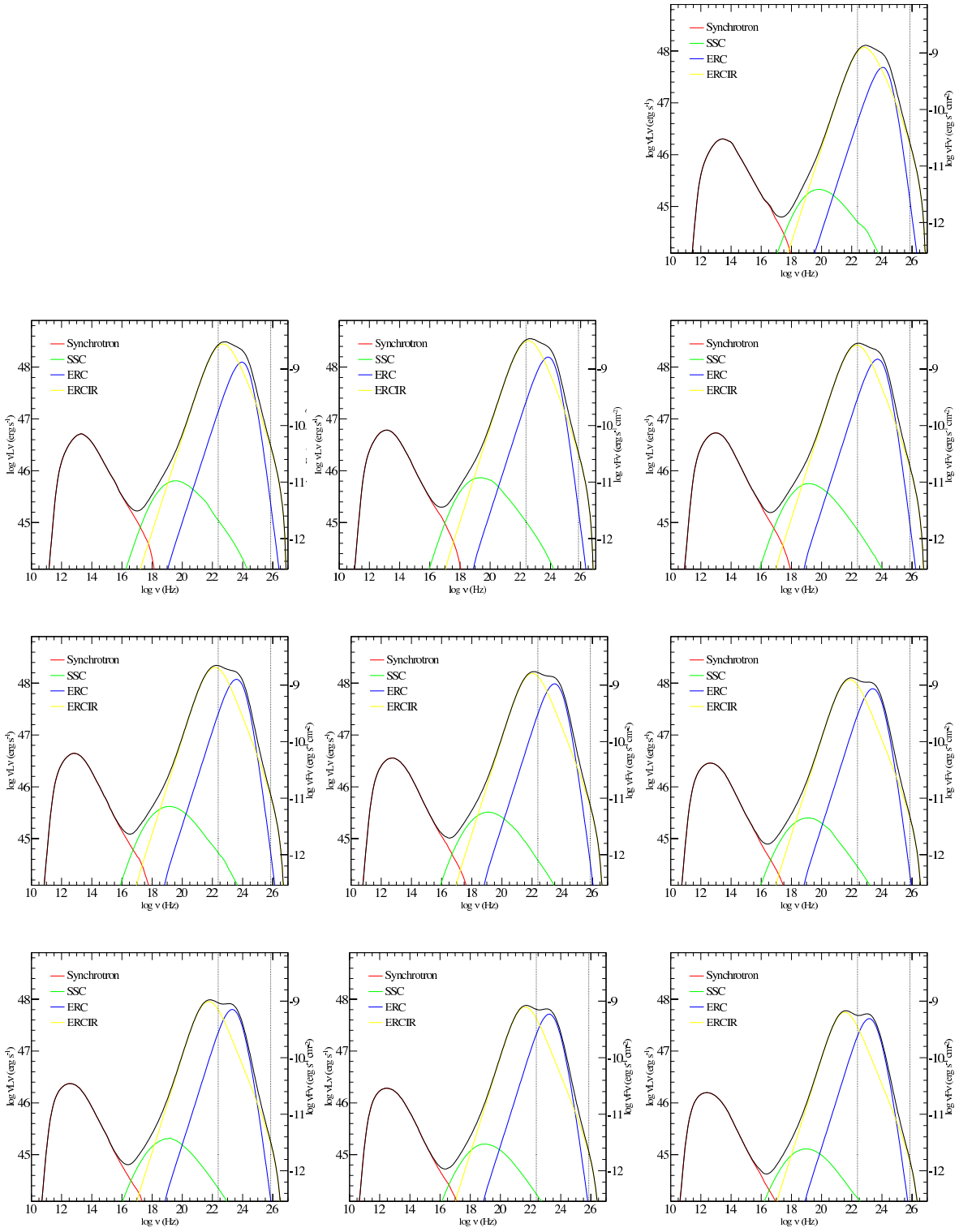

Figure 7.9: Variation of SEDs during the flare #8 in PKS 1510–089. Each SED corresponds to each simulated point in the light curve presented in Figure 7.8. Vertical dotted lines show the *Fermi*-LAT energy range (0.1 GeV – 300 GeV).

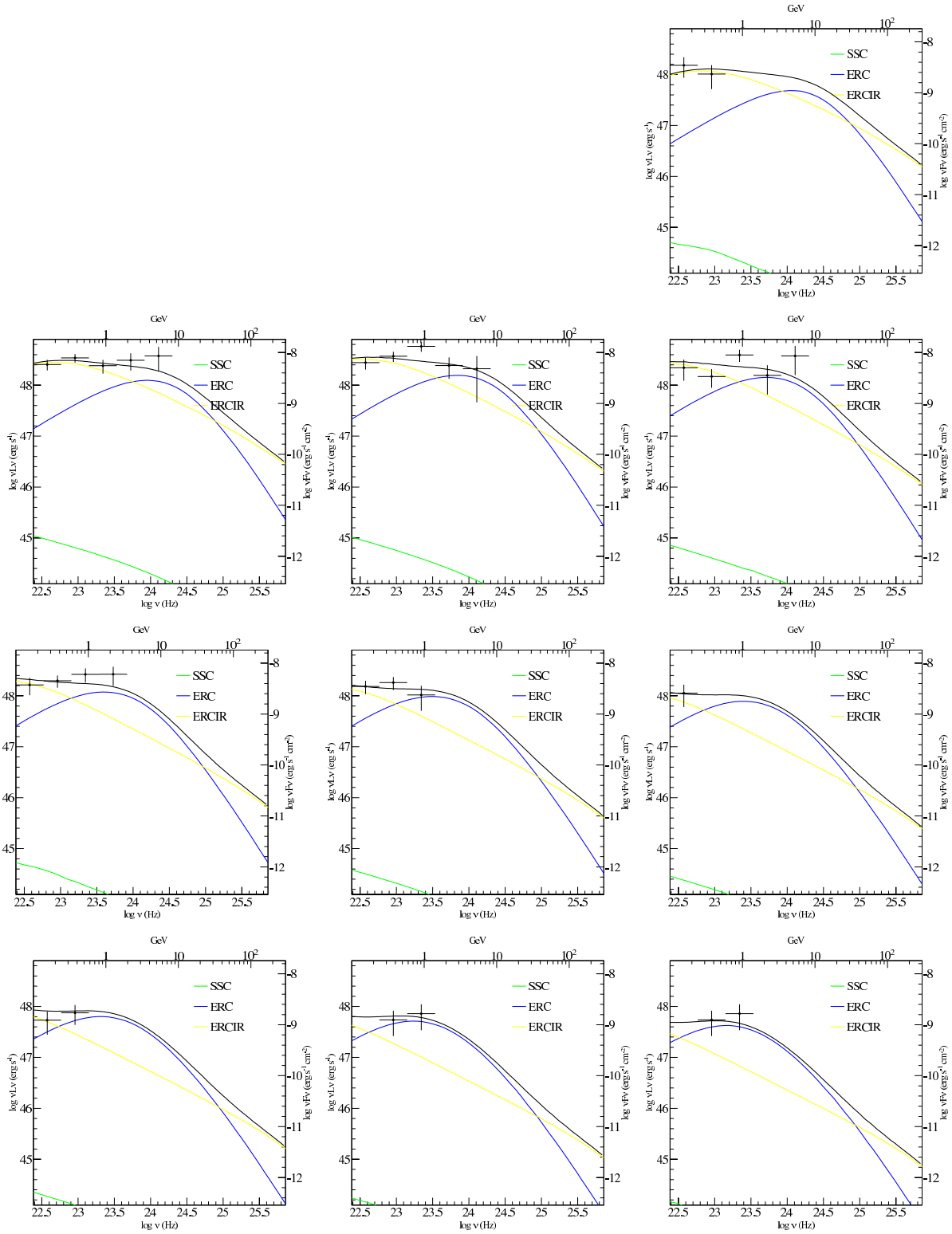

Figure 7.10: Zoomed-up SEDs during the flare #8 in PKS 1510–089 for the *Fermi*-LAT energy range (100 MeV – 300 GeV). Three-hour binned *Fermi*-LAT spectra corresponding to the time of simulated points were drawn on each SED.

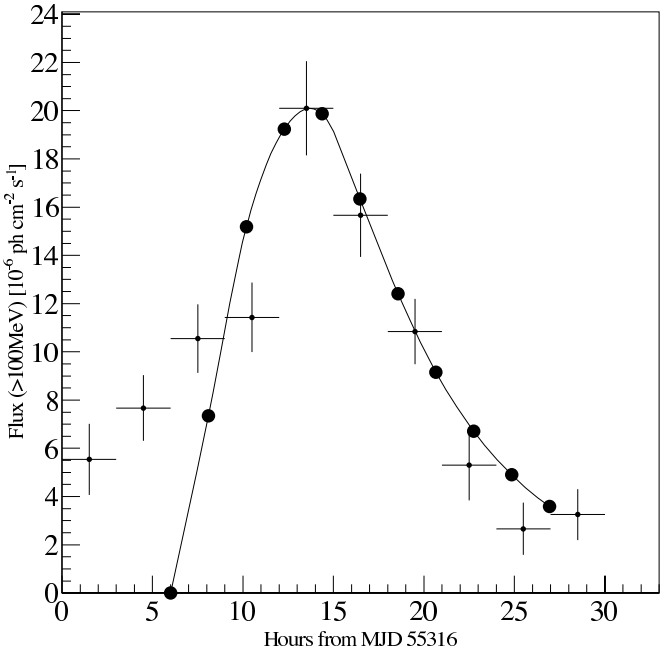

Figure 7.11: Variation of SEDs during the flare #6 in 4C 21.35. Each SED corresponds to each simulated point in the light curve presented in Figure 7.11. Vertical dotted lines show the *Fermi*-LAT energy range (0.1 GeV – 300 GeV).

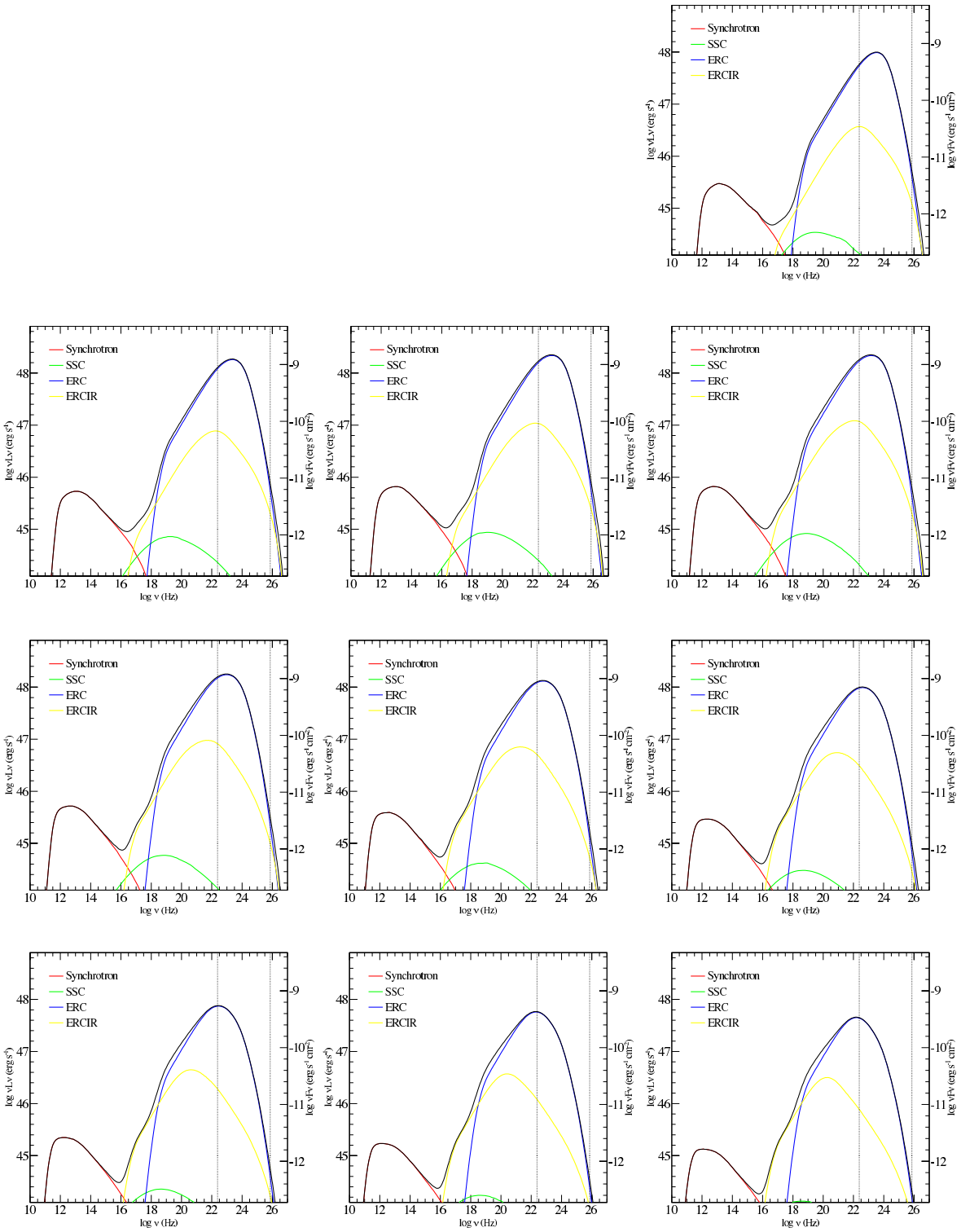

Figure 7.12: Variation of SEDs while the shell propagates along the jet. Each SED corresponds to each simulation point in Figure 7.11. Vertical dotted lines show the *Fermi*-LAT energy range.

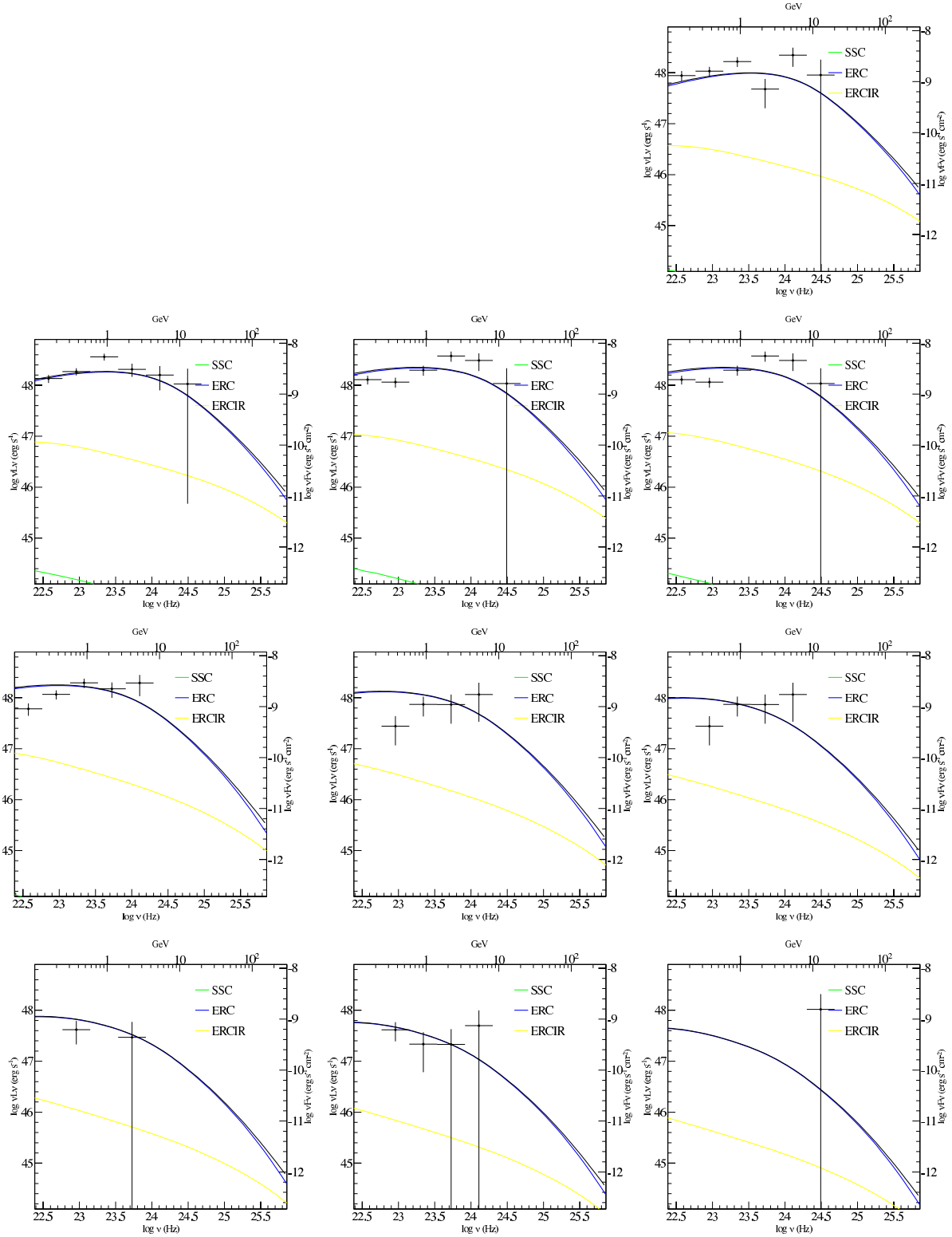

Figure 7.13: Zoomed-up SEDs during the flare #6 in 4C 21.35 for the *Fermi*-LAT energy range (100 MeV – 300 GeV). Three-hour binned *Fermi*-LAT spectra corresponding to the time of simulated points were drawn on each SED.

the first flare in PKS 1510–089, where broad line region is the dominant component for GeV emission.

7.5 Gradient Doppler Effect on the Observed Light Curves

We found that the cooling time scales of electrons are not sufficient to produce the time profile of the decay phase of the identified flares. The distribution of viewing angle of the colliding shells plays an important role to characterize the time profile. This viewing effect comes from the fact that there is gradient of Doppler factor inside the jet even if bulk Lorentz factor is uniform across the jet (Figure 7.14). Viewing angle (θ) relevant to observed photon flux ranges in $\theta_{\rm obs} - \theta_{\rm jet}(= \theta_{\rm min}) < \theta < \theta_{\rm obs} + \theta_{\rm jet}(= \theta_{\rm max})$, that results in gradient of doppler factor; $\delta_{\rm min} < \delta < \delta_{\rm max}$ where $\delta_{\rm min} = 1/\gamma(1 - \beta\cos(\theta_{\rm obs} + \theta_{\rm jet}))$ and $\delta_{\rm max} = 1/\gamma(1 - \beta\cos(\theta_{\rm obs} - \theta_{\rm jet}))$ (see Figure 7.14). As a result, the observed flaring profile consists of superposition of components of different doppler factors.

Time lag of flaring profile from different components of jets could be calculated as follows. Assuming that the internal shock forms at R_s and disappears at R_e from the center O, then the photon leaves $(R_s, \theta_{\rm min})$ and $(R_s, \theta_{\rm max})$ at $t = 0$ would be observed in the Earth at,

$$T_{{\rm s},\theta_{\rm min}} = \frac{D - R_s\cos\theta_{\rm min}}{c} \tag{7.18}$$

$$T_{{\rm s},\theta_{\rm max}} = \frac{D - R_s\cos\theta_{\rm max}}{c} \tag{7.19}$$

respectively. On the other hand, when the shock propagates along the jet with velocity of $c\beta$ to R_e, the emitted photon at $(R_e, \theta_{\rm min})$ and $(R_e, \theta_{\rm max})$ would be observed at,

$$T_{{\rm e},\theta_{\rm min}} = \frac{R_e - R_s}{c\beta} + \frac{D - R_e\cos\theta_{\rm min}}{c} \tag{7.20}$$

$$T_{{\rm e},\theta_{\rm max}} = \frac{R_e - R_s}{c\beta} + \frac{D - R_e\cos\theta_{\rm max}}{c} \tag{7.21}$$

respectively. From the above equations, we could estimate the effect of the distortion on observed flaring profile.

The observed time lag at beginning of the injection from components with different viewing angle $(\theta_{\rm min}, \theta_{\rm max})$ is estimated as,

$$\Delta T_s = T_{{\rm s},\theta_{\rm max}} - T_{{\rm s},\theta_{\rm min}} = \frac{R_s}{c}(\cos\theta_{\rm min} - \cos\theta_{\rm max}) \tag{7.22}$$

while the observed lag at the end of the injection is,

$$\Delta T_e = T_{\mathrm{e},\theta_{\max}} - T_{\mathrm{e},\theta_{\min}} = \frac{R_e}{c}(\cos\theta_{\min} - \cos\theta_{\max}) \tag{7.23}$$

On the other hand, observed duration of the flare from different components with different viewing angle is estimated as,

$$\Delta T_{\theta_{\min}} = T_{\mathrm{e},\theta_{\min}} - T_{\mathrm{s},\theta_{\min}} = \frac{\Delta R}{c\beta}(1 - \beta\cos\theta_{\min}) \tag{7.24}$$

$$\Delta T_{\theta_{\max}} = T_{\mathrm{e},\theta_{\max}} - T_{\mathrm{s},\theta_{\max}} = \frac{\Delta R}{c\beta}(1 - \beta\cos\theta_{\max}) \tag{7.25}$$

respectively, where $\Delta R = R_e - R_s$. Then the observed duration from a component with larger viewing angle is expanded by,

$$\frac{\Delta T_{\theta_{\max}}}{\Delta T_{\theta_{\min}}} = \frac{1 - \beta\cos\theta_{\max}}{1 - \beta\cos\theta_{\min}} = \frac{\delta_{\max}}{\delta_{\min}} \tag{7.26}$$

Finally the effect of the gradient Doppler factor is summarized in Figure 7.15. We note that the difference in Doppler factor also causes the difference in beaming effect, which results in difference in observed flux.

This effect of time difference significantly affects the flaring profile we considered in the previous section. Figure 7.3 and Figure 7.16 shows comparison of modeling light curve with `BLAZAR` code, decaying profile considering only corresponding cooling effect, and the observed light curve. Cooling timescale is significantly shorter than the observed decaying timescale.The effect of the gradient Doppler effect for each case in Figure 7.16 could be roughly estimated as $\Delta T_s \simeq 1$ hour and 6 hours respectively, where $\theta_{\min} = 0rad, \theta_{\max} = \theta_{\mathrm{obs}} = 0.045$ rad are assumed. Thus this effect becomes more significant when we the emitting region is far from the central blackhole.

7.6 Properties of the Internal Shock Contributing to Blazar Flares

Based on the picture of the internal shock scenario presented in chapter 2, we could evaluate the properties of the internal shock contributing to the particle acceleration during the flares. In the case of flare #5 in PKS 1510–089 which showed very rapid profile, the rising timescale of the flare is less than three hours. The size of the internal shock contributing to the flare could be estimated with equations presented in chapter 2. The length of the shocked region is $l_{\mathrm{sh}} \simeq 3 \times 10^{16}$ cm in the observer rest frame and $l'_{\mathrm{sh}} \simeq 1.5 \times 10^{15}$ cm in the jet rest frame, assuming the speed of shock is $0.1c$ in the jet

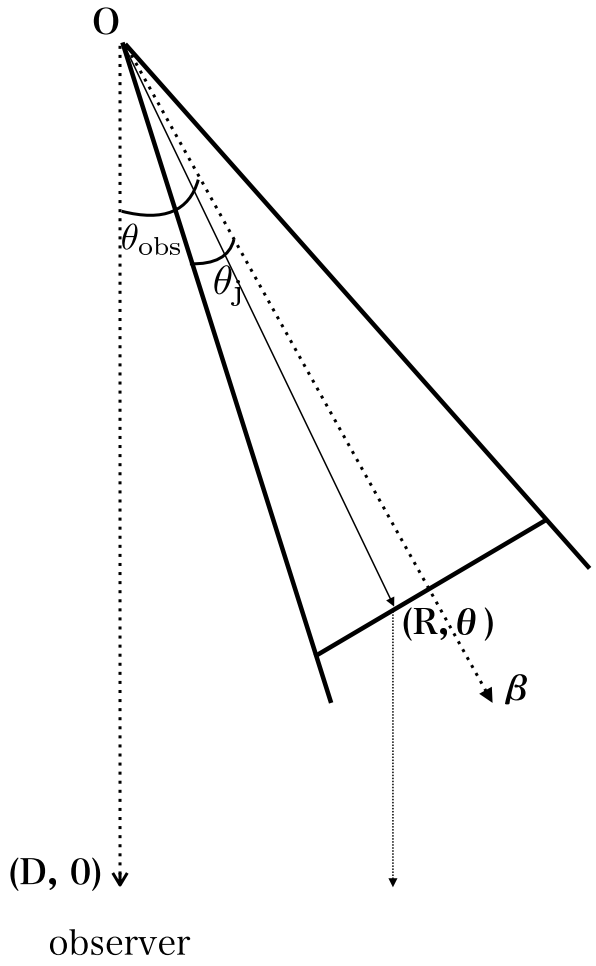

Figure 7.14: Jet picture presented in polar coordinates. The observer locates at (D, 0). A component of the relativistic shell propagating along the jet with velocity of $c\beta$ radiates at (R, θ).

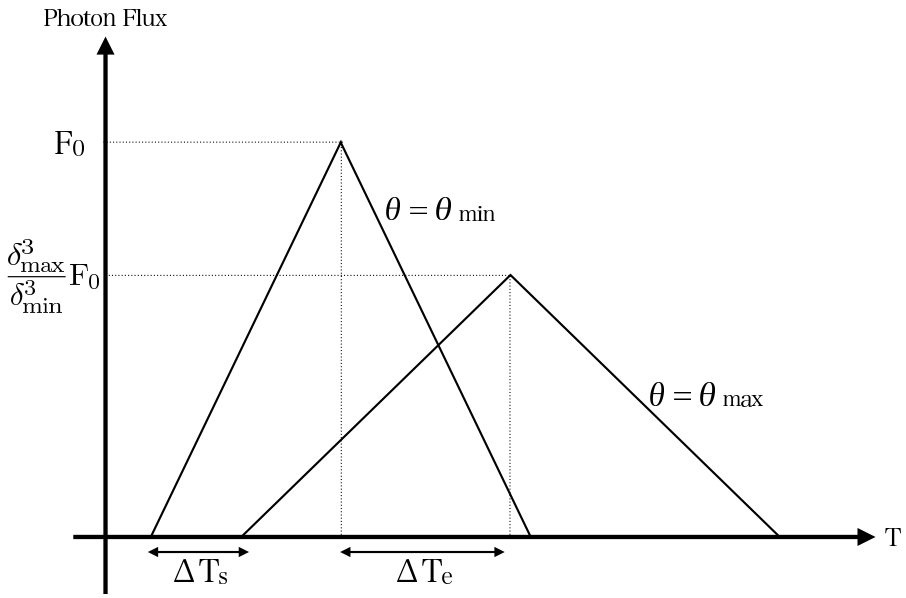

Figure 7.15: A figure illustrating the contributions from components with different observation angle to the observed flaring profile. The observed profile of flare would be distorted even the emitting shell has uniform bulk Lorentz factor across the jet.

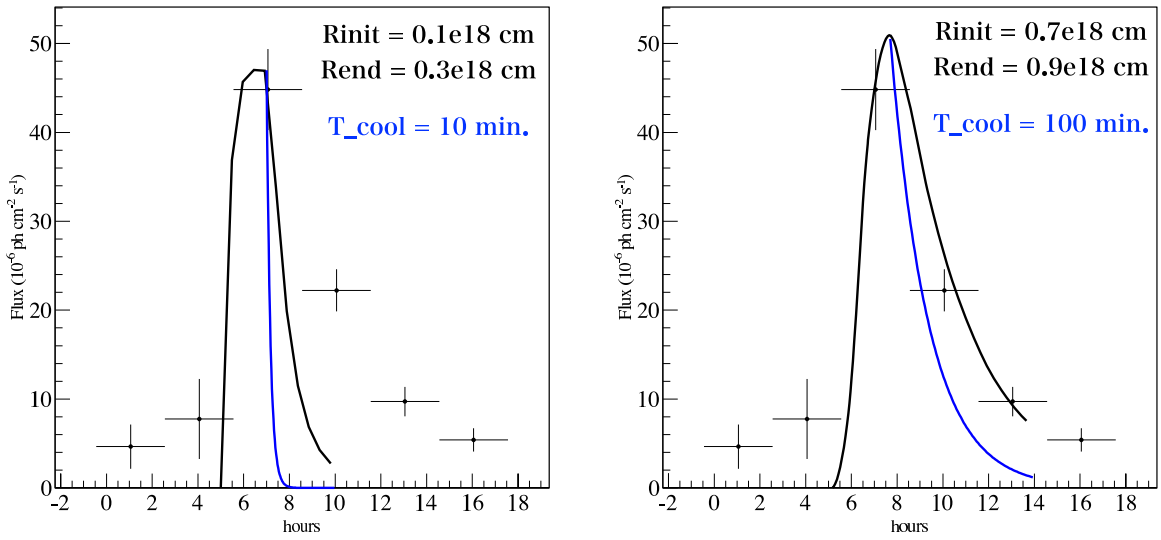

Figure 7.16: Comparison of electron cooling timescale and simulated decaying timescale of the flare #5 in PKS 1510–089 for different locations of emitting region. Black lines were obtained by numerical simulations with `BLAZAR` code. Blue lines were calculated by $F_{\rm peak} \exp\left((t - t_{\rm peak})/t_{\rm cool}\right)$, where $t_{\rm cool}$ was estimated from Eq. (7.7). Black points represent observed flux with *Fermi*-LAT.

rest frame. The value of $l_{\rm sh}$ is very small compared to the location of emitting region $\sim 7 \times 10^{17}$ cm, and implies very thin shock contributes to the huge GeV flare involving the whole energetics of the relativistic jet.

In this chapter, we successfully modeled the observed light curves of rapid GeV variability based on the internal shock scenario. We discovered that the rising profile of rapid variability depends on shock length of internal shock, and the emitting region should not necessarily be located at extremely close to the central blackhole. This model avoid the difficulty in the conventional model assuming the GeV emitting region to be extremely close to the central blackhole for producing rapid variability that the expected cooling timescale for relativistic electrons is much shorter than the observed decaying time scale of a flare. Another difficulty in the conventional model in explaining TeV detection of rapid variability in 4C 21.35 (Aleksić et al. (2011)) could also be avoided by the internal shock model.

We should note that the location of emission zone would be treated as upper limit in some situations. We could not exclude possibility of substructures of flares which are currently masked due to exposure gaps (which lasts about 60 minutes per orbit). If there are sub-flares in the gaps of light curves, each flare has faster decaying time than we inferred from 3-hour binned light curve. Then the location of real emission zone will be closer to the central black hole, where we expect fast cooling due to a dense photon field. Another thing we should keep in mind is the simplicity of the model. For example, we assumed electron injection at constant rate which immediately stops at certain distance from the BH. If there is still weakened injection of electrons in the decaying phase of flares, the expected decaying time of a flare should be longer than what we calculated with the modeling. In this case, we should put the emission zone closer to the BH.

Chapter 8

Conclusions

We studied rapid gamma-ray variability during the bright flares in FSRQs with *Fermi*-LAT. GeV gamma-ray study is of great importance since most of radiative energy of relativistic jets is dissipated as GeV gamma-rays in FSRQs. Followings are the conclusions in this thesis.

- For investigating variability of FSRQs with fine time resolution, we extracted a flux-limited sample of the brightest blazar flares observed with *Fermi*-LAT. Six bright objects were selected from $\sim$ 400 *Fermi*-detected FSRQs based on daily peak fluxes (3C 454.3, PKS 1510–089, 4C 21.35, 3C 273, CTA 102 and PKS 0402–362). We proposed interval definition of flares using duty cycle of the sources, and collected a sample of the ten brightest blazar flares from five-year data of the six bright blazars.

- We systematically analysed the ten selected intervals with three-hour binning, which is the shortest binning that we can expect basically constant exposure for all the bins. Very rapid GeV gamma-ray variability with the timescale of a few hours was discovered in PKS 1510–089, 4C 21.35 and 3C 273 from the systematic analysis of the selected flares. Among the analysed flares, PKS 1510–089 showed the shortest variability timescale of one hour, where photon flux increased by factor seven in three hours, which is the shortest variability timescale claimed for all the AGN in GeV range so far.

- The discovered rapid variability indicates that the total power released during the studied rapid and high-amplitude flares constitutes the bulk of the power radiatively dissipated in the source, and a significant fraction of the total kinetic luminosity of the underlying relativistic outflow.

- Sub-hour variability during the flares was investigated in the next step. Bayesian method was introduced in order to evaluate variability under very limited photon statistics, which is the case with our analysis. We adopted *Bayesian block*, which finds flux change points based on arrival times of events. We applied *Bayesian block* to each exposure window of LAT during the flares in order to study if there was significant variability within the exposure window lasting ∼30 minutes. Among the ten selected flares, variability within the single exposure window was marginally indicated for only one flare in PKS 1510–089, while there were no indications of variability for remaining nine flares. From these results, we concluded sub-hour variability in FSRQ would not be general.

Next, we interpreted the rapid gamma-ray flaring profiles based on the internal shock scenario, which gives us good prescription to interpret the observed rapid variability. We performed numerical simulations to derive a consistent set of parameters that describe the flare properties such as blazar emission zone.

- Rapid rising timescale of flares can be explained as the injection timescale of relativistic electrons in emitting shell in the internal shock scenario, and the emitting region is not necessarily located very close to the central blackhole. This picture avoids two major problems accompanied with a common interpretation of rapid variability which places the emitting region very close to the central blackhole, namely too fast cooling and the detection of rapid TeV gamma-ray variability.

- We discovered that gradient of Doppler factor inside the jet significantly distorts the decaying time profile of a flare. As a component of jet with larger observation angle has smaller Doppler factor, observed time profile of emission from the component would be delayed compared with the one from a component with smaller observation angle even if bulk Lorentz factor is uniform across the jet. We pointed out this effect should be taken into account when modeling the decaying time profile of flares.

- Finally we could successfully explain the whole time profile of the rapid flares based on the internal shock scenario. Furthermore, we suggested a new method for constraining the blazar emission zone using the well-resolved decaying timescale of a flare. As energy density of the external photon fields (broad line region and hot dusty torus) decay as a function of distance from the central blackhole, cooling timescale of relativistic electrons becomes long at far distance. Thus the observed rapid decaying would put strong constraints on the emitting region. We applied

this method to the observed decaying time profile of flares, and constrained that the GeV gamma-ray emission in PKS 1510–089 flare took place at around 10^{18} cm from the central blackhole assuming the observed flare was formed by a single shock.

In this thesis, we discovered the existence of hour-scale and high-amplitude GeV variability which involve the whole energetics of relativistic jets in FSRQs. We explained the mechanism inducing such rapid and huge variability based on the simple internal shock scenario, and constrained the location of blazar emission zone which has been a long lasting question in the blazar studies.

Our study of rapid variability is based on the best sample currently available in GeV energy range. Future gamma-ray instruments with larger effective area would reveal nature of blazar flares by examining shorter time variability, and focusing on short time variability presented in this thesis should play an important role.

Appendix A

Estimation of Emission Zone with Orbit Binned Light Curves

We performed modeling of light curves based on orbit-binned light curves, instead of 3-hour binned light curves presented in Chapter 7. By binning in each exposure windows, we could obtain better time resolution at the expense of photon statistics. Flux estimation (100 MeV – 300 GeV) was performed using standard maximum likelihood analysis (see Chapter 4).

The modeling results for the flare #5 in PKS 1510–089 are shown in Figure A.1 with placing simulated light curves at two different positions. Parameters for simulations were exactly same as was presented in Table 7.1 except for the locations of electron injection which were free parameters here. The optimum location where injection starts were $(1.2 \pm 0.2) \times 10^{18}$ cm and $(0.8 \pm 0.1) \times 10^{18}$ cm for upper and lower cases in Figure A.1, while the comparison of both cases suggests that the upper case is better fitted to the decaying time profile of the orbit binned light curves.

In conclusion, we could estimate the gamma-ray emission zone at $(1.2 \pm 0.2) \times 10^{18}$ cm from the central black hole in the framework of this modeling, which is consistent value obtained from the modeling with 3-hour binned light curves; $(1.1 \pm 0.2) \times 10^{18}$ cm (See Figure 7.4 for comparison).

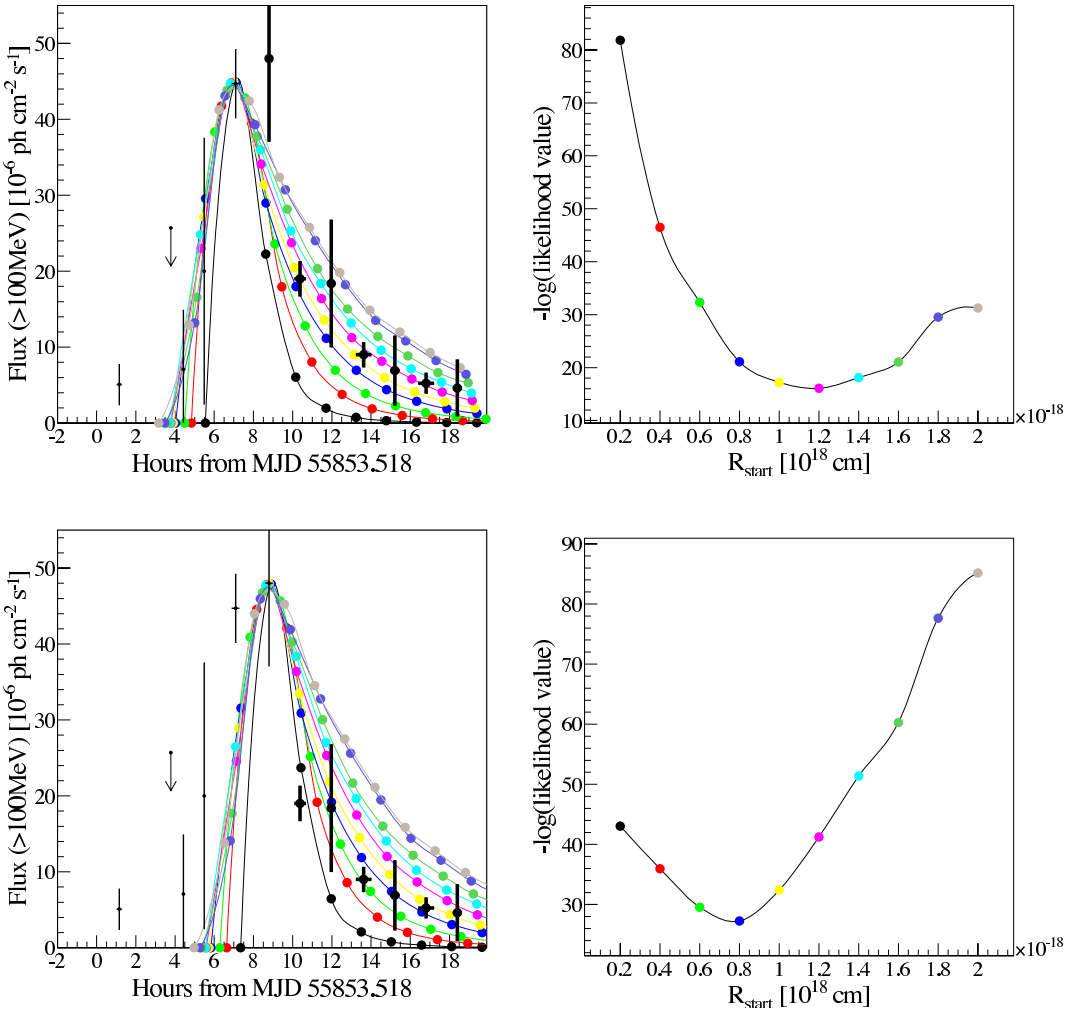

Figure A.1: Modeling results of orbit-binned light curves of the flare #5 in PKS 1510–089. Since we could not tell the time of flux peak in the orbit-binned light curves, we present results by setting the peak at two different times (upper panels and lower panels). Bold data points in the figures were used for evaluating likelihood values. From the maximum likelihood method, we could estimate the location where injection starts at $(1.2 \pm 0.2) \times 10^{18}$ cm and $(0.8 \pm 0.1) \times 10^{18}$ cm for upper and lower cases.

Bibliography

Abdo, A. A., Ackermann, M., Atwood, W. B., et al. 2009, ApJ, 697, 934

Abdo, A. A., Ackermann, M., Ajello, M., et al. 2009, ApJ, 699, 817

Abdo, A. A., Ackermann, M., Ajello, M., et al. 2010a, ApJ, 710, 810

Abdo, A. A., Ackermann, M., Agudo, I., et al. 2010c, ApJ, 721, 1425

Abdo, A. A., Ackermann, M., Ajello, M., et al. 2010b, ApJL, 714, L73

Ackermann, M., Ajello, M., Baldini, L., et al. 2010, ApJ, 721, 1383

Aharonian, F., Akhperjanian, A. G., Bazer-Bachi, A. R., et al. 2007, ApJL, 664, L71

Albert, J., Aliu, E., Anderhub, H., et al. 2008, Science, 320, 1752

Albert, J., Aliu, E., Anderhub, H., et al. 2007, ApJ, 669, 862

Aleksić, J., Antonelli, L. A., Antoranz, P., et al. 2011, ApJL, 730, L8

Arlen, T., Aune, T., Bendow, W., et al. 2013, ApJ, 762, 92

Atwood, W. B., Abdo, A. A., Ackermann, M., et al. 2009, ApJ, 697, 1071

Avni, Y. 1976, ApJ, 210, 642

Barnacka, A., Moderski, R., Behera, B., Brun, P. & Wagner, S. 2013, arXive:1307.1779

Becker, R. H., White, R. L., and Helfand, D. J. 1995, ApJ, 450, 559

Begelman, M. C., Fabian, A. C., & Rees, M. J. 2008, MNRAS, 384, L19

Bicknell, G. V. 1995, ApJS, 101, 29

Blandford, R. D. & Znajek, R. L. 1977, MNRAS, 179, 433

Brown, A. M. 2013, arXiv:1301.7677

Böttcher, M., Reimer, A., & Marscher, A. P. 2009, ApJ, 703, 1168

Carilli, C. L. & Barthel, P. D. 1996, A&A, 7, 1

Celotti, A., Padovani, P., & Ghisellini, G. 1997, MNRAS, 286, 415

Cortina, J. 2012, The Astronomer's Telegram, 3965, 1

D'Ammando, F., Raiteri, C. M., Villata, M., et al. 2011, A&A, 529, A145

D'Ammando, F., Pucella, G., Raiteri, C. M., et al. 2009, A&A, 508, 181

Donato, D., Ghisellini, G., Tagliaferri, G., et al. 2001, A&A, 375, 739

Foschini, L., Ghisellini, G., Tavecchio, F., Bonnoli, G., & Stamerra, A. 2011, A&A, 530, A77

Fossati, G., Maraschi, L., Celotti, A., et al. 1998, MNRAS, 299, 433

Gasparrini, D., & Cutini, S. 2011, The Astronomer's Telegram, 3579, 1

Ghisellini, G., Tavecchio, F., Foschini, L., et al. 2010, MNRAS, 402, 497

Ghisellini, G., & Tavecchio, F. 2009, MNRAS, 397, 985

Ghisellini, G., Tavecchio, F., Foschini, L. et al. 2011, MNRAS, 414, 2674

Ghisellini, G. 2013, arXiv:1309.4772

Giannios, D., Uzdensky, D. A., & Begelman, M. C. 2009, MNRAS, 395, L29

Hartman, R. C., Bertsch, D. L., Bloom, S. D., et al. 1999, ApJS, 123, 79

Hays, E. 2010, SPIE Newsroom (http://spie.org/x43269.xml), DOI:10.1117/2.1201011.003370

Homan, D. C., Ojha, R., Wardle, J. F. C. et al. 2001, ApJ, 549, 840

Homan, D. C., Wardle, J. F. C., Cheung, C. C., Roberts, D. H., & Attridge, J. M. 2002, ApJ, 580, 742

Hovatta, T., Valtaoja, E., Tornikoski, M. et al. 2009, A&A, 494, 527

Jackson, B., Scargle, J. D., Barnes, D., et al. 2005, IEEE Signal Processing Letters, 12, 2

Kataoka, J., Takahashi, T., Wagner, S. J. et al. 2001, ApJ, 560, 659

Kataoka, J., Madejski, G., Sikora, M., et al. 2008, ApJ, 672, 787

Kellermann, K. I., Lister, M. L., Homan, D. C. et al. 2004, ApJ, 609, 539

Kobayashi, S., Piran, T. and Sari, R. 1997, ApJ, 490, 92

Komissarov, S. S., Falle, S. A. E. G. 1997, MNRAS, 288, 833

Konigl, A. 1981, ApJ, 243, 700

Kubo, H., Takahashi, T., Madejski, G. et al. 1998, ApJ, 504, 693

Longair, M. S. 2011, High Energy Astrophysics (Cambridge University Press)

Malmrose, M. P., Marscher, A. P., Jorstad, S. G., et al. 2011, ApJ, 732, 116

Marscher, A. P. 1980, ApJ, 235, 386

Marscher, A. P. 2012, arXiv:1201.5402

Marscher, A. P., Jorstad, S. G., Larionov, V. M., et al. 2010, ApJL, 710, L126

Mattox, J. R., Bertsch, D. L., Chiang, J., et al. 1996, ApJ, 461, 396

Moderski, R., Sikora, M., & Blazejowski, M. 2003, A&A, 406, 855

Moderski, R., Sikora, M., Coppi, P. S., & Aharonian, F. 2005, MNRAS, 363, 954

Moderski, R., Sikora, & Bulik, T., 2000, ApJ, 529, 151

Nalewajko, K., Sikora, M., Madejski, G., et al. 2012, ApJ, 760, 69

Nenkova, M., Sirocky, M. M., Nikutta, R., et al. 2008,ApJ, 685, 160

Nolan, P. L., Abdo, A. A., Ackermann, M., et al. 2012, ApJS, 199, 31

Orienti, M., Koyama, S., D'Ammando, F., et al. 2013, MNRAS, 428, 2418

Orienti, M., Venturi, T., Dallacasa, D., et al. 2011, MNRAS, 417, 359

Ormes, in Current Perspectives in High Energy Astrophysics, NASA 1391, 1996

Perley, R. A., Dreher, J. W., Cowan, J. J. 1984, ApJ, 285, 35

Peterson B. M. 1997, Introduction to Active Galactic Nuclei (Cambridge University Press)

Peterson B. M., Ferrarese, L., Gilbert, K. M., et al. 2004, ApJ, 613, 682

Pian, E., Falomo, R., and Treves, A. 2005, MNRAS, 361, 919

Poutanen, J., & Stern, B. 2010, ApJL, 717, L118

Rees, M. J. 1978, MNRAS, 184, 61

Rybicki, G. B., & Lightman, A. P. 1979, Radiation Processes in Astrophysics (New York: Wiley)

Saito, S, Stawarz, Ł. Tanaka, Y. T., et al. 2013, ApJL, 766, L11

Sari, R. & Piran, R. 1995, ApJ, 455, L143

Scargle, J. D., Norris, J. P., Jackson, B., & Chiang, J. 2013, ApJ, 764, 167

Scargle, J. D. 1998, ApJ, 504, 405

Shakura, N. I., Sunyaev, R. A. 1973, A&A, 24, 337

Sikora, M., Błażejowski, M., Begelman, M. C., & Moderski, R. 2001, ApJ, 554, 1

Sikora, M., Błażejowski, Moderski, R. et al. 2002, ApJ, 577, 78

Sikora, M., Madejski, G., Moderski, R., & Poutanen, J. 1997, ApJ, 484, 108

Sikora, M., Begelman, M. C., and Rees, M. J. 1994, ApJ, 421, 153

Sikora, M., Stawarz, Ł., Moderski, R., Nalewajko, K., & Madejski, G. M. 2009, ApJ, 704, 38

Stawarz, Ł., Sikora, M., Ostrowski, M. et al. 2004, ApJ, 608, 95

Takahashi, T., Tashiro, M., Madejski, G., et al. 1996, ApJ, 470, 89

Takahashi, T., Kataoka, J., Madejski, G., et al. 2000, ApJ, 542, 105

Tanaka, Y. T., Stawarz, Ł., Thompson, D. J., et al. 2011, ApJ, 733, 19

Tanihata, C., Urry, C. M., Takahashi, T., et al. 2001, ApJ, 563, 569

Tanihata, C., 2001, Dissertation thesis

Tavecchio, F. & Ghisellini, G., 2008, MNRAS, 386, 945

Tavecchio, F., Ghisellini, G., Bonnoli, G., & Ghirlanda, G. 2010, MNRAS, 405, L94

Tavecchio, F., Becerra-Gonzalez, J., Ghisellini, G., et al. 2011, A&A, 534, A86

Thompson, D. J., Bertsch, D. L., Fichtel, C.E., et al. 1993, ApJS, 86, 629

Tompkins, W., 1999, Dissertation thesis

Urry, C. M., & Padovani, P. 1995, PASP, 107, 803

Wagner, S. J., & H.E.S.S. Collaboration 2010, AAS/High Energy Astrophysics Division #11, 11, #27.06

Wilks, S. S 1938, Ann. Math. Stat., 9, 60

Acknowledgements

First of all, I'm very grateful to Prof. T. Takahashi for his instruction throughout the past five years of my academic life in ISAS/JAXA. I was always encouraged by his profitable advice and I obtained a lot of ideas through the conversations. I thank Dr. Ł. Stawarz for all the discussions about the interpretaions of *Fermi*-LAT data analysis results. I also thank Dr. Y. Tanaka and Dr. H. Odaka for encouraging me for years and giving a lot of suggestive comments on this thesis. Prof. P. Coppi took care of me during my stay in Yale university. I learned a lot from his enormous amount of knowledge and ideas. Dr. G. Madejski instructed me when I stayed in SLAC. His careful guide helped me a lot when I started to work on data analysis of *Fermi*-LAT. I'm grateful to Prof. M. Urry, Dr. J. Scargle and Dr. J. Chiang for the discussions about statistics. I thank Dr. R. Moderski for providing the code for the modeling. Finally, I really thank my familiy for their support and encouragement.